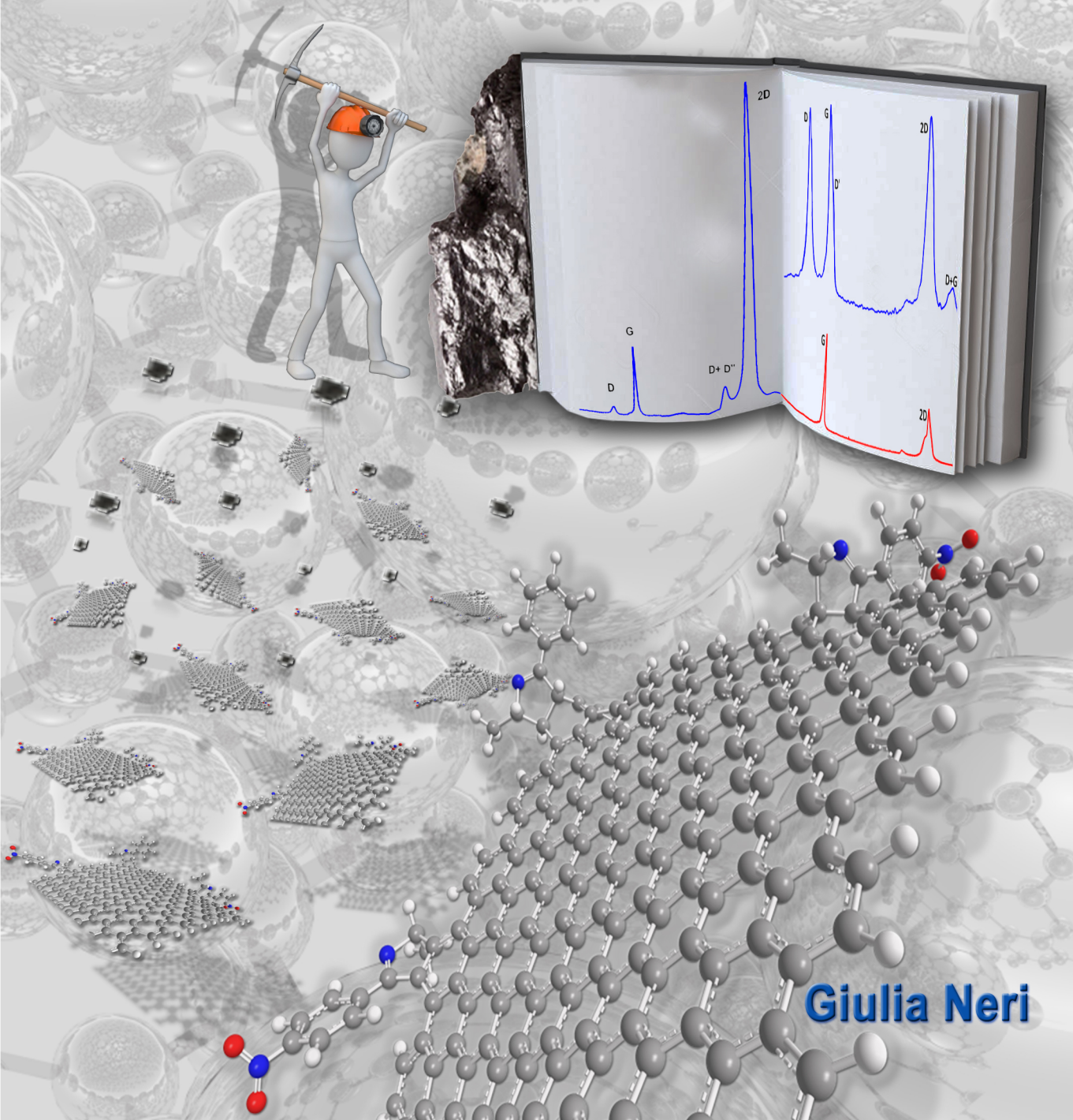




Engineering of Graphene Materials for Biomedical Applications

From graphite to new functionalized
graphene derivatives by top-down approaches

Dottorato di Ricerca in Scienze Chimiche XXIX Ciclo
2014-2016



Giulia Neri



UNIVERSITÀ DEGLI STUDI DI MESSINA

Dipartimento di Scienze Chimiche, Biologiche, Farmaceutiche ed Ambientali

Dottorato di ricerca in Scienze Chimiche

XXIX Ciclo (CHIM/06)

Engineering of Graphene Materials for Biomedical Applications

From graphite to new functionalized graphene
by top down-approaches

Giulia Neri

Supervisor

Prof. Anna Piperno

Coordinator

Prof. Sebastiano Campagna

2014-2016

Table of Contents

<i>Aim of the work</i>	2
Chapter 1:	6
1.1 Graphene materials	7
1.2 Characterization of G materials	13
1.3 Biomedical Applications of G Materials	16
Chapter 2:	24
2.1 Graphene as platform for drug delivery	25
2.2 Graphene nanoplatforms	26
2.3 Silibinin-Conjugated Graphene Nanoplatform	33
2.4 Reactive Azlactone Graphene Platform (RAGP).....	42
2.5 Catalytic Properties and Immobilization Studies of Graphene Catalase Bioconjugate (G-Cat)	54
2.6 Experimental section	60
Chapter 3:	74
3.1 Functionalized G nanosheets by a top-down approach from graphite using oxazolone chemistry.....	75
3.2 Computational studies	87
3.3 Graphene/Gold Nanocomposites for SERS applications	93
3.4 Experimental section	105
Chapter 4	110
4.1 Basic concepts about peptide self-assembly	111
4.3 SD1: a peptide for gene-delivery	119
4.4 Experimental section	124
Acknowledgements	130
References	132

Aim of the work

The discovery of graphene (**G**) and its functionalized derivatives has been accompanied by increasing research attention to explore these new materials for biomedical applications due to their unique structure and excellent mechanical, optical and electrical properties.

Generally, synthetic methods of **G** are classified in two categories: top-down and bottom-up. The former approach entails exfoliation of a layer of **G** from graphitic materials. The latter approach involves the building up of **G** using carbon-based materials. The bottom-up approach is simple, although it produces material with relatively more defects than the top-down approach. Top-down strategies separate the stacked sheets by disrupting the Van der Waals forces that hold the sheets together. Damaging of the sheets during the exfoliation process and re-agglomeration of the separated sheets are some of the disadvantages of the top-down technique.

The biocompatibility of **G** is the most critical issue for the applications in the biomedical/pharmaceutical field and its chemical modification is the key factor for designing stable and safe drug delivery nanodevices.

It is known that size, shape, morphology, thickness, degree of functionalization and dispersibility of **G** play critical roles in regulating biological behaviours and toxicity. Therefore, the development of adequate **G** preparation methods represents a key factor to achieve good **G** materials for biomedical applications.

The thesis describes the synthesis and the characterization by complementary techniques of new functionalized **G** materials obtained by two different top-down approaches. Moreover, some biomedical applications of newly synthesized **G** materials have been investigated.

The thesis is structured in four chapters.

The first chapter reports an overview of the main characteristics of **G** materials and describes the currently available procedures for their fabrication and summarizes the main biological applications.

The chapter II about reports the functionalization of **G** materials with the terminal alkyne units and their synthetic applications by click assembly with azido-functionalized compounds (Fig. 1).

The alkyne-terminated graphene platform (**G-Alk**) was obtained in good yield by reduction of graphene oxide (**GO**) with *hydrazine* followed by grafting of *p*-(2-propynyloxy)-benzene units by reaction with diazonium salts. The click assembly of **G-Alk** with the azido flavonoid Silibinin (**Sil**) provided a new drug delivery nanoplatform (herein called **G-Sil**). The cytotoxicity of the new platform has been evaluated on human mesenchymal stem cells and the anticancer effects have been studied on human osteosarcoma cell lines. Our **G** nanoplatform did not show any cytotoxicity even at high concentration (1000 $\mu\text{g/ml}$) and **Sil** grafted onto **G** maintained its antiproliferative activity.

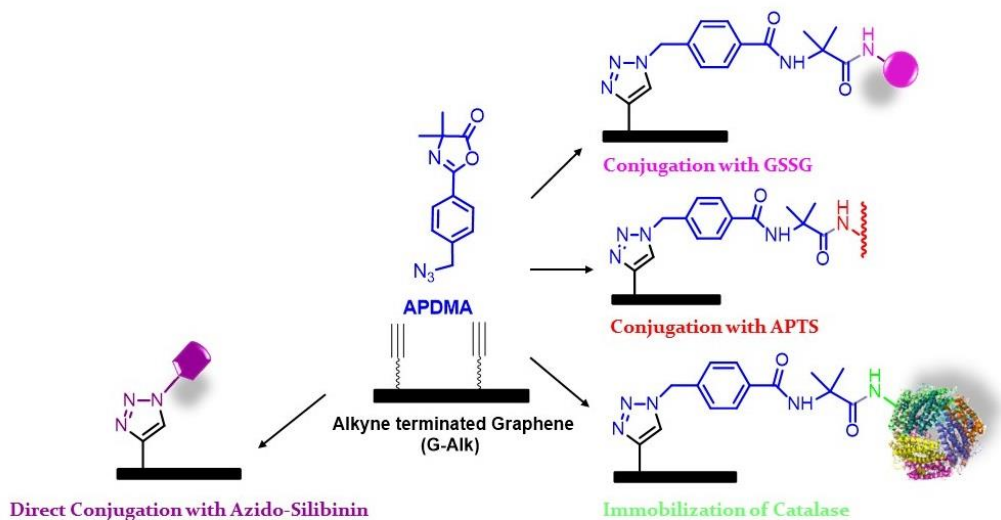


Figure 1 Alkyne-terminated graphene platform.

The click reaction of **G-Alk** with the oxazolone (**APDMA**) containing an azido moiety has been used to build the reactive **G** platform (**RAGP**). The **RAGP** has been employed for the silylation of **G** surfaces and for the selective conjugation with compounds of biological interest such as glutathione (**GSSG**) and catalase (**Cat**).

The chapter III reports the direct delamination and functionalization of graphite into **G**, exploiting the reactivity of mesoionic compounds in solvent-free conditions (Fig.2). For the first time we have demonstrated that the solvent-free 1,3-DC reaction of mesoionic compounds is an effective tool for the direct functionalization and delamination of graphite flakes into few layers of **G** nanosheets. The procedure has been tested by employing two differently substituted oxazolones and a high degree of functionalization (2.1–4.6% @700 °C) was obtained for both substrates under mild conditions (70–120 °C). The graphite exfoliation efficiency depends upon the oxazolone substitution pattern. The exfoliation and functionalization was confirmed by micro-Raman and X-ray photoelectron spectroscopies, scanning transmission electron microscopy (STEM) and thermogravimetric analysis (TGA). Moreover computational studies showed that the reaction proceed mainly on the corner and on the edge of graphenic system.

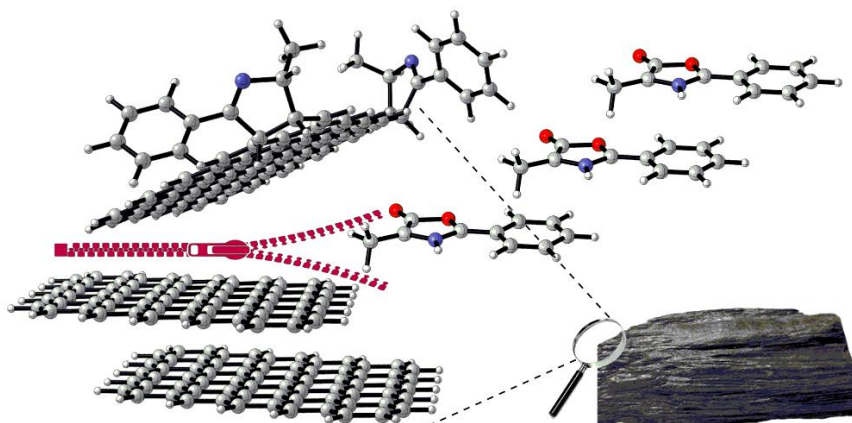


Figure 2 Functionalized graphene platform obtained by direct exfoliation and delamination of graphite.

These data were confirmed by decoration of the surface **G** layers with gold nanoparticles (Au NPs). STEM analysis showed that Au NPs are mainly located on edge of **G** layers. Finally, the properties of **G-NH₂/Au** nanocomposites as SERS materials have been investigated using Rhodamine 6G (R6G) as a probe.

The final chapter of the thesis (chapter IV) is focused on the development of a coiled-coil peptide for gene-delivery. This section reports the results of the research project carried out at the National Physical Laboratory of London (NPL, UK), within the Biotechnology group, under the supervision of Dr Max Ryadnov and Dr Emiliana De Santis. The chapter reports the characterization studies of peptide (**SD1**). TEM analysis has been used to confirm the formation of peptide sphere structures by self-assembling process; qualitative titrations have been employed to prove the formation of SD1/siRNA complex. From these studies, **SD1** emerged as a good candidate for gene-delivery; actually, SD1/siRNA complex is under biological evaluation.

Chapter 1:

Graphene: Synthesis, Characterization and Biological Applications

This chapter reports an overview on **G** materials focusing the attention on the preparation methods, the characterisation techniques, that are generally, used to investigate the structure, morphology and chemical composition of **G** materials. Moreover, the chapter covers recent literature and deals with the basic concepts, the chemistry, the potentialities and the problems due to the toxicity of the **G** materials proposed for biomedical applications.

1.1 Graphene materials

G is an allotropic form of carbon; it exhibits a bi-dimensional honeycomb lattice structure (Fig. 1.1), where each carbon is hybridized sp^2 with an estimated interatomic distance of 0.142 nm and a hexagon center to center distance of 0.246 nm (Fig. 1.2).⁽¹⁾ **G** exposes a large surface area, rich of π electrons, which determinate its outstanding proprieties. **G** shows an am-bipolar conductivity with an electron mobility until to $40.000 \text{ cm}^2/\text{Vs}$ ⁽²⁾, a good thermal conductivity (between 4.84 ± 0.44 and $5.30 \pm 0.48 \cdot 10^3 \text{ W/mK}$ at r.t.) ⁽³⁾, an optical transmittance ($\sim 97.7\%$) ⁽⁴⁾; moreover it is a robust material and at the same time flexible and lightweight with a density of 0.77 mg/m^2 .⁽⁵⁾

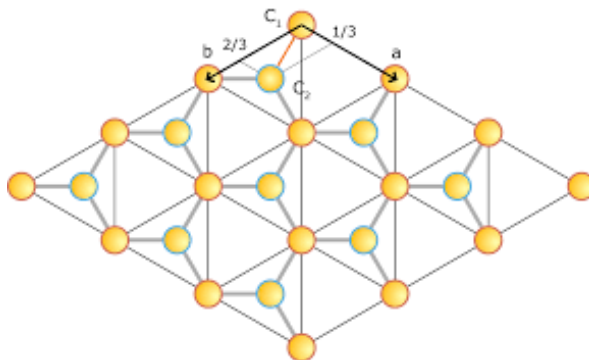


Figure 1.1 Representative honeycomb lattice structure of **G**.

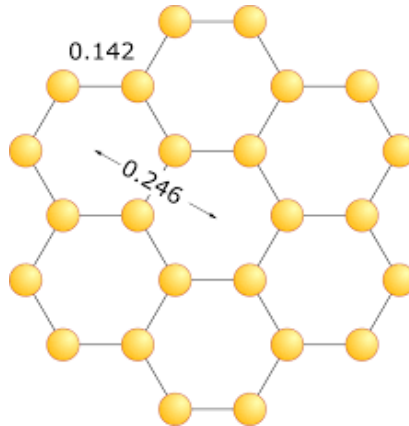


Figure 1.2 Illustrative figure of the atomic distance in **G** material.

Since the discovery of **G**, the research ⁽⁶⁾ on it has increased exponentially ⁽⁷⁾ and the family of “**G** materials” under consideration has expanded beyond monolayer **G** to include related materials with significant variations in layer number, lateral dimension, rotational faulting, and chemical modification. This increasing interest caused confusion among researchers in regard to the terms that would have been used to name **G** materials. Recently, a nomenclature for **G** derivatives has been proposed to clarify and overcome some questions in this respect ⁽⁸⁾:

“**Graphene** – a single-atom-thick sheet of hexagonally arranged, sp^2 -bonded carbon atoms that is not an integral part of a carbon material, but is freely suspended or adhered on a foreign substrate. The lateral dimensions of graphene can vary from several nanometers to the macroscale.

Graphene layer – a single-atom-thick sheet of hexagonally arranged, sp^2 -bonded carbon atoms occurring within a carbon material structure, regardless of whether that material structure has 3D order (graphitic) or not (turbostratic or rotationally faulted). The “graphene layer” is a conceptual structural unit that has been used for many years to describe the structure and texture of 3D carbon materials with primary sp^2 -hybridized bonding.

Turbostratic carbon – three-dimensional sp^2 -bonded carbon material in which there is no defined registry of the layers, meaning there is no spatial relationship between the positions of the carbon atoms in one **G** layer with those in adjacent layers. This is a common structure in carbon materials prepared at lower temperatures or in “hard carbons” that do not pass through a fluid phase during carbonization and resist the development of 3D crystalline order even upon very high temperature heat treatment.

Bilayer graphene, trilayer graphene – 2D (sheet-like) materials, either as free-standing films or flakes, or as a substrate-bound coating, consisting of 2 or 3 well-defined, countable, stacked **G** layers of extended lateral dimension.

Multi-layer graphene (MLG) – a 2D (sheet-like) material, either as a free-standing flake or substrate-bound coating, consisting of a small number (between 2 and about 10) of well-defined, countable, stacked **G** layers of extended lateral dimension.

Few-layer graphene (FLG) – a subset of multi-layer **G** (defined as above) with layer numbers from 2 to about 5.

Graphene nanosheet – a single-atom-thick sheet of hexagonally arranged, sp^2 -bonded carbon atoms that is not an integral part of a carbon material, but is freely suspended or adhered on a foreign substrate and has a lateral dimension less than 100 nm.

Graphene oxide (GO) – chemically modified **G**, prepared by oxidation and exfoliation that is accompanied by extensive oxidative modification of the basal plane. **GO** is a monolayer material with a high oxygen content, typically characterized by C/O atomic ratios less than 3.0 and typically closer to 2.0.

Reduced graphene oxide (rGO herein called G-Red) – **GO** (as above) that has been reductively processed by chemical, thermal, microwave, photo-chemical, photo-thermal or microbial/bacterial methods to reduce its oxygen content.

Graphene materials (also graphene-based materials, graphene nanomaterials, graphene-family nanomaterials) – overarching terms for the collection of 2D materials defined above that contain the word “graphene”, including multilayered materials (N less than about 10), chemically modified forms (**GO**, **G-Red**), and materials made using **G**, **GO**, or another **G** material as a precursor.”

Moreover, the **G** derivatives are also named, according to synthetic strategy employed to obtain them. Generally, these synthetic strategies are classified in two big categories: bottom-up and top-down techniques.⁽⁹⁾ The “scotch-tape method” has been the first to be applied and it has been proposed by Geim and Novoselov.⁽¹⁰⁾ It is a mechanical exfoliation (top-down approach) and provided particular thin tallies of graphite of high quality, [*Highly Ordered Pyrolytic Graphite* (**HOPG**)]. Although, **HOPG** is a high quality material, the scotch-tape method is not a suitable strategy to apply on large scale.⁽¹⁰⁾

Another top-down strategy concerns the “liquid exfoliation of **G**”, by using chemical solvents such as DMF or NMP under strong sonication conditions. However, several studies have demonstrated that the liquid exfoliation is not an efficient method because the **G** layers obtained show many surface defects.⁽¹¹⁾

The main methods of alternative bottom-up strategy are the chemical vapor deposition (CVD) and the epitaxial growth (EG). EG strategy consists in the production of **G** layers by using monocrystalline silicon carbide, which shows two different surface terminations, Si-terminated and C-terminated. The process consists in a thermal desorption of silicon from monocrystallines SiC; if the **G** layers are generated by Si-terminated, they show a homogenous surface with high carrier mobility. On the contrary the C-terminated ones show a heterogeneous surface with many defects. In addition, from Si- and C-terminated, **FLG** and **MLG** systems are obtained, respectively. EG is an efficient method to obtain **G** layers of high quality on large scale and the number of **G** layers depends on the applied

temperature. In order to reduce the cost of fabrication, more attention has been paid to find an alternative to the expensive SiC.⁽¹²⁾

In CVD method the **G** grows on a metal poly/monocrystalline support and acetylene or methane are used as carbon source. The process occurs at high temperature (~ 1000 °C), under hydrogen flow, to keep the respective metal in its catalytic state. Copper and nickel are the most employed in CVD strategy; generally, by using copper, monolayer systems have been obtained, whereas the use of nickel generates few layers. To improve the efficiency of CVD strategy and to reduce the costs, some changes about this method have been proposed.⁽¹³⁾

Other efficient methods to produce **G** of high quality have been developed.⁽¹⁴⁾

In particular, the research focused the efforts on the synthesis of functionalized **G** materials.⁽¹⁵⁾ It has been demonstrated that the functionalization of **G** is the key to control its chemical-physical properties.

Both covalent⁽¹⁶⁾ and non-covalent⁽¹⁷⁾ surface modifications of **G**-based materials can be exploited to convey specific properties to **G** and to increase its colloidal stability.

Among the covalent approaches the radical reactions are the most applied. Diazonium salts are used to generate in situ aryl radicals, which attack the **G** surface, forming new C sp^3 -aryl-bond on the sp^2 **G** network.⁽¹⁸⁾

Other important approaches to fabricate functionalized **G** materials are 1,3-dipolar cycloaddition (1,3-DC)^(19, 20), the Bingel reaction⁽²¹⁾ the Diels–Alder reaction (DA).^(22, 23) DA reaction is the most investigated cycloaddition process, since Haddon and co-workers have suggested that **G** can be used as either a diene or a dienophile for DA reactions.⁽²⁴⁾

Other methods for the functionalization of **G** include the introduction on **G** surface of single atoms such as fluorine and chlorine by halogenation processes, other halogens are not used due to stability problems. The fluorination is an

uncontrollable process due to the fast kinetics; the fluorinated **G** showed a reduced conductivity with respect to **G**.⁽²⁵⁾ Conversely, chlorination is a better controllable process and the product exhibits a good carrier mobility. **G** materials can be subjected to hydrogenation reaction on SiO₂/Si substrates.⁽²⁶⁾

The most employed approaches for the preparation of **G** materials involve the chemistry of **GO** obtained from graphite by Hummer or Brodie methods.⁽²⁷⁾ The oxidation process produces first graphite oxide that after strong exfoliation treatment produces **GO** (Fig. 1.3), which could be subsequently subjects to chemical reduction to obtain **G-Red** (Fig. 1.3). The strong oxidation conditions adopted in these processes destroy the **G** sp² network, and the reduction process restore only partially the sp² network. Hence, these **G** materials cannot be used to produce electrical devices, but they are strongly investigated in laboratory for other applications like those in biomedical field since the residual polar groups increase their biocompatibility.

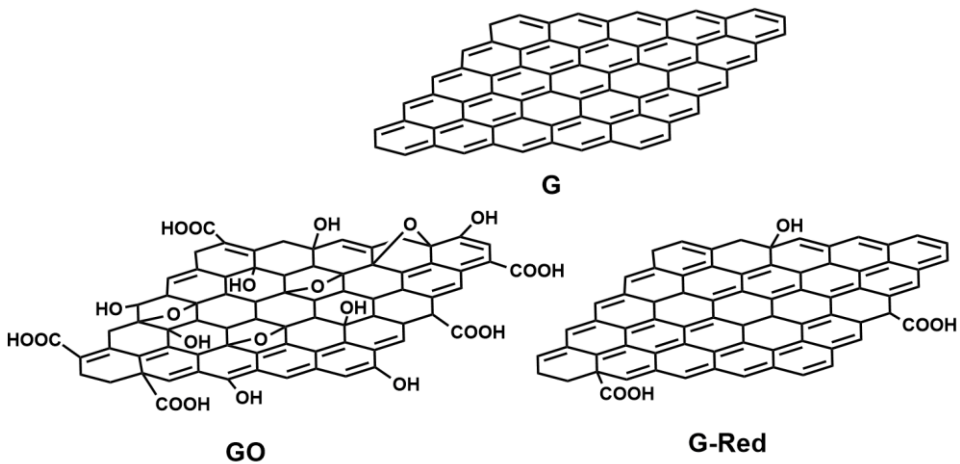


Figure 1.3 Graphene (**G**), Graphene Oxide (**GO**) and Reduced Graphene (**G-Red**).

1.2 Characterization of G materials

A very important aspect of G materials research is the definition of their chemical composition, crystal structure, thickness, lateral dimension, by employing a combination of spectroscopy, microscopy and thermogravimetric techniques.

The Raman spectroscopy is one of the most extensively, non-destructive optical techniques used to detect the structural features of G materials.⁽²⁸⁾ Information can be gained about the amount of G network order, its exfoliation degree or in some cases, the number of stacking layers.⁽²⁸⁾ In a typical G Raman spectrum, two main characteristic bands are present: *i*) the so called G-band centered at about 1580 cm^{-1} , due to in plane modes vibrations of sp^2 network; *ii*) the so called 2D, or D', band at about 2680 cm^{-1} (Fig. 1.4), an overtone of the D one, generally located at about 1330 cm^{-1} , due to different inter-plane vibration modes. The D peak is absent in pristine G due to its crystal symmetries. On the contrary, D band is present in Raman spectra of G derivatives, such as GO or G-Red, as consequence of the inherent chemical treatments which induce imperfections on the carbon basal plane. In this condition, breathing modes of aromatics rings will be activated and D band results evident. Moreover, in the spectrum of G derivatives, other two bands: D' (1620 cm^{-1}) and D+G (2940 cm^{-1}), can be detected (Fig. 1.5). They are activated by the increased disorder of the sp^2 network, due to the defects introduced by chemical functionalization of G surfaces.

The interaction forces among G layers influences the intensity, the shape and the position of these bands. Therefore, information about the number of layers can be obtained by studying the band modifications. In single-layer G, 2D band shows a narrow peak around 2950 cm^{-1} while, in presence of overlapped layers, the forces due to the interactions between the layers of the stacked G, determine a splitting of the 2D peak. Thus, some different vibrational modes are activated and the 2D band is characterized by four sub-bands.⁽²⁸⁾ At the same time, upon increasing the layers

number a smaller red shift of the G-band can also be observed. Hence, the number of **G** layers can be indirectly estimated by the I_{2D}/I_G band intensity ratio, as well as analyzing their shapes and their shifts. The I_G/I_D band intensity ratio is commonly used to indicate the disorder degree of the **G** material.⁽²⁹⁾ In the pristine graphite, a high I_G/I_D ratio value (3.7) is observed, indicating a highly ordered system while, in the graphene based materials, a progressive decrease of the graphitization degree is clearly evident.⁽²⁹⁾

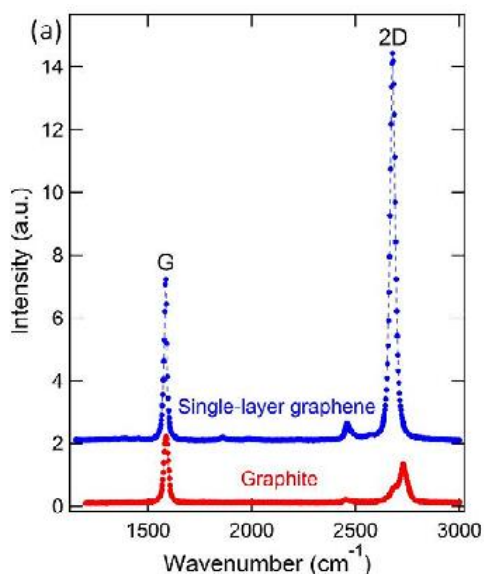


Figure 1.4 Raman spectra of a monolayer graphene system and graphite bulk.⁽²⁸⁾

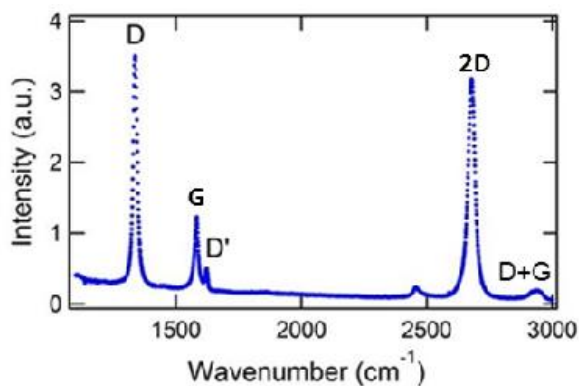


Figure 1.5 Raman spectrum of functionalized graphene multilayer system.⁽²⁸⁾

Information about the chemical composition and the kind of chemical bond fraction present on **G** surfaces (i.e. C-O bonding coordinations) can be obtained by X-ray photoelectron Spectroscopy (XPS).⁽²⁹⁾ XPS is used to investigate the **G** functionalization and to study how the chemical surface's coordination changes during **G** material synthesis (i.e from graphite to **GO** and **G-Red**). In particular, C 1s peak is made up by five different chemical shifted components, assigned to C atoms bonded to various oxygen function groups: 289.2 eV (carboxyl groups), 287.5 eV (carbonyl groups) 286.55 eV (epoxy groups) and 285.86 eV (hydroxyl groups). Another important contribute is related to sp^2 carbon atoms in aromatic rings assigned at 284.5 eV. At the same time three characteristic peaks contribute to the O 1s band: 533.43 eV (oxygen bonded to aromatic carbon), 532.03 eV (oxygen single-bonded to aliphatic carbon) and 531.08 eV (oxygen double-bonded to sp^2 carbon). Further information about the **G** functionalization can be obtained by taking into account the signals related to other chemical species, such as N 1s, Si 2p and S 2p.

Indications about the functionalization of materials are obtained carrying out Fourier Transform Infrared Spectroscopy (FT-IR) measurements. The FT-IR spectra of **G** materials is characterized by a band around 1573 cm^{-1} due to the presence of C=C stretching in graphitic domains.⁽³⁰⁾ Moreover, through FT-IR spectra is possible to monitor of the chemical changes of **G** surface. The **GO** spectrum shows several contributes relative to the strong oxidative process such as: the band centered at $\sim 3430\text{ cm}^{-1}$, due to the O-H stretching of hydroxyl and carboxylic acid moieties, the band at $\sim 1719\text{ cm}^{-1}$ due to the C=O stretching of carboxylic acids groups and a peak at $\sim 1046\text{ cm}^{-1}$ attributed to the C-O stretching; in addition, a band at $\sim 2922\text{ cm}^{-1}$ corresponding to C-H stretching of aliphatic sp^3 carbon can be observed.⁽³⁰⁾ FT-IR spectrum of **G-Red** shows a clear decrease of oxygen functional group contribute due to the reduction process by hydrazine

treatment; the observed bands are attributable to residual oxygen functional groups.⁽³⁰⁾

Several microscopy techniques such as Scanning Electron Microscopy (SEM), Transmission Electron Microscopy (TEM) and Atomic Force Microscopy (AFM) are used to investigate the morphology of **G** materials.⁽²⁹⁾ These analyses (Fig. 1.6) give information about the layers distribution and, about the edge of the layers, allowing to estimate their shape and thickness.

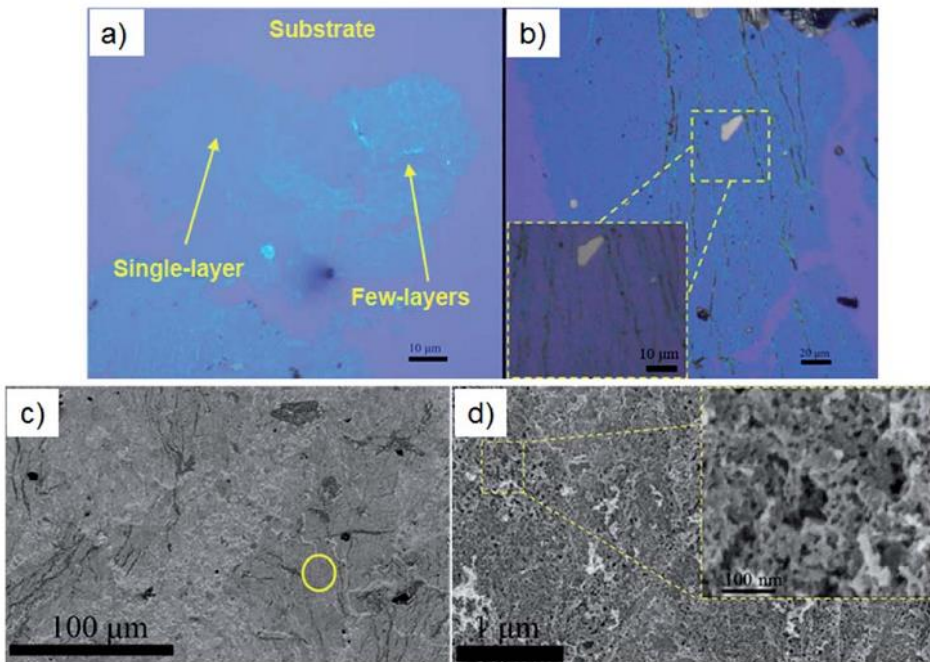


Figure 1.6 (a) and (b) Optical images of graphene layers. (a) Single and a few-layers are indicated with yellow arrows. (b) A layer displaying ripples is shown. (c) and (d) Field emission SEM images (FE-SEM): (c) overview of layers deposited onto the substrate. (d) High magnification of the area marked with a circle in (c), showing the porous structure of the layers.⁽³¹⁾

1.3 Biomedical Applications of **G** Materials

Considering the exceptional properties of **G** materials, they have been object of extensive research in several fields including the biomedical and pharmaceutical ones.^(32, 33) They have been proposed as drug delivery systems for photothermal

and photodynamic therapy, as biosensing materials for nano-theranostic applications and as a scaffold in tissue engineering (Fig. 1.7).⁽³⁴⁾

At the same time, the most important issue is still the potential long-term toxicity concerning **G** and its derivatives.⁽³⁵⁾ By these studies, it was understood that the toxicity of **G**, like other materials previously employed in biomedicine, is strongly dependent on the functionalization degree of its surface. The toxicity of pristine **G** has been demonstrated in several works ⁽³⁶⁾, while suitable functionalized **G** materials shown no toxic effects in the tested dose ranges.⁽³⁷⁾ Other studies have demonstrated that, a suitable functionalization of **G** materials, allows to control their behavior in biological systems and to increase their biocompatibility towards human cells.⁽³⁸⁾ Depending on target application, several synthetic strategies based on covalent or non-covalent binding, have been proposed. Functionalized **G** materials have been obtained by covalent approach, exploiting the reactive groups like carboxylic acid, hydroxyl and epoxy groups widely present on **GO** ⁽³⁹⁾, scarcely on **G-Red** surface. Other approaches are based on hydrophobic interactions, π - π stacking and electrostatic binding.⁽³⁸⁾

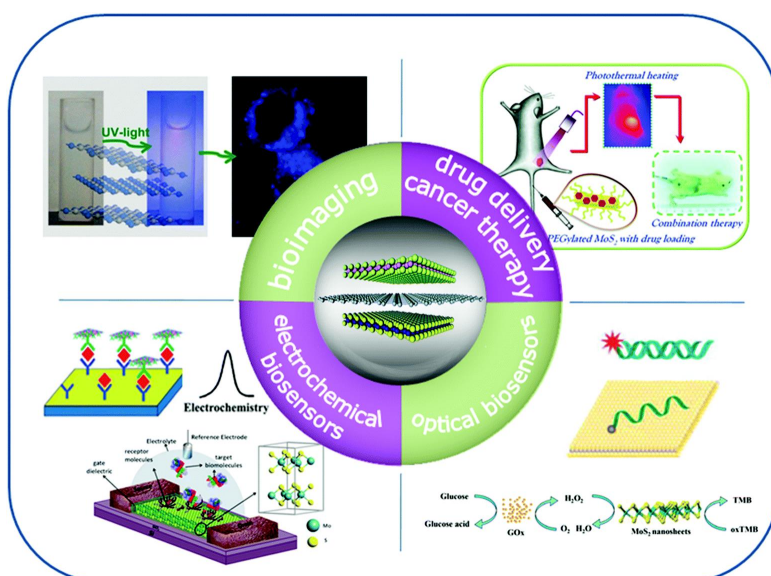


Figure 1.7 Illustration of potential biomedical applications of graphene.

G and its derivatives, due to their high capacity of loading biomolecules on their large surface area, were employed to build several drug delivery systems. The **G** surface, rich of delocalized π electrons, showed high ability of forming complexes with several aromatic drugs by π - π stacking, like doxorubicin (DOX) ⁽⁴⁰⁾, camptothecin (CPT) ⁽⁴¹⁾ and SN38 (irinotecan, an analogous of CPT).⁽⁴²⁾ Both DOX and CPT were loaded on **GO** surfaces, obtaining a synergic cancer cell killing effect, in dose dependent manner.⁽⁴³⁾

The preparation of **G-Red**/DNA complex with a high water solubility was described. During the chemical reduction from **GO** to **G-Red**, the DNA has been introduced by π - π stacking interactions, between **GO** surface and the bases of single-stranded DNA. At the end of chemical reaction, DNA covers the **G-Red** surface. This method was used to develop several DNA biosensors.⁽⁴⁴⁾

An interesting gene delivery system was prepared by functionalization of **GO**, a negatively charged material, with poly-ethyleneimine (PEI), a positively charged polymer, *via* electrostatic interactions. PEI imparts a positive charge to **G** surface, allowing a subsequently loading of DNA or RNA sequences, negatively charged. The system **GO-PEI** showed: *i*) a lower toxicity compared to bare PEI; *ii*) an improvement of physiological stability compared to **GO**; *iii*) high gene delivery transfection efficiency, due to a better protection from action of nuclease enzymes.⁽⁴⁵⁾

Another delivery system, based on **G** materials, was prepared by covalent conjugation of polyethylen glycol (PEG) and chitosane on **GO** surfaces. The conjugation was achieved between the amine groups of PEG/chitosane and the carboxyl groups of **GO**, improving the biocompatibility of carbon material. Moreover, it reduces the non-specific binding to biological molecules and cells, promoting a specific action in anticancer therapy.⁽⁴⁶⁾ Other studies have demonstrated that the covalent conjugation with biomolecules increases the

biocompatibility of **G**. For example **GO** conjugated with dextran (DEX), showed a significant improvement of the stability in physiologic solution with respect to **GO**. The conjugation of **GO** with sulphate biomolecules improves the colloidal stability of **GO** in biological solution.⁽³⁷⁾

GO and **G-red** were also investigated as platforms to prepare systems to be used in theranostic therapy. This is a novel medicine strategy that combines diagnosis and therapy: “all-in-one single platform”.⁽³⁸⁾

The increase in efficacy of a therapeutic formulation is directly related to its ability to selectively target the affected tissue, to overcome the biological barriers and to react smartly to the disease environment by releasing the therapeutic agents.

It has been demonstrated that **G**-based materials with the lateral size of several tens of nanometers offer passive targeting toward tumour sites, and that the conjugation with a targeting agent such as folic acid (FA) confers active targeting due to over-expression of FA-receptors on membrane surfaces of cancer cells.⁽⁴⁷⁾

G materials were also explored for photothermal therapy (PTT) and photodynamic therapy (PDT).

PTT is based on a local increase of temperature that kills the cancer cells, due to an agent that generates heat, under controlled light irradiation. **G** is suitable for this application because it exhibits an important absorption in near infrared region (NIR).⁽⁴⁸⁾ An interesting photothermal system based on **G** materials was obtained by chemical reduction of nanoGO-PEG to ultra small nanoG-Red-PEG, coating with PEGylation phospholipid and finally bonding to the arginine-glycine-aspartic acid peptide chain. This system showed *in vitro* a high efficient and selective cancer cells ablation.⁽⁴⁹⁾ Other works have demonstrated that, the efficient action of these systems depends on the dimensions of **G** materials and on their functionalization degree.⁽⁵⁰⁾ **GO** was also used to build photodynamic systems.⁽⁵¹⁾ In PDT a photosensitizer molecule is subject to appropriate light irradiation, which causes the

local release of reactive oxygen species (ROS) which kill the cancer cells.⁽⁵²⁾ For example, nGO-PEG was conjugated, by noncovalent interactions with zinc phthalocyanine (ZnPc), under Xe light irradiation; this system showed selective cytotoxic effects on tumor cells.⁽⁵³⁾ Also, **GO** functionalized with TiO₂ nanocomposites has shown an important anticancer activity under visible light irradiation.⁽⁵⁴⁾ Another interesting photothermal system consists in **GO** conjugated with chlorine e6 (Ce6), this system under laser irradiation at 633 nm has showed an important anticancer action.⁽⁴⁷⁾

G and its derivatives were also studied for their antibacterial effects. However, literature data are conflicting and unclear results were obtained by different research groups. It was demonstrated that **GO** with respect to **G-Red** and graphite showed the major antibacterial effects on *Escherichia coli*.⁽⁵⁵⁾

G induces an effective membrane damage in Gram-positive bacteria and at the same time, this effect was not observed on membrane of Gram-negative bacteria.⁽⁵⁶⁾ A bactericidal activity of **GO**, coated with silver nanoparticles, for both Gram-negative and Gram-positive was reported.⁽⁵⁷⁾ In contrast with these studies, other works demonstrate that the bacteria grow faster on substrates containing **GO** with, respect to substrates where is absent.⁽⁵⁸⁾

G surface could be decorated with inorganic nanoparticles: Au, Ag Pt, Ni, TiO₂, ZnO, Fe₃O₄ etc.⁽⁵⁹⁻⁶¹⁾

GO-TiO₂ was used in photodynamic therapy.⁽⁵⁴⁾ Nanohybrids obtained by decoration of **GO** with iron oxide nanoparticles (IO NPs) showed interesting applications in biomedical field because the drug release can be controlled by using magnetic forces.⁽⁶²⁾ Moreover, they could be used in magnetic resonance imaging and as contrast agent for cell labeling.⁽⁶³⁾

Nanohybrids of **G-Red** covered with Au NPs, have been used in drug-delivery applications and in bio-imaging.⁽⁶⁴⁾

The potential application of **G** in tissue engineering has been demonstrated during the last years. In particular, it has been proven that the scaffold of chitosan-PVA nanofibers containing **G** is able to control the distribution and the cell proliferation. Considerable attention was attracted on the design of scaffolds for bone tissue engineering. In particular, it was observed a very good attachment and growing of MC3T3-E1 mouse pre-osteoblast cells on a GO-chitosan scaffold covalently bonded.⁽⁶⁵⁾ The authors reported that the cells penetrate the pores of the scaffold and, at the same time, their interconnections were increased. The studies have shown a high quality of the cellular proliferation. Moreover, the combination of chitosan with **GO** avoids the degradation of the polysaccharide.⁽⁶⁶⁾

In summary, literature data suggest a great potential of **G** and its derivatives for biomedical applications. These materials exhibited a large surface area where it is possible to graft a wide variety of drugs and biomolecules. Furthermore, these materials have shown interesting physical and optical properties useful in bio-imaging and for the photothermal therapies. It was very important to understand that a suitable functionalization allows to overcome the associated problems of short life toxicity. Currently, studies about the long life toxicity are less advanced. Recently, **G** materials have been intensively investigated as substrates to be functionalized for SERS (Surface Enhanced Raman Spectroscopy) applications like bio-sensing⁽⁶⁷⁾ or for the detection of molecules or tumour cells.⁽⁶⁸⁾ SERS is a more suitable technique comparing to Raman since the latter often has a very small cross-section and generally, the problem of fluorescence arises. SERS, as the name itself suggests, is a surface phenomenon where the intensity of the signals are enhanced by a factor of $10^{12} - 10^{14}$ ⁽⁶⁹⁾, respect to a common Raman spectrum. SERS phenomenon can be attributed to two mechanisms: the electromagnetic mechanism (EM), due to the strong amplification of the local EM field ⁽⁷⁰⁾ and the chemical effect (CM) that involves the creation of new electronic states generated by the

interaction between the metal and the molecules adsorbed on it.⁽⁷¹⁾ Such new electronic states allow for resonant Raman scattering processes.

The substrates play a crucial role for an effective surface enhancement. In particular, the control of the distances among the localized surface plasmons (LSPs), on a sub-nanometres scale, is a critical parameter to control the EM and therefore the efficiency of SERS phenomenon. In fact, an increase of the distance among the LSPs causes a decrease of coupling between them and, therefore, a decrease of the enhancement factor.

With respect to other materials, **G** layers influence positively both the EM and the CM coupling, enhancing the SERS process. Summarizing **G** shows: *i*) interesting optical properties, *ii*) high surface/volume ratio, *iii*) sub-nanometer scale thickness and *iv*) a great affinity with noble metals.⁽⁷²⁾

Chapter 2:

Graphene: Innovative Material for Biomedical Applications

This chapter deals about the functionalization of **G** material with terminal alkyne units and their synthetic applications by click assembly with azido-functionalized compounds.

2.1 Graphene as platform for drug delivery

Graphene (**G**) and its multifunctional derivatives, due to their advantageous properties, have recently emerged as new and interesting drug nanocarriers. In particular, these resulting **G** systems have showed the potential to be applied for systemic, targeting and local drug delivery.

G materials display many advantages compared with other drug delivery systems:

- the ability to provide high loading capacity for many different drugs and therapeutic molecules (weight ratio of loaded drug to **G** nanomaterials could reach 200%)⁽⁷³⁾;
- their flexibility and capability to be engineered into complex multifunctional drug delivery systems, for combined therapies, a new development which is hardly achievable with other nanomaterials;
- covalent or non-covalent surface modifications can be used to impart specific biological activity to **G** materials, as well as to improve their biocompatibility and colloidal stability.

Although preliminary preclinical studies are encouraging, the clinical applications are still far and require addressing some open challenges. The most critical issue for the biomedical applications of these materials is their biocompatibility and toxicity, which are the primary concerns. Most of the current literature data report that the **G** is a biocompatible material with a low toxicity. In spite of this, some conflicting and unclear results have been reported by different research groups.^(74,75)

However, an agreement has been gradually reached: the functionalization of **G**

materials significantly improves their biocompatibility; this step is essential for designing stable and safe drug delivery nanocarriers. Other important questions regard the development of nanocarriers with reproducible dimensions and properties and the requirement to achieve a deeper understanding of **G**'s interaction with living cells (tissues and organs), especially about the cellular uptake mechanism.

2.2 Graphene nanoplatforms

Among the different subtypes of **G**-based nanomaterials, **GO** is certainly the more investigated one for drug delivery purposes (e.g., compared to pristine **G** and **G-Red**). As-produced **GO** is highly oxidized with a large number of residual epoxide, hydroxyl and carboxylic acid groups on its surface. The reduction of **GO**, with reducing agents (i.e. N_2H_4), restores partially the structure and properties of **G**. In comparison with **GO**, **G-Red** is known to have higher electrical conductivity and optical absorbance, a fact that makes it a more attractive tool for applications in theranostic nanomedicine.⁽³⁸⁾ Therefore, a better understanding of **G-Red** materials behaviour in biological systems is needed to improve their performances inside the nanodevices. It is noteworthy, that both the biocompatibility and the pharmacokinetic profile of **G** depend on the modality of functionalization and on its conjugation with biological compounds.⁽⁷⁶⁾

G-Red sheets, unlike **GO** layers, are hydrophobic with limited aqueous dispersibility. In addition, the existence of high π - π stacking and Van der Waals forces, which facilitate the irreversible aggregation of **G** layers or their restack to graphite, strongly limit the **G-Red** applications. To avoid these phenomena, a suitable **G-Red** functionalization is mandatory in order to make the structural, physical, chemical and electronic properties of the material, suitable to the specific applications.⁽⁷⁷⁾

In my ongoing research program, aimed at the discovery of biocompatible drug delivery systems based on carbon nanomaterials, the interest was focused on the decoration of reduced **G** platform with an alkyne terminated group (**G-Alk**).

The alkyne moieties introduced on the nanoplatform prevent the aggregation of **G** sheets, improve their dispersibility in organic media and, being reactive structural fragments, they can be further functionalized by click chemistry reactions.

Two different synthetic approaches were exploited (Fig. 2.1): *a*) the alkyne units were directly coupled with the azide functionality linked to a target biomolecule; *b*) the alkyne moieties were employed to prepare a reactive azlactone graphene platform (**RAGP**) on **G** sheets. Afterwards, **RAPG** can be very efficiently exposed to ring-opening reactions with functionalized primary amine derivatives. In particular, an aminosilane coupling agent (**APTS**), a biological fragment (glutathione oxide, **GSSG**) ⁽⁷⁸⁾ and a natural enzyme such as Catalase (**Cat**) have been incorporated.

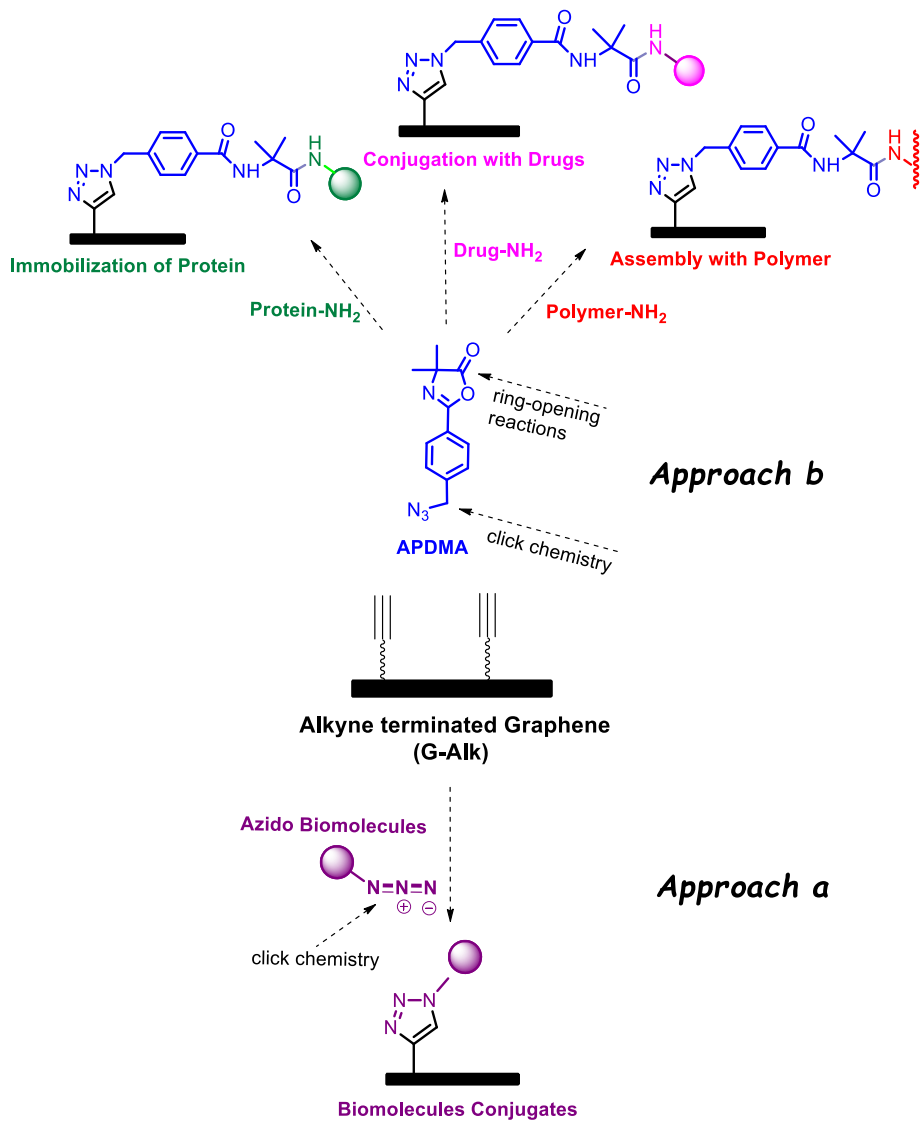


Figure 2.1 Representative scheme of two approaches to insert biological moieties on **G-Alk**.

G-Red was prepared by oxidizing natural graphite powders to graphite oxide, using Hummers method ⁽⁷⁹⁾ and successive exfoliation to **GO**, by ultrasonication. Then, **GO** was reduced with *hydrazine*, under controlled conditions, according to a literature procedure ⁽⁸⁰⁾, to obtain reduced **G** sheets (**G-Red**) (Fig. 2.2).

Graphite, **GO** and **G-Red** have been characterized by TGA, XPS, Raman and TEM analyses. The results are in agreement with literature data. ^(79; 80)

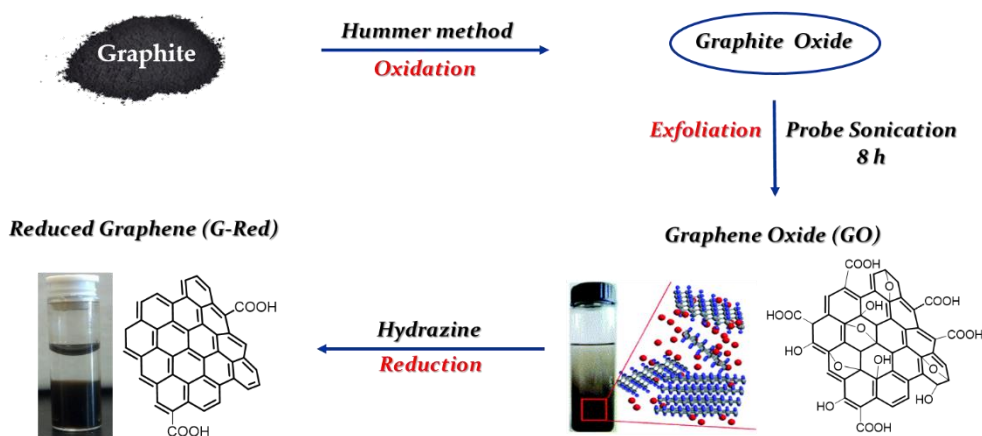


Figure 2.2 Schematic illustration of the preparation of reduced graphene (**G-Red**).

Raman spectroscopy was used to probe structural characteristics of the investigated carbon-based materials, providing useful information on the defects (D-band) related to the vibrations of the sp^3 hybridized carbons, and located at about 1330 cm^{-1} , and in-plan vibration of sp^2 carbon atoms (G-band) centred at about 1580 cm^{-1} . Raman spectra are also characterized by the second-order Raman 2D band (known as D'), which is a defect-independent contribution. The effect of the reduction process on the Raman spectral profiles points out an increased defect density, showing a progressive reduction of the graphitization degree (i.e., of I_G/I_D in Fig. 2.3), confirming the highly disordered structure of the carbon based materials.

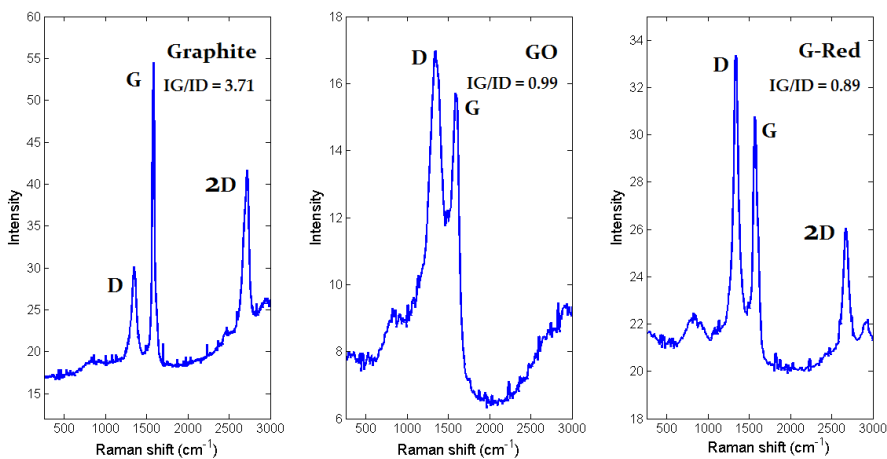


Figure 2.3 Raman spectra of graphite, graphene oxide (GO), reduced graphene (G-Red).

The XPS spectra of graphite, **GO** and **G-Red** (Fig. 2.4), showed the C 1s regions composed by six contributions at about 284.5, 285.8, 286.6, 287.7, 288.9 eV and 291 eV. These contributions are ascribed to C=C/C-C in aromatic ring, C-OH, C-O-C, C=O and OH-C=O and π - π bounds, respectively. The contributions of C-OH, C-O-C, C=O and OH-C=O are completely absent in the graphite spectrum as expected. Conversely, they are prevalent in **GO** spectrum due to the chemical oxidation process. In **G-Red** the chemical reduction process restore in part the sp^2 network, with a decrease of C-OH, C-O-C, C=O and OH-C=O contributes (Tab. 2.1).

TGA analysis results (Fig. 2.5) agree well with Raman and XPS data. The graphite is stable up to 700 °C, unlike **G-Red** and **GO**. The latter shows an overall important weight loss of 51% up to 600 °C, due to the degradation of oxygenated groups, which occur significantly at about $\sim 200^\circ\text{C}$. At variance, **G-Red** being poor of oxygenated groups shows a weight loss of only 15% up to 600 °C.

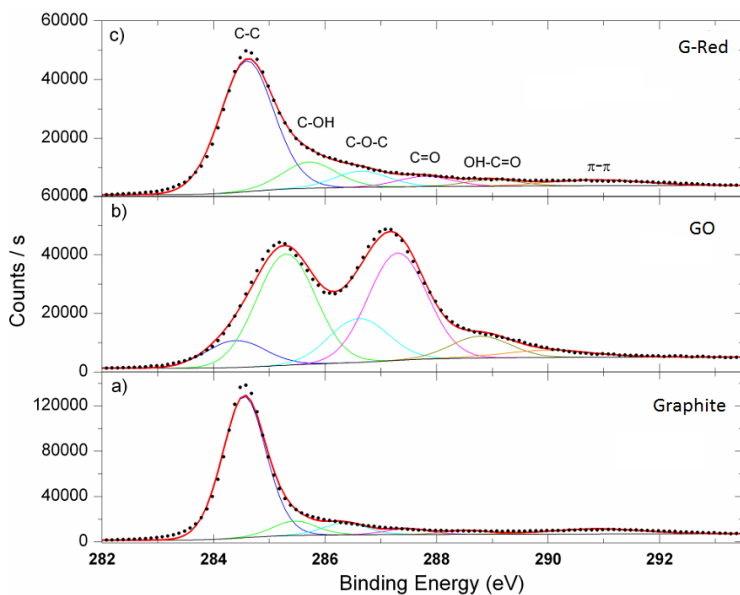


Figure 2.4 C 1s X-ray photoelectron spectra of: (a) graphite; (b) graphene oxide (GO); (c) reduced graphene (G-Red).

Samples	C-C (%)	C-OH (%)	C-O-C (%)	C=O (%)	OH-C=O (%)	π - π (%)
Graphite	74,9	7,6	6,4	3,0	2,0	6,10
GO	8,3	34,5	13,6	33,3	6,8	3,5
G-Red	65,3	13,1	8,1	5,1	3,3	5,1

Table 2.1 Relative percentage of functional groups obtained by fitting the C 1s XPS spectra.

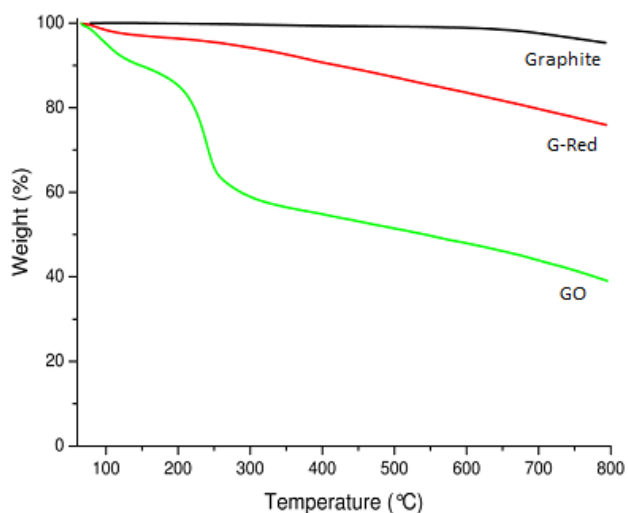


Figure 2.5 TGA profiles of Graphite, GO and G-Red, under N₂ atmosphere.

The morphology of **GO** and **G-Red** was investigated by TEM analysis. (Fig. 2.6). The layers were estimated to be ~100 nm large and ~1-2 nm thick. The sheets of **GO** appear partially folded, due to the large area occupied, while the **G-Red** ones appear homogeneous and quite smooth with little aggregation.

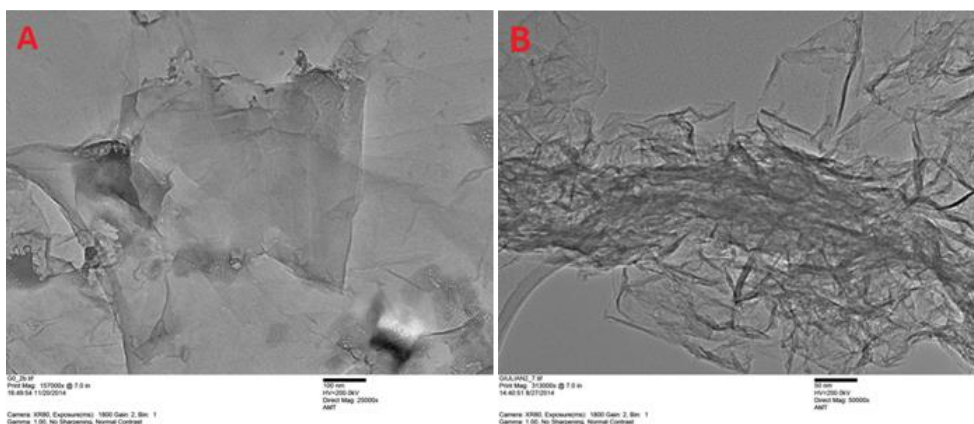
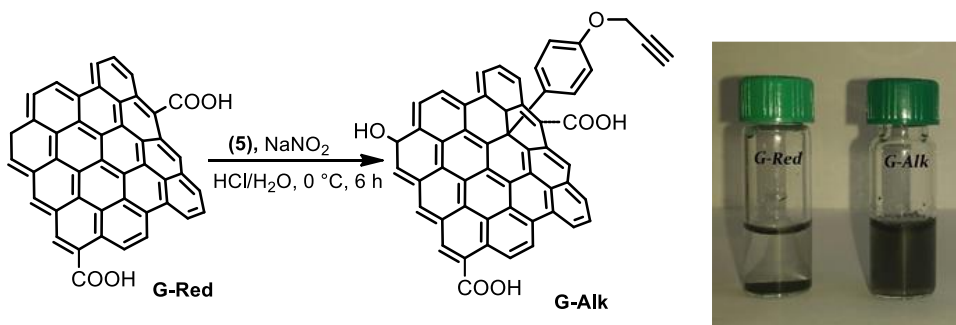


Figure 2.6 TEM images of graphene based materials: **GO** (A), **G-Red** (B).

To prevent the aggregation of **G** sheets, **G-Red** was treated with diazonium compounds to graft the *p*-(2-propynyloxy)-benzene moieties, on the **G** surfaces. The reaction of **G-Red** with *p*-(2-propynyloxy)-benzamine (**5**), sodium nitrite and hydrochloric acid was performed at 0 °C, under continuous sonication (Scheme 2.7). The functionalization of **G-Red** surfaces gave alkyne-terminated graphene materials (**G-Alk**). By TGA analysis it was estimated that **G-Alk** contains 0.8 mmol/g of alkyne moieties and, as expected, it showed a better dispersibility in water with respect to **G-Red** (Scheme. 2.7).



Scheme 2.7 Synthesis of **G-Alk** and photograph of **G-Red** and **G-Alk** dispersed in water (2 mg/mL) three days after preparation.

2.3 Silibinin-Conjugated Graphene Nanoplatfom

Surface modifications of **G** materials with natural biomolecules provide them specific biological activity and improve their biocompatibility. In order to prepare a biocompatible drug delivery system based on carbon nanomaterials, the interest has been focused on the decoration of **G-Alk** surface with Silibinin (**Sil**), a natural flavonoid endowed with several interesting biological properties.⁽⁸¹⁾

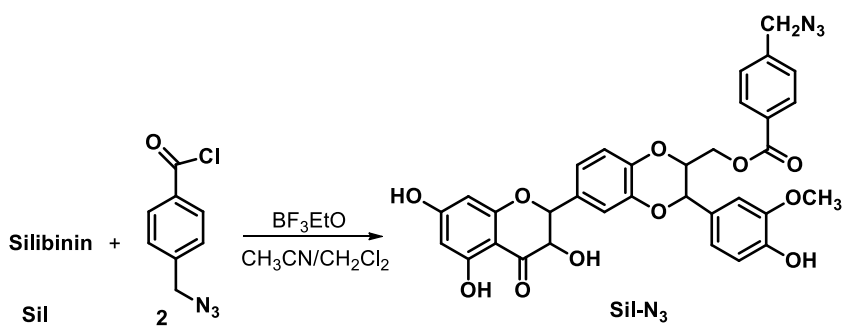
Sil (Fig. 2.8), is the major active constituent of Silymarin, a standardized extract of the milk thistle seeds of *Silybum marianum* employed mainly as dietary supplements to treat a wide range of ailments related to vital organs such as liver and kidney. **Sil** exhibits strong antioxidant activity through scavenging hydroxyl radicals. Recently, it has been extensively studied as hepatoprotective and anti-cancer agent. Studies on cancer prevention, using various cell lines, have demonstrated that **Sil** has a strong inhibitory effect on tumor cell survival and proliferation, efficiently attenuating tumor induced angiogenic response. Currently, **Sil** is in phase II clinical trials in patients with prostate cancer.⁽⁸²⁾

However, the use of **Sil** in the preparation of pharmaceutical products is restricted due to its low solubility in both hydrophilic and lipophilic medium, which greatly reduces its bioavailability and resorbability after oral administration.

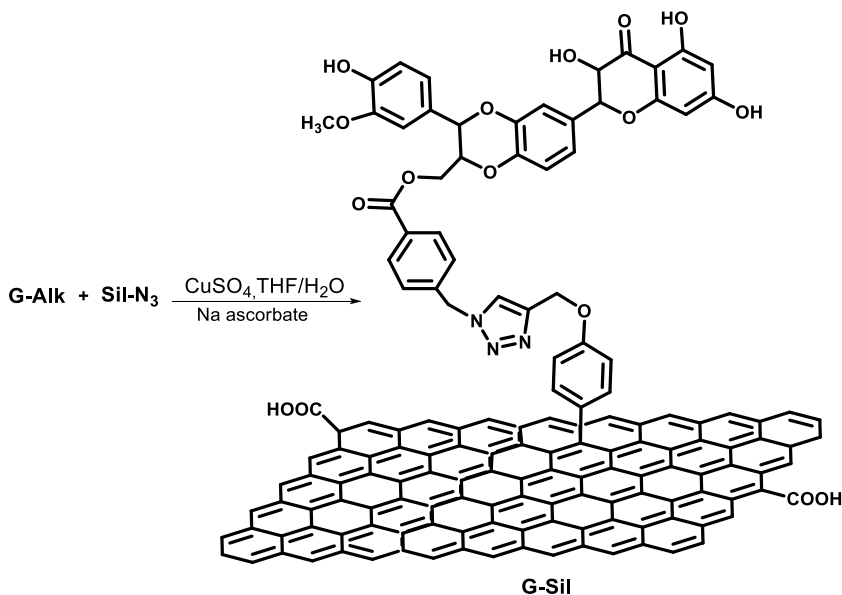
esterification at 23-OH group was performed according to literature protocol.⁽⁸³⁾ The reaction of 4-(azidomethyl)benzoyl chloride (2) and **Sil**, in presence of (BF₃·Et₂O) in acetonitrile/dichloromethane gave the azido-silibinin (**Sil-N₃**), as main product in 48% yield (Scheme 2.9).

The product was purified by flash chromatography and the structure was confirmed with the support of analytical and spectroscopic data.

The click chemistry reaction of **G-Alk** with **Sil-N₃**, using CuSO₄/Na-ascorbate as metal source, gave the **G-Sil** bioconjugate (Scheme 2.10).



Scheme 2.9 Synthesis of Azido-Silibinin (**SilN₃**).



Scheme 2.10 Synthesis of graphene silibinin platform (**G-Sil**).

Unambiguous evidence of **Sil** conjugation on **G-Alk** sheets was provided *via* thermal gravimetric analyses (Fig. 2.11). The TGA profile of **G-Alk** showed a constant mass loss up to 800 °C. A different behavior can be observed in the **G-Sil** curve, which consists of a two-step weight loss profile, corresponding to: *i*) first step (4.8% weight loss <160 °C), removal of solvent and decarboxylation of residue carboxylic acids; *ii*) second step (68.0% weight loss, range 280-600 °C), decomposition of flavonoid moieties linked by triazole fragments. The curve trend above 600 °C suggests a thermal stability of residual material, due to the complete degradation of grafted organic moieties. The high efficiency of the clicking step provides a wide surface loading in the “clicked” **Sil** that causes the relevant weight loss detected in the TGA analysis. From TGA data (Fig. 2.11) the amount of **Sil** grafted on **G-Alk** surfaces is responsible of the weight loss up to 450 °C, corresponding to ~0.82 mmol/g. This value suggested an exclusive linkage of **Sil** to **G** surface by triazole moieties with a quantitative yield in the click reaction (the estimated amount of grafted alkyne moiety on **G-Alk** was ~0.8 mmol/g).

The grafting of **Sil** to **G-Alk** surface has been also confirmed by FT-IR and UV-Vis spectroscopy (Fig. 2.12 and Fig. 2.13). The FT-IR spectrum of **G-Alk** showed the peak at 1641 cm⁻¹, typical of C=C stretching of the **G** skeleton⁽⁸⁸⁾ and the signal of O-H stretching vibrations observed at about 3414 cm⁻¹, due to residual OH and COOH functionalities remaining after *hydrazine* reduction. The expected weak band at about 2100 cm⁻¹ of alkyne moieties is not recognizable. The spectrum of pure **Sil** showed a strong and broad band, due to -OH stretching vibration at 3452 cm⁻¹ and peaks at 1636 cm⁻¹(C=O stretching) and at 1535 cm⁻¹ (C=C skeleton vibration of aromatic ring stretching). The FT-IR bands of **Sil** units resulted clearly observable in the **G-Sil** nanohybrid, with some absorption bands slightly shifted from the values of pure **Sil**, probably due to interactions with **G** nanosheets (formation of hydrogen bonds, conjugation processes, etc.).

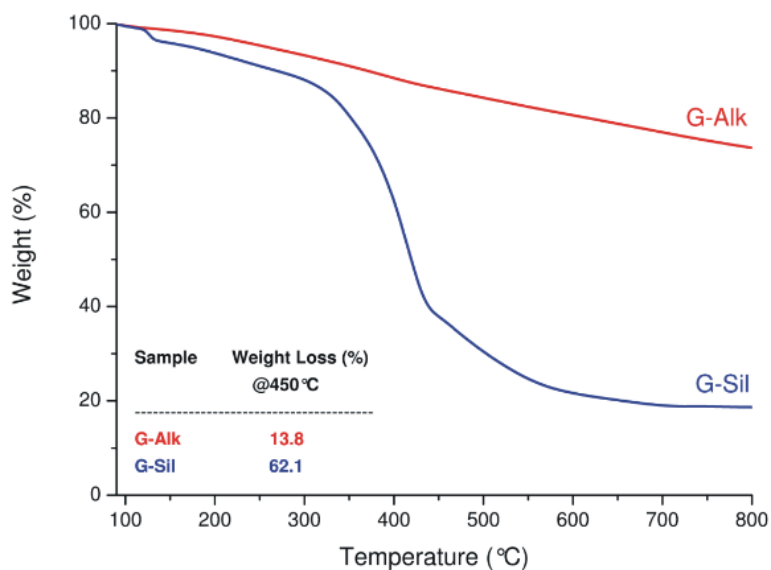


Figure 2.11 TGA profiles of **G-Alk** and **G-Sil** under N_2 atmosphere. The table reports the values of weight loss (%) at 450 °C.

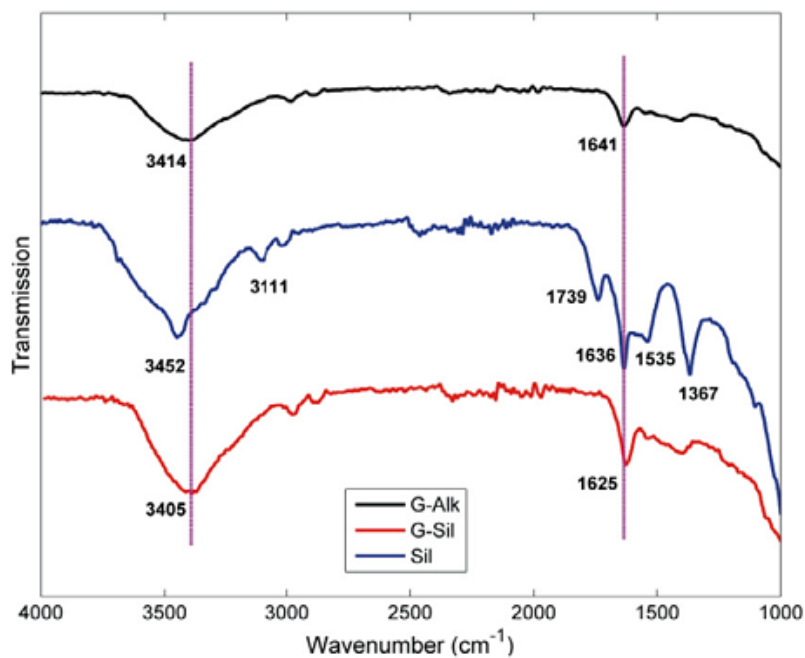


Figure 2.12 FT-IR Spectra of **G-Alk**, **G-Sil** and free **Sil**.

The UV–Vis spectrum of pure **Sil** displayed two characteristic bands: one centred at 286 nm (Band II) and another, less intense (Band I), with a maximum at 324 nm (Fig. 2.13).⁽⁸⁹⁾ The Band II of **G-Sil** bioconjugate is remarkably wider than free **Sil** and slightly shifted towards longer wavelength. The flattening of this peculiar band is plausibly due to the non covalent interactions of the aromatic rings of **Sil** (those ones far from the conjugation sites) with the adjacent graphene nanosheet.

The UV–vis spectrum ($\lambda \geq 230$ nm) of **G-Alk** in DMF/H₂O showed the characteristic pattern of reduced-graphene based materials, while this feature is hidden by **Sil** band in the **G-Sil** spectrum. Moreover, self-recognition phenomena between **Sil** rings cannot be excluded.

The modifications of **G** material, from **G-Alk** to **G-Sil**, is also confirmed by Raman spectroscopy analysis. In the Raman spectrum of **G-Alk** sample, G and D bands, assigned to the in-plane E_{2g} zone-center mode and disorder-induced modes, are centred at 1580 cm⁻¹ and 1332 cm⁻¹, respectively (Fig. 2.14). In **G-Sil** nanohybrid, D and G bands peak intensity is much weaker and slightly shifted towards lower frequency compared to that of **G-Alk** (Fig. 2.14). The attenuation of characteristic peaks suggested a conjugation process, due to the interactions between the **G-Alk** platform and **Sil**. On the other, no changes due to **Sil**-grafting was observed in 2D band (not shown), which presents the characteristic features of a multilayer **G-Alk**. The morphology of functionalized **G** materials was investigated by STEM analyses. STEM images of **G-Alk** showed a large number of homogeneous and quite smooth sheets, overlapping each other (Fig. 2.15 A). On the other hand, the presence of amorphous materials is evident in the **G-Sil** sample (Fig. 2.15 B) and the **G** sheets appear mainly bundled together

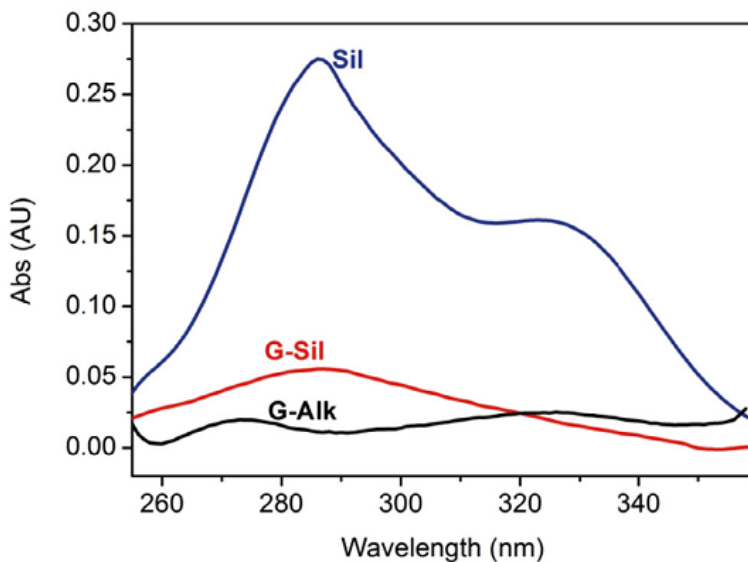


Figure 2.13 UV-Vis spectra of *Sil*, *G-Alk* and *G-Sil*. Normalized spectrum of *Sil* ($[Sil] = 400 \mu M$) is 25 times more intense with respect to the reported trace.

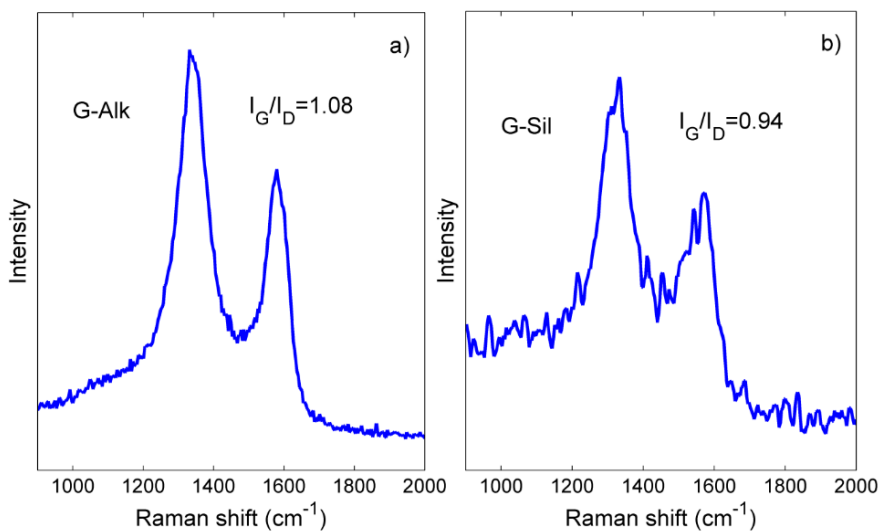


Figure 2.14 Raman spectra of *G-Alk* and *G-Sil* samples.

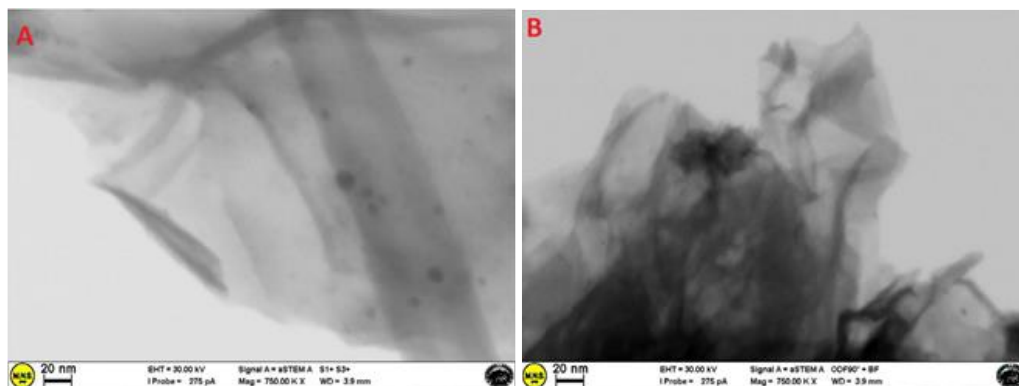


Figure 2.15 STEM images of **G-Alk** (A) and **G-Sil** (B).

Preliminary *in vitro* studies on **G-Alk** and **G-Sil** nanoplateforms were performed in order to evaluate the cytotoxicity of **G** materials as well as cell-based assays to test the anti-cancer effect of the Sil bioconjugate (**G-Sil**). **G-Alk** evaluation showed the total absence of cytotoxicity towards both mesenchymal stem cells (MSCs) and human MG63 osteosarcoma cell line.

For all the tested concentrations, no statistical differences have been recorded between **G-Alk** and the group of cells alone (Fig. 2.16). No apoptotic cells were detected after 48h of incubation of the cultures with **G-Alk** (Fig. 2.16). The fact that **G-Alk**, even at the high concentration of 1000 $\mu\text{g/ml}$, did not affect the viability of the cells, especially that of MSCs, highlights the cytocompatibility of this material, providing new perspectives for its use in biomedical applications. In order to estimate the likelihood of using this nanoplateform for the preparation of a drug delivery system, the effects of **G-Sil** on MSCs and MG63 cells were tested *in vitro* to find out if **Sil**, bound to the **G-Alk** platform, maintained its anticancer properties. It is well known that **Sil** exhibits a strong inhibitory effect on tumor cell survival and proliferation, and efficiently attenuates tumor invasion.⁽⁹⁰⁾ Important anticancer effects have been also detected against osteosarcoma, the most common primary malignant tumor of bone.⁽⁹¹⁾ Two different concentrations of **Sil**, as free compound

and as bioconjugate with **G** materials, were tested. The results showed that 100 $\mu\text{g/ml}$ of free **Sil** feebly reduces the cell viability of MG63 and MSCs, at variance with that of the cells alone (Fig. 2.17).

Interestingly, **Sil** maintains its inhibitory effect against MG63 cells also after conjugation with **G-Alk** and it did not affect the viability of MSCs. It is possible to hypothesize a retarded uptake process, cell type-dependent, which could reduce the **G-Sil** cytotoxicity on MSCs with respect to free **Sil**. A similar behaviour was reported for Sil-loaded lipid nanoparticles.⁽⁹²⁾

These results are a very important starting point to put down the basis for future characterization of these **G** based materials in more complex biological systems. Further investigations and exploitations are needed to evaluate the potential of the **G-Sil** nanohybrid as co-delivery system in the combined anticancer therapy, which nowadays remains the most challenging task to deal with in the field of the nanomedicine.

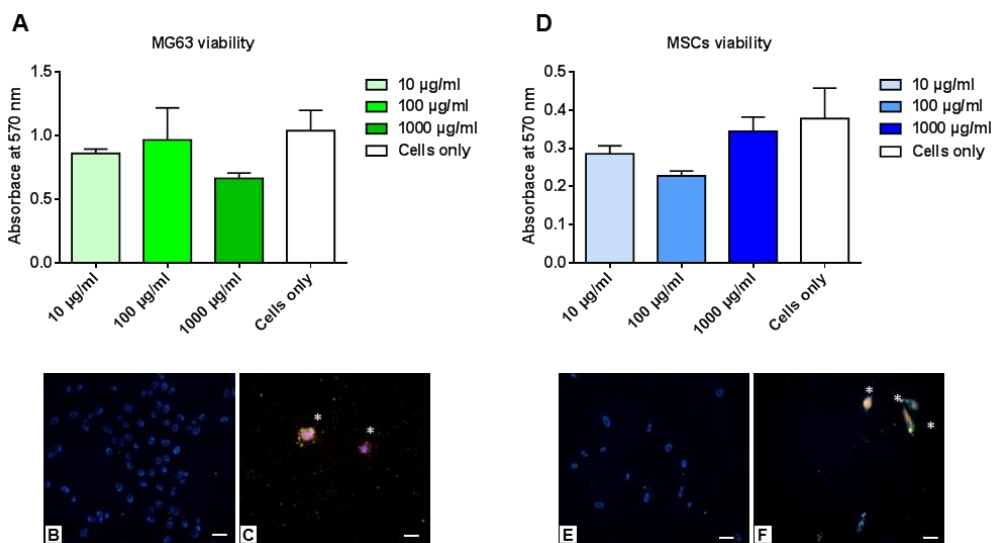


Figure 2.16 **G-Alk** cytotoxicity assay. The graphs showed totally absence of **G-Alk** toxicity on MG63 (A) and MSCs (D) cells after 48h of culture assessed by MTT test. No statistical differences exist at all the tested **G-Alk** concentrations compared to cells only. Noapoptotic MG63 cells (B) and MSCs (E) were observed after the treatment with 100 $\mu\text{g/ml}$ of **G-Alk** at 48h. Dead MG63 cells (C) and MSCs (F) were observed in positive control. Cells nuclei in blue, apoptotic cells in green (*), nuclear localization of Dox in red. Scale bars: 50 μm .

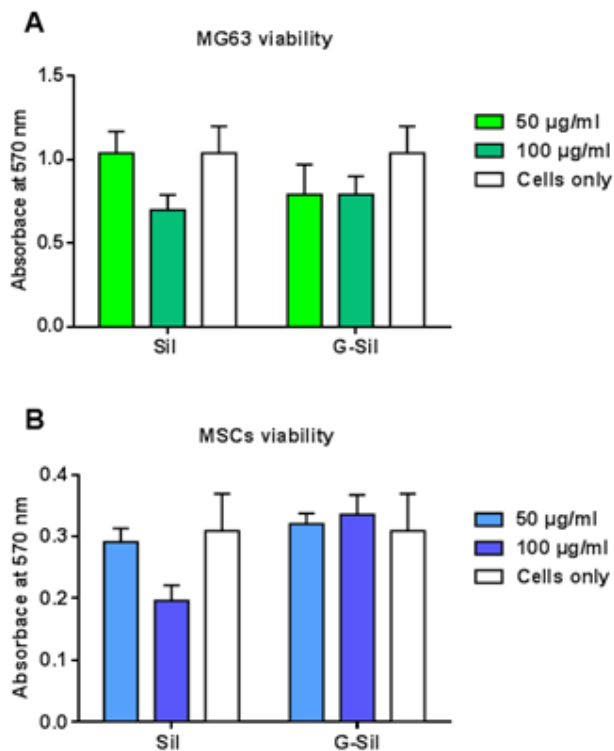


Figure 2.17 Cell viability assay. MG63 cells (A) and MSCs (B) viability assessed by MTT assay after 48h of culture with different concentrations of free *Sil* and *G-Sil* bioconjugate.

2.4 Reactive Azlactone Graphene Platform (RAGP)

Azlactones (*oxazol-5-(4H)-ones*) are multifunctional compounds that contain numerous reactive sites (the electrophilic centres at C2 and C5; the nucleophilic site at C4; the azomethine ylide 1,3-dipole), allowing a wide variety of transformations (Fig. 2.18). Recently, they were employed as mesoionic azomethine ylides in the functionalization of carbon nanomaterials such as fullerenes and carbon nanotubes.^(93, 94)

The *4,4-dimethyl-5-oxazolone* was studied in industry for many years by groups at 3M, Polaroid, Rohm and Haas GmbH; recently, 4,4-disubstituted azlactones have been used as a way to modify polymer surfaces.⁽⁹⁵⁻⁹⁷⁾ In presence of two

substituents at the C4 position, the reactivity as a nucleophile or azomethine ylide is forbidden and the lactone-based functional group displays only high reactivity toward nucleophilic agents, such as primary amines, alcohols and thiols by means of a ring-opening addition reaction.⁽⁹⁵⁻⁹⁸⁾

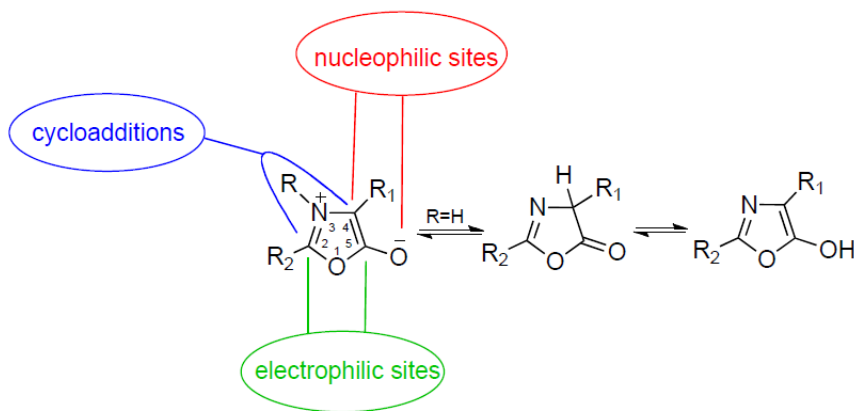
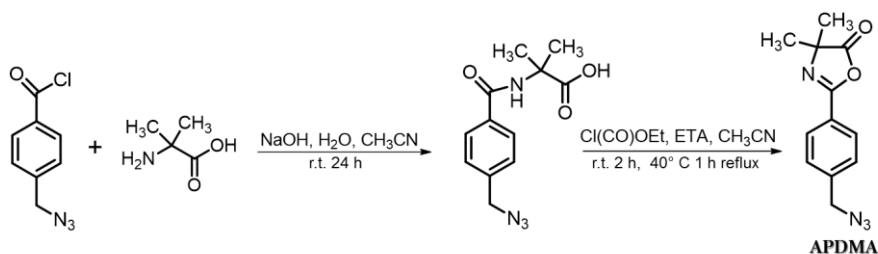


Figure 2.18 Representative scheme of reactive sites of oxazolone

Along my research activity, particular attention was addressed on the development of an efficient and versatile approach to introduce a pendant oxazolone functionality on **G-Alk** surfaces (Approach *b*, Fig. 2.1). The integration of the azlactone functionality into **G** is appealing because, no activation or pre-treatment is necessary for the post-functionalization of **G** based materials, since they are more stable to hydrolysis than activated esters, and no side reactions are expected during functionalization. Furthermore, it is envisaged that the range of applications for which azlactone-functionalized **G** materials can be tailored is both broad and diverse. It could include the design of drug delivery systems, or the fabrication of supports for the immobilization of biomolecules and direct implications for the development of novel biosensors, in the context of nanoscale detection of pathogens and other metabolites related to human health issues. Moreover, the reactive

azlactone **G** platform could be suited for the deposition of **G** films on the surfaces of amine functionalized polymers.

The reactive azlactone graphene platform (**RAGP**) was built by click scaffold assembly of an alkyne and an azide fragments. The terminal alkyne moiety was grafted on graphene surfaces (**G-Alk**), while the azide group was introduced in the azlactone fragment (**APDMA**). The azlactone fragment **APDMA** was prepared by sequential acylation–cyclodehydration involving a two-step procedure (Scheme 2.19). The first step is a Shoeten-Baumman reaction, between the 4-(azidomethyl)benzoyl chloride and the 2-amino-2-methylpropanoic acid. The intermediate was subjected to a cyclodehydration reaction, induced by ethyl chloroformate, to obtain the oxazolone fragment (**APDMA**). The structure of **APDMA** was supported by ^1H NMR, ^{13}C NMR and FT-IR analysis; in particular the FT-IR spectrum of **APDMA** showed the strong stretching bands at 2097 cm^{-1} ($\nu\text{ N=N=N}$), 1818 cm^{-1} ($\nu\text{ C=O}$), 1652 cm^{-1} ($\nu\text{ C=N}$) and 1200 cm^{-1} ($\nu\text{ C-O-C}$) (Fig. 2.20), characteristics of oxazolone structure.



Scheme 2.19 Synthesis of azido-azalactone (**APDMA**).

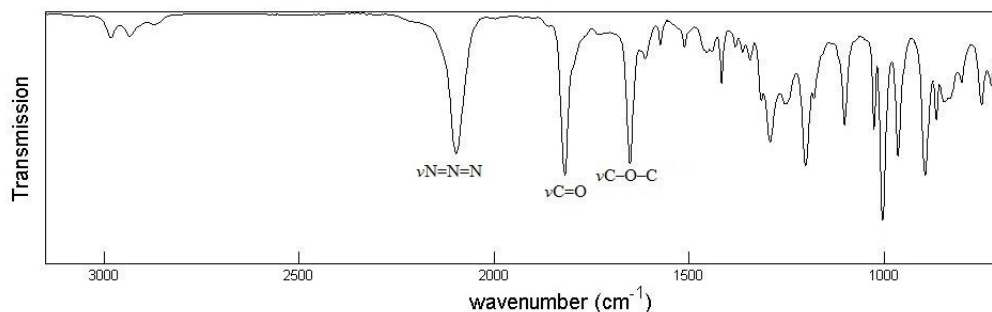
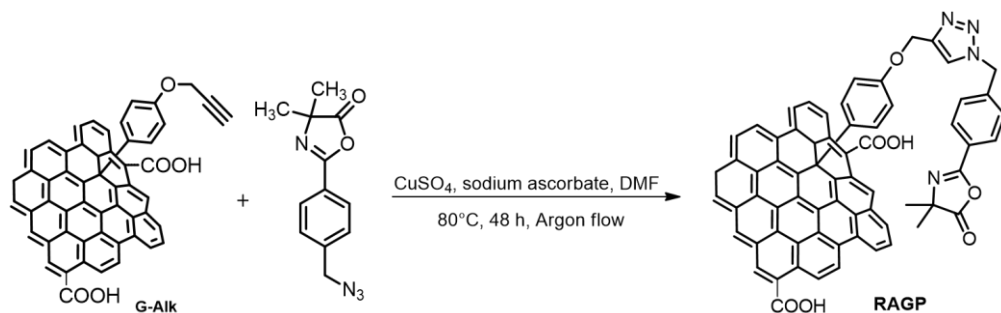


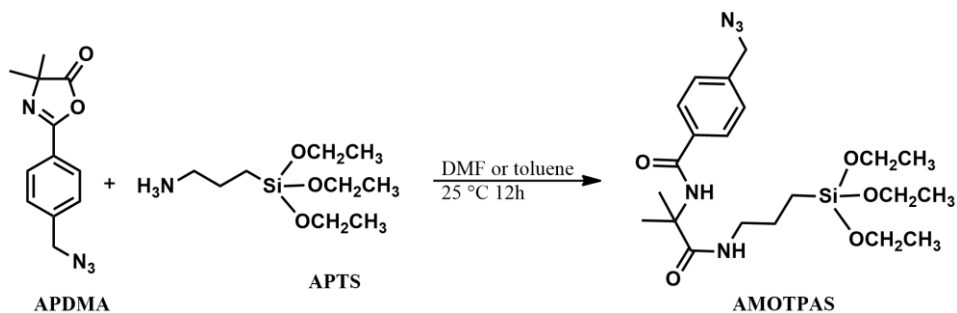
Figure 2.20 FT-IR spectrum of **APDMA**.

The click chemistry reaction between **APDMA** and **G-Alk**, using CuSO_4/Na -ascorbate as the metal source⁽⁹⁹⁾, led to the reactive azlactone graphene platform (**RAGP**) (Scheme 2.21).



Scheme 2.21 Synthesis of reactive azalactone graphene nanoplateform (**RAGP**).

Once the appropriate **RAGP** structure was obtained, it was important to quantify the ring opening efficiency of azlactone, in order to proceed with further functionalizations of the nanoplateform. A study of the experimental conditions to optimize the efficiency of the ring-opening reaction was carried out by treating, in toluene without catalysts, one equivalent of **APDMA** with one equivalent of *aminopropyltriethoxysilane* (**APTS**), chosen to act as a nucleophilic agent (Scheme 2.22). FT-IR and ^1H NMR analyses of the crude reaction mixture confirmed the presence of the coupling product, without observable side reactions (Fig. 2.23). The downfield shift of resonance of amino methylene protons (peak c, Fig. 2.23) from 2.45 to 3.31 ppm, the disappearance of characteristic azalactone absorption at 1818 cm^{-1} and the presence of the carbonyl amide group signal at 1649 cm^{-1} (Fig. 2.23) indicate the formation of the coupling compound with 100% atom efficiency. Hence, the same procedure was applied for the post functionalization of **RAGP** using **APTS** and **GSSG** (*glutathione oxidized*), (Scheme 2.24).



Scheme 2.22 Ring opening reaction an azide-azalactone moiety.

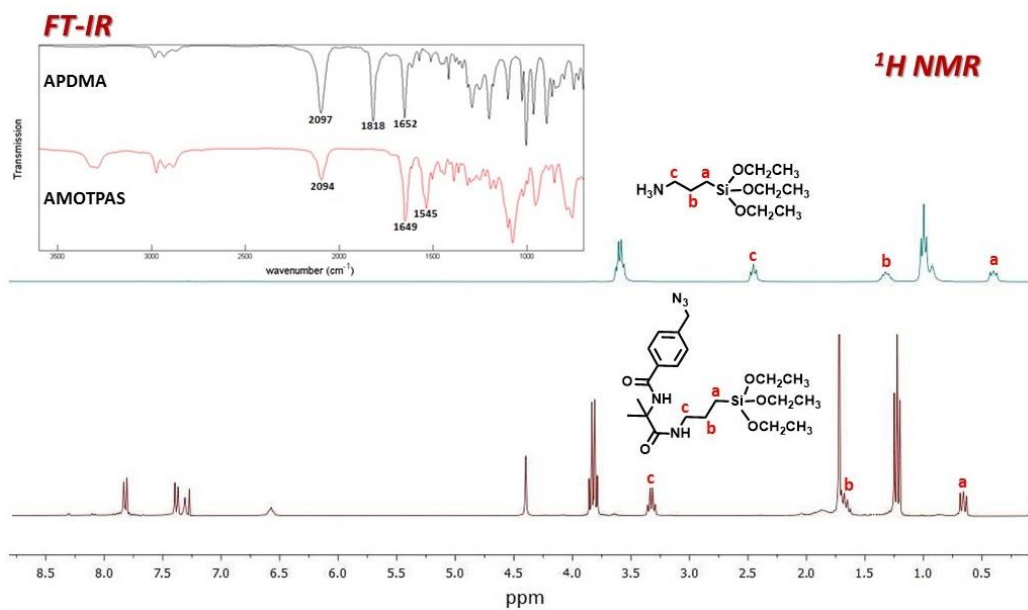
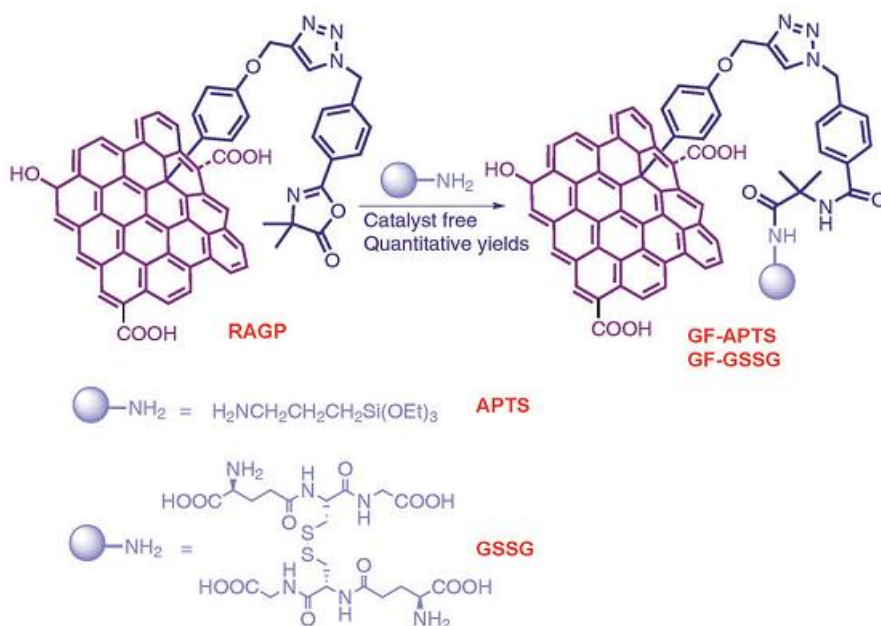


Figure 2.23 ¹H NMR of APTS and crude of ring opening reaction. The inset shows the IR spectrum of APDMA and the crude of ring opening reaction.



Scheme 2.24 Schematic illustration of ring opening reactions on **RAGP** with primary amines to give graphene functionalized materials (**GF-APTS** and **GF-GSSG**).

The pristine and functionalized graphene platforms were characterized by TGA, TEM, XPS, FT-IR and Raman spectroscopy.

The thermal gravimetric analyses (TGA) provides a clear evidence of the grafting of organic groups. In fact as reported previously, **G-Red** shows much higher thermal stability with a constant mass loss up to 800 °C, the TGA curve of **G-Alk** shows a minor thermal stability, with no significant change in profile (Fig. 2.25). A different behavior can be observed in the **RAGP**, **GF-APTS** and **GF-GSSG** profiles, where the rapid weight loss at about 500 °C can be attributed to the decomposition of the organic component linked by the azlactone fragment.

The presence of functional groups on the **G** surface is confirmed by FT-IR spectra. In Fig. 2.26 are shown selected region of **RAPG**, **GF-APTS** and **GF-GSSG** FT-IR spectra. The C=C stretching band at 1590 cm^{-1} of **G** is present in all the samples. The signal of C=O amide group at about 1630 cm^{-1} , is indicative of the coupling of amine

groups with azlactone moiety. Both in **GF-APTS** and **GF-GSSG** spectra the strong bands, located approximately at 2800 and 2900 cm^{-1} corresponding to sp^3 C-H stretching, are present.

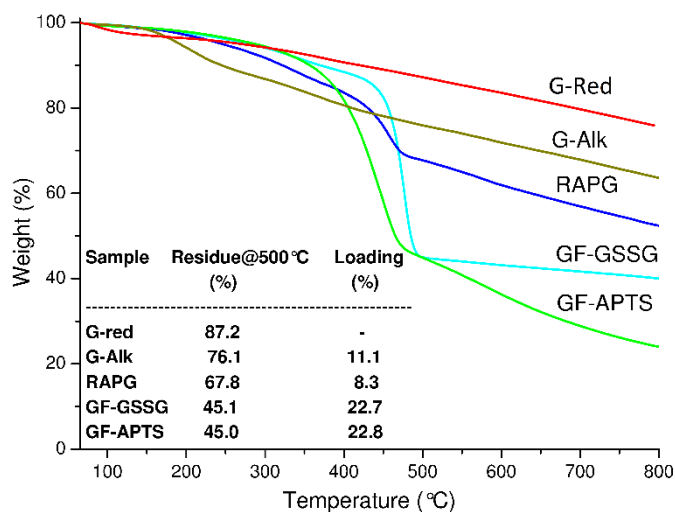


Figure 2.25 TGA profiles of **G-Red**, **G-Alk**, **RAGP**, **GF-GSSG**, and **GF-APTS**, under a N_2 atmosphere. The table reports the values, at 500 $^{\circ}\text{C}$, of weight residue (%) and loading(%).

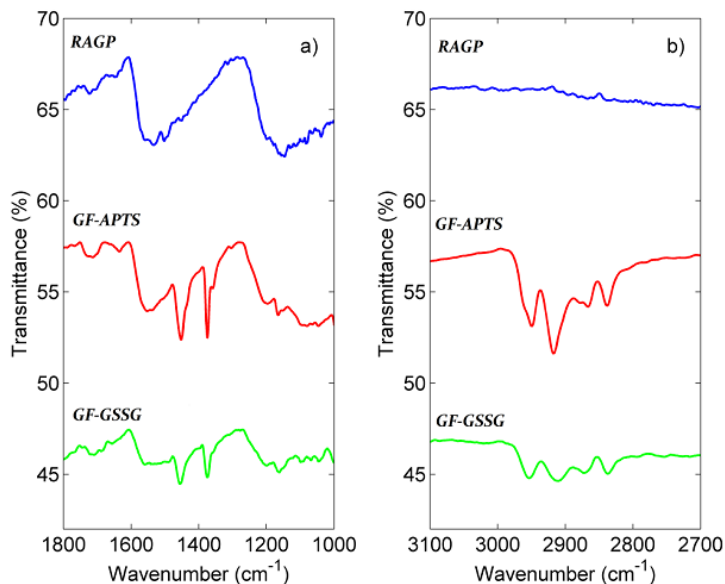


Figure 2.26 FT-IR spectra of **RAGP**, **GF-APTS** and **GF-GSSG** samples.

In Raman spectra (Fig. 2.27), since functionalization causes an increase of the structural disorder in the graphitic lattice (e.g. the sp^2 -defect), the I_G/I_D ratio decreases from 1.08 in the **G-Alk** sample down to 0.61 in the **GF-APTS** one. In the **GF-APTS** and **GF-GSSG** samples, the D- and G-bands bands slightly shift towards higher wavenumbers (from 1312 cm^{-1} and 1580 cm^{-1} in **RAGP** sample up to $1332\text{--}1341\text{ cm}^{-1}$ and $1588\text{--}1608\text{ cm}^{-1}$ in the **GF-APTS** and **GF-GSSG** ones, respectively) as an effect of the electron transfer from graphitic lattice to oxygenated moieties, as confirmed by FT-IR and XPS analyses. Thus, the typology of oxygenated functionalities have a significant impact on the wavenumber position of D and G bands. The addition of **APTS** and **GSSG** reflect also on the width (FWHM) of the Raman bands. FWHM slightly decreases, hinting a shrinkage of the distributions of the angles and lengths of C bonds as well as of the strains.

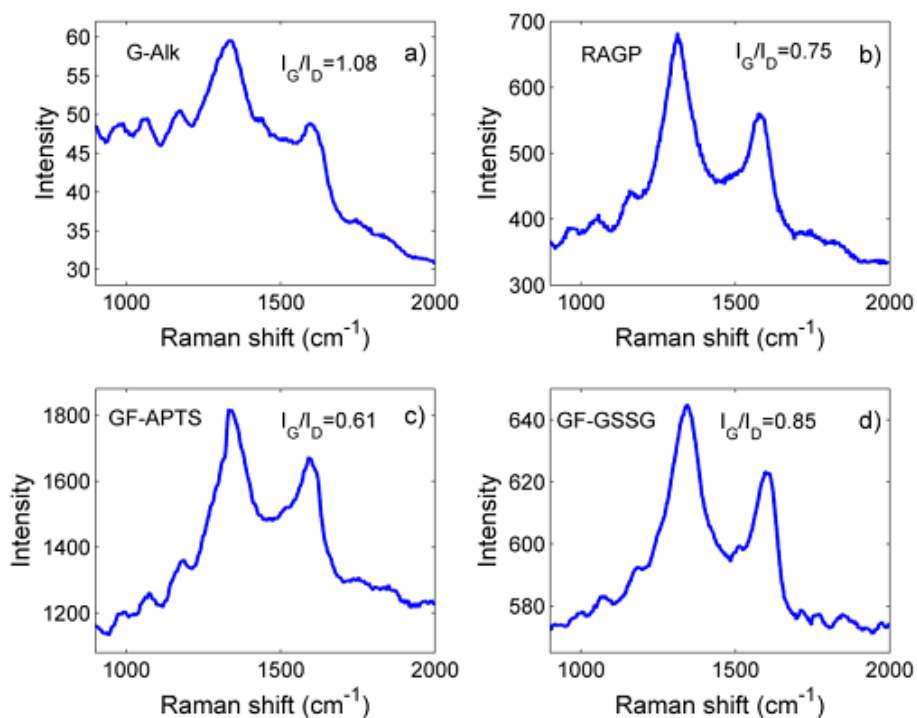


Figure 2.27 Raman spectra of (a) **G-Alk**, (b) **RAGP**, (c) **GF-APTS** and (d) **GF-GSSG** samples.

In XPS spectra (Fig. 2.28) the C1s bands were deconvoluted using six contributions: a main contribution at 284.5 eV attributed to C=C/C–C in the aromatic ring and four other contributions at higher binding energies corresponding to carbon atoms bonded to oxygen in different surface functionalities (C–OH, C–O–C, C=O and OH–C=O) centered at 285.8, 286.6, 287.7, and 288.9 eV, respectively. The contribution at about 291.0 eV refers to π – π bonds.⁽¹⁰⁰⁻¹⁰²⁾ As expected, the percentages corresponding to C–C and carbon oxidized contributions are almost unchanged from **G-Alk** to **RAGP** sample (Table 2.2). On the other hand, the addition of **APTS** induces an evident decrease in the degree of surface carbon oxidation (Tab. 2.2). This behavior is directly related to the symmetrical and shrunk Si 2p and O 1s lineshape features. Particularly, the position of the Si 2p band at 102.0 eV is indicative of silicon–oxygen bonds in silanes (Fig. 2.29 c, Table 2.3).⁽¹⁰³⁾

The **GF-GSSG** sample is characterized by the presence of S–S bonds at 164.0 eV and, to a lower extent, by oxidized sulphur bonds at 168.0 eV (Fig. 2.30 d). The **GF-GSSG** and **RAGP** samples show only slight differences in terms of carbon-oxidized phases. Finally, the N 1s lineshapes showed a similar profile in all the samples, but its intensity decreases in the functionalized samples (**GF-APTS** and **GF-GSSG**) (Fig. 2.29 b, Table 2.3).

The morphology of based and functionalized graphene materials was investigated by TEM analyses (Fig. 2.30). The TEM micrograph of **GO** showed partially folded layers, while the **G-Red** and **G-Alk** ones showed the presence of quite homogeneous and smooth sheets, with little aggregation. The TEM images of **RAGP** clearly show a planar backbone conformation and transparency with ripple lines between the layers. The presence of well-defined edges revealed a large number of thin sheets of **G**. In the amine functionalized **G** materials there are very

noticeable layers of amorphous materials due to the **APTES** or **GSSG** residue bound on both surfaces of **G** sheets.

Elemental mapping information were obtained by STEM analyses (Fig. 2.30). STEM analyses are in good agreement with XPS results which show that the graphene nanomaterials have different C, O, Si and S contents, as expected on the basis of the chosen functionalization (Fig. 2.30). Three elements as carbon, oxygen and nitrogen are dispersed in the samples. The content of these three elements is similar in **RAGP** and **GF-APTS**, respectively, whereas it is reduced in **GF-GSSG**. The lower amount of peculiar elements as S in **GF-GSSG**, respect to Si in **GF-APTS**, suggested an additional grafting of **APTS** on the **G** surfaces, probably on residual phenolic and carbonyl groups.

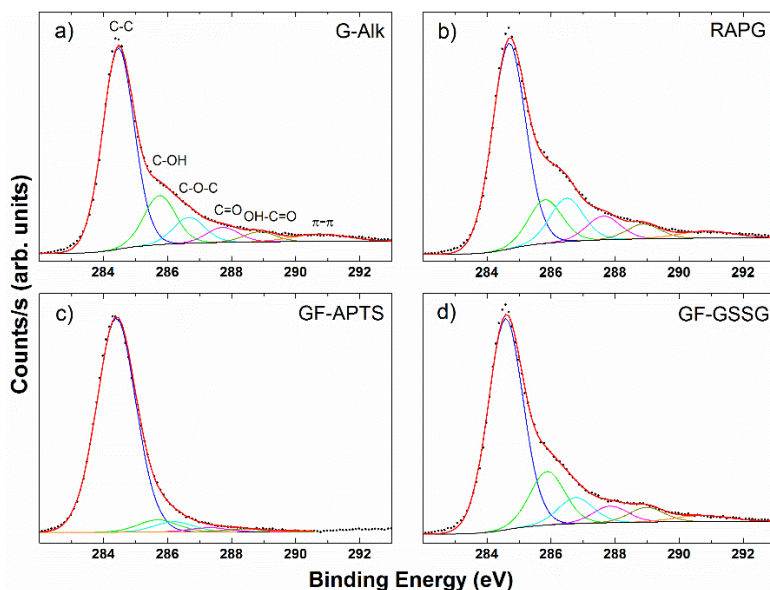


Figure 2.28 C 1s bands of XPS spectra of **G-Alk** (a), **RAGP** (b), **GF-APTS** (c), and **GF-GSSG** (d).

Samples	C-C (%)	C-OH (%)	C-O-C (%)	C=O(%)	O-C=O(%)	π - π (%)
G-Alk	64,2	15,7	8,3	4,8	3,2	3,8
RAGP	60,0	12,7	12,8	6,9	4,3	3,3
GF-APTS	87,2	5,0	4,2	1,8	1,3	0,5
GF-GSSG	63,7	16,2	7,9	5,0	4,4	2,8

Table 2.2 Atomic content percentage and bonding fraction percentage by XPS analysis.

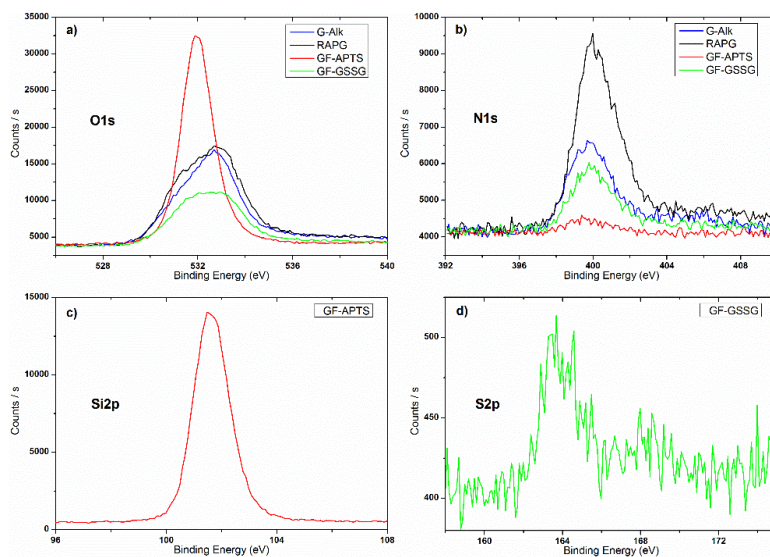


Figure 2.29 O 1s (a), N 1s (b) bands of XPS of **G-Alk**, **RAGP**, **GF-APTS**, and **GF-GSSG**. Si 2p (c) and S 2p (d) XPS bands of **GF-APTS** and **GF-GSSG** respectively.

Samples	Si (%)	S (%)	Cl (%)	C (%)	N (%)	O (%)	Sn (%)	F1s (%)	Cu2p (%)
G-Alk	0,6	-----	0,3	83,9	3,7	11,1	0,1	0,3	-----
RAGP	0,4	-----	0,2	79,3	6,0	13,0	0,1	0,6	0,4
GF-APTS	21,5	-----	0,2	56,6	0,9	20,1	-----	0,7	-----
GF-GSSG	1,0	0,3	0,4	80,9	3,6	12,8	0,3	0,3	0,4

Table 2.3 Atomic content percentage and bonding fraction percentage by XPS analysis.

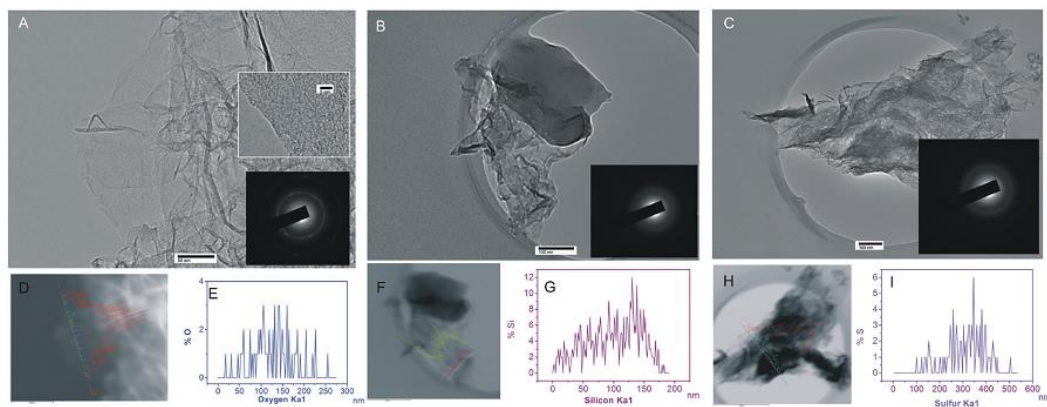


Figure 2.30 TEM (A–C) and STEM (D, F, H) images with line scans and corresponding total element percentages, detected by peculiar emission lines (for colours see ESI, † Fig. S9–S11). (A, D) **RAGP**; (B, F) **GF-APTS**; (C, H) **GF-GSSG**. Inset of (A–C) SAED patterns of each sample area; (E) % of O in **RAGP**; (G) % of Si in **GF-APTS**; (I) % of S in **GF-GSSG**.

From TGA, XPS and STEM analyses the amounts of **APTS** and **GSSG** grafted onto **G** surfaces were estimated to be ~ 1 mmol/g and ~ 0.3 mmol/g, respectively. These values suggested an exclusive linkage of **GSSG** to **G** surfaces by the azlactone moiety in a 1:1 molar ratio, because the estimated amount of the linked oxazolone moiety on **RAGP** was ~ 0.3 mmol/g; for **APTS** an additional grafting occurred.⁽¹⁰⁴⁾ Probably, based on experimental results and according to literature data⁽¹⁰⁵⁾, additional reactions between the silyl group of **APTS** and the phenolic and carboxylic groups occurred, when **RAGP** was treated with **APTS**. The structure proposed for **GF-APTS** product has been reported in Fig. 2.31.

In the case of functionalization with **GSSG** the residue carboxylic groups cannot react with amino groups of **GSSG** without a coupling reagent.

In conclusion, it has been demonstrate that azlactone moieties grafted by the click chemistry reaction on reduced functionalized **G** might be useful as a reactive platform for the rapid engineering of **G** based materials with functionalized primary amines. The reactive platform shows a high yield of silane grafting with respect to graphene silylation methods provided in the literature. Moreover, it can be employed for the selective conjugation of compounds of pharmaceutical and biological interest such as **GSSG**.

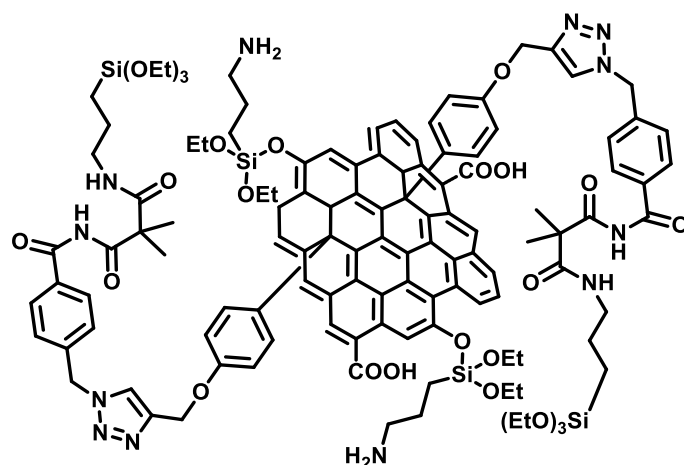


Figure 2.31 Proposed structure of **GF-APTS**.

2.5 Catalytic Properties and Immobilization Studies of Graphene Catalase Bioconjugate (G-Cat)

As previously reported **G** materials are able to influence the activity of biomolecules linked on their surface like enzymes, proteins, antigens, antibodies, etc.⁽¹⁰⁶⁻¹⁰⁸⁾ In a recent work is reported the preparation of a biosensor system with high capacity to detect H₂O₂, a molecule involved in cellular oxidative damages. This biosensor is a hybrid system where horseradish peroxidase enzyme was immobilized onto suitable functionalized **G** film. The conjugation of horseradish peroxidase with **G** improves its catalytic activity and its storage stability up to one month. Indeed the system exhibits a higher sensitivity for the detection of H₂O₂, respect to the enzyme alone.⁽¹⁰⁹⁾

Other enzymes are investigated to prepare hybrid **G**-based systems and most of results indicated an improvement of the enzyme's activity due the **G**'s ability to affect the enzyme conformation.

In this contest, attention was focused to test the ability of our graphene platform, **RAGP**, to link onto its surface an enzyme, Catalase (**Cat**). Moreover, the **G** capability to influence the **Cat** activity was investigated.

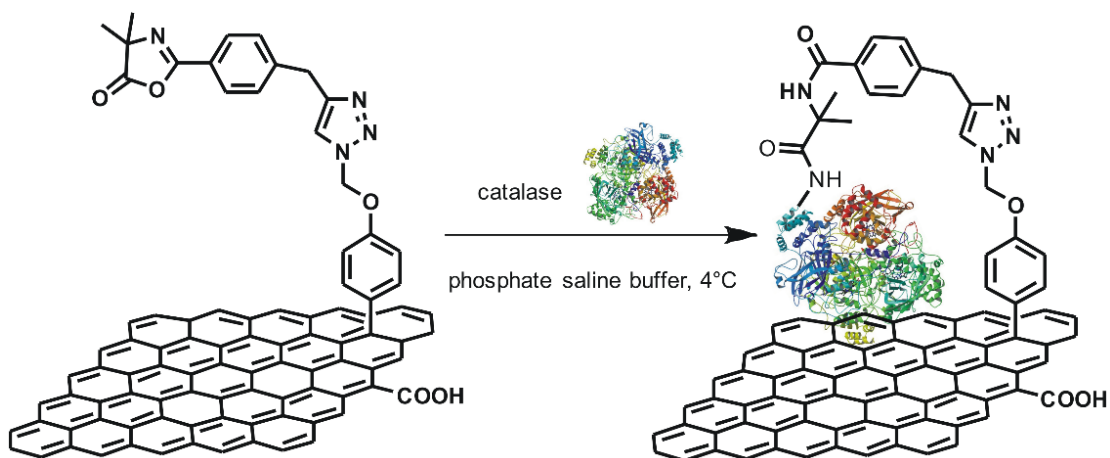
The catalase (**Cat**) is a tetrameric iron porphyrin protein, essential antioxidant agent, which is able to protect the cells from strong oxidation damages induced by H₂O₂. This enzyme is able to catalyze the dismutation process of H₂O₂ in oxygen and water, without generating free radicals.⁽¹¹⁰⁾ For this important activity, **Cat** has been selected as model protein to prepare a hybrid system, which could be useful to prevent the oxidative damages of human cells.

Hybrid materials obtained by adsorption of **Cat** on carbon nanomaterials such as **GO**⁽¹¹¹⁾, **G-Red**⁽¹¹²⁾, fullerene, carbon nanotubes has been reported in literature. On the contrary, no data about the activity of hybrid system **G-Cat** covalently bonded are reported.

G-Cat system was obtained by the incubation of catalase (1.0 mg/ml) with **RAPG** (Scheme 2.32). The interaction involves the formation of amide bond between the carboxyl groups present on the **G** surface and the free ammonium groups present on Lysine moieties, a peptide of **Cat**.

The **Cat** and **RAPG** were incubated at different weight ratio, to found the best interaction/binding conditions. **CG1**, **CG2**, **CG3** samples were prepared using 1:2, 1:1 and 2:1 **RAPG/Cat** (w/w) ratio respectively. Moreover, **RAPG** was treated with bovine serum albumin (BSA) (1 mg/mL), before the incubation with **Cat**. In addition, the behavior of **RAPG** saturated with BSA (**CG4** sample) has been evaluated. The obtained results are described in the Fig. 2.33.

The loading efficiency was estimated by the detection of the enzymatic activity of **Cat** present in the supernatant of the reaction mixtures, after 24 hours of incubation at room temperature. **CG1**, **CG2**, **CG3** showed a loading values of $38.4 \pm 0.75\%$, $46.0 \pm 0.56\%$, $99 \pm 0.36\%$ respectively, while sample **CG4** showed values less than 30%. These data suggest that the **Cat** keeps its activity only in **CG1** sample, while it results completely inactive in **CG2**, **CG3** and **CG4**. The residual activity of **CG1** is about $23.0 \pm 2.6\%$ and, at room temperature, it remains constant up to one month.



Scheme 2.32 Synthesis of hybrid system **CG** by click chemistry reaction.

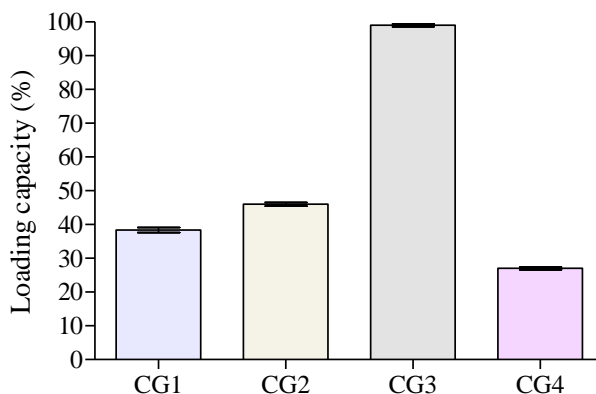


Figure 2.33 Loading capacity of catalase on modified graphene.

These results were also confirmed by Bradford assay (data not shown). Indeed the analysis of the amount of protein, present in the supernatant as well as in the precipitate, gives results in agreement with those obtained by enzymatic activity detection.

Hence, the best efficiency of loading was obtained in the sample characterized by the higher **Cat** concentration, **CG1**. This result suggests that the enzymatic loss activity is due to the interactions between **RAPG** and **Cat** (such as π - π stacking and crosslinking covalent bond by free amino group of protein), which impair the structure and therefore the catalase enzymatic activity. Therefore we supposed that at lower **G** concentration (**CG1**) an amount of **Cat** keeps its activity because it is not binded on **G** surfaces. This hypothesis was supported by FT-IR spectroscopy of protein structure (data not shown). The lower absorbance at 1652 cm^{-1} , observed in **CG1** sample suggests a net decrease of α -helix structures. This structural change is responsible of a double effects: *i*) a decrease of the protein catalytic activity respect to an equal amount of free protein; *ii*) an increase of the half life time of enzyme, at the same time.

In order to further understand the **G** influence on the catalase activity, free **Cat** has been incubated with fixed amounts of **CG1**, **CG2**, **CG3** and **CG4** for several days (Fig. 2.34). The free enzyme without **CG** complex shows a half-life of ~ 77 min and it is not changed in presence of **CG4** sample. On the contrary the half-life decreased remarkable by ~40 fold in 10 min in presence of **CG2** and **CG3**, while it increased by ~1.7 fold in presence of **CG1** sample.

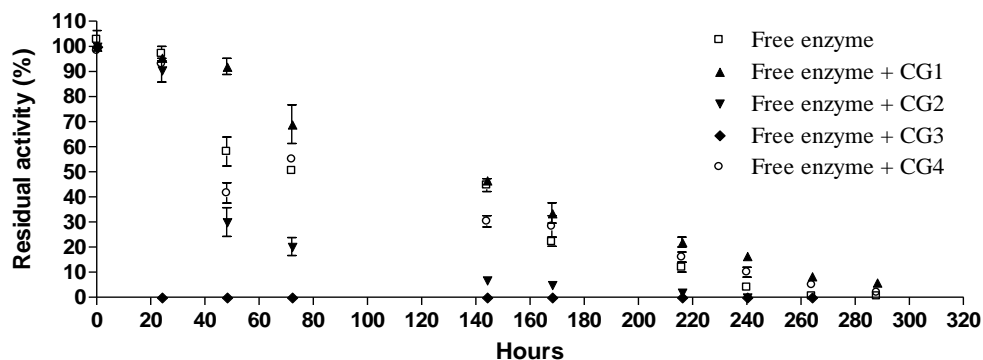


Figure 2.34 Effect of the drug delivery system on free enzyme activity after different intervals of time.

The ability of **G-Cat** complex to overcome cellular membrane of lymphocytes was investigated by preparing **CG1** complex labeled with fluorescein (FITC). The cellular uptake of **CG1-FITC** labeled was analyzed on lymphocytes after 2 hour of incubation. The test was carried out in presence of chlorpromazine, a well known inhibitor of clathrin-mediated endocytosis. The data showed that the cellular uptake was completely inhibited in presence of chlorpromazine alone, indeed it results in a complete lack of fluorescence in the cells, as expected. On the contrary, an increase of intracellular fluorescence in presence of **CG1** complex was detected. In particular an intracellular fluorescence up to ~1.7 fold at the maximum concentration was estimated (Fig. 2.35). These data suggest that the mechanism is almost completely clathrin-dependent.

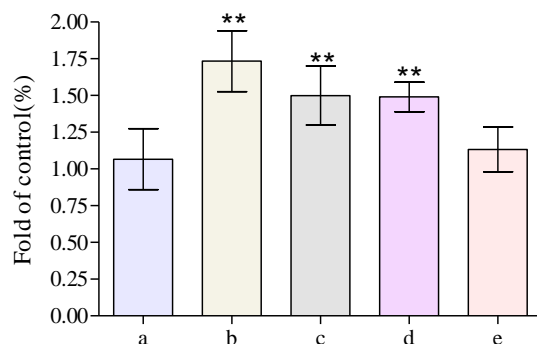


Figure 2.35 Increase of fluorescence in cells in the absence (a) or in the presence of 0.1 (b), 0.05 (c) and 0.025 (d) mg/ml of **CG1** FITC-labeled. Cells incubated in the presence of 0.1 mg/ml of **CG1** FITC-labeled and chlorpromazine. The asterisks indicated significant difference ($P < 0.05$) in function of control.

Finally the ability of **CG1** to protect lymphocytes from H_2O_2 injuries was tested (Fig. 2.36). Previously, the cells were incubated with **CG1** at three different concentrations (0.1 mg/mL, 0.05 mg/mL and 0.025 mg/mL) for 2 hours; then the cells were washed twice and finally they were exposed to the strong oxidant action of H_2O_2 for 2 hours. After the incubation time both the cell vitality, LDH release, caspase 3 activation and protein carbonyl groups increase were determined.

The incubation of lymphocytes for 2 h at $37^\circ C$ in the presence of $100 \mu M H_2O_2$ induced a decrease of cellular vitality down to 27%. The biological test indicated the **CG1** ability to protect the cellular damages from H_2O_2 at all tested concentration. The amount of surviving cells is almost completely superimposable to the one obtained with cells incubated in the absence of H_2O_2 .

The cytoprotective effects of **CG1** were also evaluated determining the release of LDH from lymphocytes, the activation of caspase 3, the increase of protein carbonyl groups and reactive oxygen species. LDH is a cytosolic enzyme commonly used to check cell viability due to its release outside the cells, after the membrane integrity loss. Protein carbonylation and caspase 3 activation are factors induced by oxidative stress conditions inside the cells.

The oxidative damage, induced by H_2O_2 , results in cellular membrane breakdown, LDH release, increase of reactive oxygen species, protein carbonylation and caspase 3 activation (up to ~4.0, 1.3, 1.25 and 1.35 fold with respect to control). The LDH release in presence of **CG1** is not observed, confirming its ability to protect the cells from oxidative damages. These results are also supported by the analysis of ROS with dichlorofluorescein, by the lack of caspase 3 activation and by the increase of protein carbonylation.

On the overall, the results highlight the potentiality of graphene platform to act as a drug delivery system for Catalase. It was demonstrated that the nanocarrier is able to enter the cells and to protect them from oxidative damages.

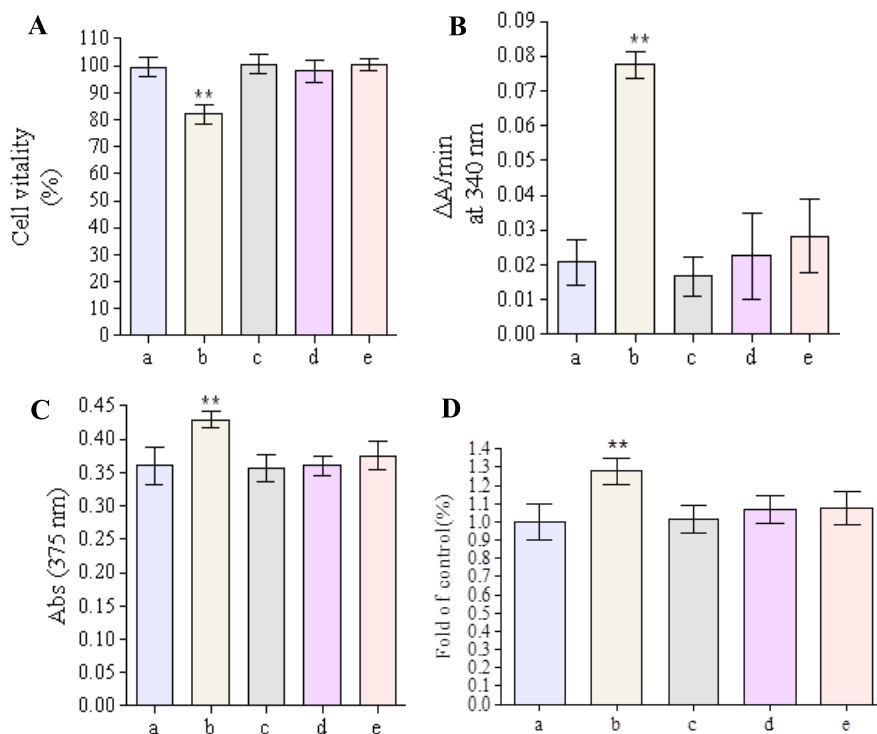


Figure 2.36 Cytoprotective activity of **CG1** on lymphocytes treated with hydrogen peroxide. Lymphocytes were first incubated for two hours in the absence (a and b) or in the presence 0.1 mg/ml (c), 0.05 mg/ml (d) or 0.025 mg/ml (e) of **CG1**. After centrifugation and washing the samples b-e have been resuspended in incubation buffer and treated with 100 μM of H_2O_2 . Detection of cell vitality with trypan blue (A), LDH (B), protein carbonylation (C) and caspase 3 (D). The asterisks indicated significant difference ($P < 0.05$) in function of control H_2O_2 .

2.6 Experimental section

Materials

Graphite (GF), solvents and other reagents were purchased from Sigma Aldrich. Merck Kieselgel 60F254 plates were used for TLC and Merck silica gel 60 (0.063–0.100 mm) for column flashchromatography. Lyophilized bovine liver catalase, hydrogen peroxide (30% solution) and all other chemicals used in this work were obtained from Sigma Chemical Company (St. Louis, MO).

Synthesis of azido-azalactone moiety (APDMA)

Synthesis of 4-(azidomethyl)benzoyl chloride

A solution of 4-bromomethyl benzoic acid (2.23 g, 13 mmol) and sodium azide (2.55 g, 39.2 mmol) in DMSO (10 mL) was stirred for 48h at 80 °C. After cooling to room temperature, 10 mL of deionized water and 20 mL of Et₂O were added. The organic phase was extracted with water and dried over MgSO₄; the solvent was removed under reduced pressure to obtain the pure 4-azomethyl benzoic acid (2.1 g, yield 95%). Thionyl chloride (1.2 mL) was added to 4-azomethyl benzoic acid (540 mg, 95.66 mmol) at 0°C; the reaction was left at room temperature for 4 h under stirred and then at 50°C for 12 h. The reaction mixture was dried under reduced pressure to obtain an oil that was used without purification.

Synthesis of 2-(4-azidomethyl)benzamido)-2-methylpropanoic acid

A solution of 4-(azidomethyl)benzoyl chloride (497 mg, 2.55 mmol) in dioxane (5 mL) was added dropwise to mixture of 2-amino-2-methylpropanoic acid (263.9 mg, 2.55 mmol) and 756.8 mg of Na₂CO₃ in 10mL of deionized water. The solution was stirred overnight at room temperature. The solvent was removed under reduced pressure and the residue was treated with chloroform. The white precipitate was removed and the organic solvent was dried under reduced

pressure to obtained 400 mg of 2-(4-azidomethyl)benzamido)-2-methylpropanoic acid. No sign of product decomposition is evident until the dry powder was heated to 80 °C. 2-(4-azidomethyl)benzamido)-2-methylpropanoic acid white solid, 58 % yield, mp 172- 175°C.

¹H NMR (500 MHz, CDCl₃) 1.77 (s, 6H), 4.49 (s, 2H), 6.74 (bs, 1H, NH), 7.38 (d, 2H, *J*=8.3 ESI-3 Hz), 7.79 (d, 2H, *J*=8.3 Hz), 7.95 (bs, 1H, OH).

¹³C NMR (125 MHz) 24.5, 24.9, 54.2, 57.1, 127.3, 127.7, 128.0, 128.5, 133.9, 139.4, 167.0, 177.9. MALDI-TOF (m/z): 263.3 [MH⁺] cld for C₁₂H₁₄N₄O₃ 262.1.

Synthesis of 2-(4-azidomethyl)phenyl)-4,4-dimethyloxazol-5(4H)one

To a solution of 2-(4-azidomethyl)benzamido)-2-methylpropanoic acid (145 mg, 0.55 mmol) in dry acetonitrile (1 mL), ethyl chloroformate (52 μL) was added under argon inlet. The reaction mixture was stirred for 30 min at room temperature; then the temperature was decreased at 5 °C and triethylamine (152 μL) was added. The reaction was stirred for 2h at room temperature and for an additional hour at 40°C. The formed precipitate was removed by filtration and the supernatant dried to a yellow oil under reduced pressure. The residue was extracted using hot hexane, the solutions were collected and dried under reduced pressure to obtain 110 mg of 2-(4-azidomethyl)phenyl)-4,4-dimethyloxazol-5(4H)one. No sign of product decomposition is evident until the dry powder was heated to 80 °C. 2-(4-azidomethyl)phenyl)-4,4-dimethyloxazol-5(4H)one, yellow oil, 76% yield.

¹H NMR (500 MHz, CDCl₃) 1.23 (s, 6H), 4.41 (s, 2H), 7.42 (d, 2H, *J*= 6.3 Hz), 7.99 (d, 2H, *J*= 6.3 Hz).

¹³C NMR (125 MHz) 24.7, 24.8, 54.2, 65.9, 125.9, 128.2, 128.3, 128.4, 140.2, 159.0, 181.0. MALDITOF (m/z): 245.2 [MH⁺] cld for C₁₂H₁₂N₄O₂ 244.1.

Synthesis of Azido- Silibinin (Sil N₃)

Silibinin (247 mg, 0.51 mmol) and boron trifluoride diethyl etherate (100 μ L) were added in sequence to a solution of 4-(azidomethyl)benzoyl chloride. 4-(azidomethyl)benzoyl chloride (100 mg, 0.51 mmol) in acetonitrile/dichloromethane (10 mL, 1:1) The reaction mixture was left at 0°C for 2h; then, a second portion (100 μ L) of boron trifluoride diethyl etherate was added and the solution was stirred overnight at room temperature. A saturated solution of NaHCO₃ was added to the reaction and it was left to stir for 20 min. The product was extracted with EtOAc (3 x 10 mL) and the organic phases were collected and dried over anhydrous sodium sulphate and concentrated under reduced pressure. The crude was purified by chromatography column (chloroform/acetone/formic acid: 9.5-0.1-0.5) to obtain 157 mg of **Sil-N₃** (3) as white solid (48% yield). *(3-(4-hydroxy-3-methoxyphenyl)-6-(3,5,7-trihydroxy-4-oxochroman-2-yl)-2,3dihydrobenzo[b][1,4]dioxin-2-yl)methyl 4-(azidomethyl)benzoate.*

¹H NMR (500 MHz, CDCl₃): δ ppm 3.90 (s, 3H, OCH₃), 4.03 (dd, 2H, J₁ = 10.0 Hz and J₂ = 4.5 Hz, -CH₂O), 4.21-4.30 (m, 2H, CH₂N₃), 4.43 (ddd, J₁ = 10 Hz, J₂ = 1.5 Hz and J₃ = 0.9 Hz, 1H, CH-10), 4.53 (dd, J₁ = 12 Hz and J₂ = 5 Hz, 1H, CH-3), 4.90 (dd, 1H, J₁ = 10.0 Hz and J₂ = 1.5 Hz, CH-11), 5.00 (d, 1H, J = 12 Hz, CH-2), 5.78 (bs, 1H, OH), 5.97 (dd, 1H, J₁ = 1.8 Hz and J₂ = 1.7 Hz, CH-8), 6.05 (dd, 1H, J₁ = 1.8 Hz and J₂ = 1.04 Hz, CH-6), 6.86-6.98 (m, 3H), 7.03-7.13 (m, 2H, CH-15/16), 7.19 (d, J = 11.0 Hz, 2H), 8.02 (d, J = 11.0 Hz, 2H), 8.24 (s, 1H, D₂O exchangeable, OH), 11.19 (s, 1H, D₂O exchangeable, OH).
¹³C NMR (125 MHz): δ ppm 14.1, 22.7, 29.3, 30.9, 31.2, 32.0, 56.1, 62.3, 72.3, 75.7, 76.3, 82.9, 95.9, 97.1, 100.8, 109.2, 114.9, 116.4, 116.6, 117.4, 117.5, 120.8, 121.1, 127.2, 143.7, 146.7, 147.1, 160.3, 162.2, 163.1, 163.8, 165.6, 195.7.
MALDI-TOF (m/z): 664.3 [MNa⁺]; cld for C₃₃H₂₇N₃O₁₁: 641.164.

Preparation of graphene base materials: GO, G-Red

Briefly, natural graphite (2 g) was added to sulfuric acid (350 mL) cooled at 0 °C and the mixture was vigorously stirred to avoid agglomeration. When the graphite was well dispersed, sodium nitrate (1g) and potassium permanganate (8 g) were, very slowly and contemporaneously, added to the reaction mixture. The temperature was then raised up to 40 °C and the mixture was stirred for 1 h. Thereafter, deionized water (250 mL) was slowly added into the solution, determining an immediate increase of temperature up to 70 °C. The temperature was raised up to 98°C and the reaction stirred for 30 min. Finally, 52 mL of H₂O₂ 30% were poured into the reaction mixture, resulting in the formation of bright yellow suspension. The graphite oxide was separated by vacuum filtration and washed with diluted HCl (4%) and water to reach a neutral pH. The product was dried to obtain a brown powder (1.8 g). Exfoliation of graphite oxide was carried out by ultra sonication (40% W, 8h) of the aqueous suspension graphite oxide (500 mg of graphite oxide in 35 mL of deionized water). The obtained homogeneous dark brown dispersion was diluted with deionized water and ultracentrifugated at 10000 rpm for 12 min; then, the residue was eliminated and the supernatant contains the graphene oxide sheets (**GO**) were recovered. **GO** powders were obtained by freeze-drying of supernatant (300 mg). From TGA analysis under N₂ atmosphere weight loss of 51% , due the decomposition of the surface groups heated up to 600 °C, was estimated. The reduced graphite oxide (**G-Red**) was obtained by reduction of the **GO** with hydrazine, according to literature procedure. The **GO** powders (100 mg) were dispersed in deionized water at concentration of 3 mg/mL and sonicated for 3 h; 33µL of 98% Hydrazine was added and the reaction mixture was stirred at 80°C overnight. The reduced graphene (**G-Red**) precipitate was filtered under vacuum on Millipore membrane of 0.1 µm and washed with deionized water. The residue was dried under vacuum at 50 °C to give 70 mg of **G-Red**. From TGA

analysis under N₂ atmosphere a weight loss of 15 % due the decomposition of the surface groups heated up to 600 °C was estimated.

Preparation of Reactive Azalactone Graphene Platform (RAPG)

Synthesis of alkyne-terminated graphene (G-Alk)

The aryldiazonium ion solution was prepared following the method described below. Sodium nitrite (329 mg, 4.76 mmol) was slowly added, at 0 °C under stirring, to a solution of p-(2-propylnyloxy)-benzamine (638 mg, 4.34 mmol) in HCl 37% (82.21 mL). Then, 2.17 mL of HCl 20% were dropwise added and the reaction was stirred at 0 °C for 45 min.

G-Red, (171 mg) dispersed in deionized water (100 mL) was sonicated at room temperature for 1 h to obtain a homogeneous black suspension. The diazonium salt solution was added to the black suspension and the reaction mixture was sonicated at 0 °C for 6 h. The reaction mixture was diluted with deionized water and centrifuged at 6000 rpm for 20 min. The precipitate was repeatedly washed with a solution of deionized water and methanol (1:1), the supernatant was discharged after centrifugation at 6000 rpm for 20 min and the residue was dried at 60 °C to give 56 mg of **G-Alk**.

From TGA analysis, under N₂ atmosphere, the amount of alkyne moiety grafted on the graphene surface was estimated to be ~11 wt % corresponding to ~0.8 mmol /g.

Synthesis of reactive azlactone graphene platform (RAGP)

Alkyne-terminated graphene (**G-Alk**) (20 mg) in 10 mL of dry DMF were sonicated at room temperature for 30 min to obtain a homogeneous black suspension. Azido-azlactone (**APDMA**) (20 mg, 0.081 mmol), sodium ascorbate (8.5 mg, 0.043 mmol) and copper sulphate (3.65 mg, 0.022 mmol) were added at room temperature under argon inlet. Then the temperature was increased up to 80 °C and the reaction was stirred at 80 °C for 48 h under argon inlet. The reaction mixture was diluted with deionized water and centrifuged at 6000 rpm for 20 min. The supernatant was

discharged and the residue was repeatedly washed with a solution of deionized water/methanol (1:1) and again centrifuged at 6000 rpm for 20 min. The precipitate was dried at 60 °C to give 23 mg of **RAGP**. From TGA analysis under N₂ atmosphere the amount of linked oxazolone moiety was estimated to be ~8.3 wt % corresponding to ~0.3 mmol /g.

Reaction of RAGP with aminopropyltriethoxysilane (APTS)

APTS (0.028 mL, 0.122 mmol) was added to a solution of **RAGP** (30 mg, 0.122 mmol), in toluene (2 mL). The reaction was allowed to stir at room temperature overnight. The solvent was removed under reduced pressure to obtain coupling product (58 mg). *N*-(2-(3-(triethoxysilyl)propylcarbamoyl)propan-2-yl)4(azidomethyl)benzamide, white solid, 100% yield, mp 160-162 °C.

¹H NMR (300 MHz, CDCl₃) 0.62 (t, 2H, *J*=9.0 Hz), 1.19 (t, 9H, *J*= 9.1Hz), 1.62 (q, 2H, *J*=9.0 Hz), 1.67 (s, 6H), 3.31 (m, 2H), 3.80 (q, 6H, *J*=9.1 Hz) 6.58 (bs, 1H, *NH*), 7.30 (bs, 1H, *NH*), 7.38 (d, 2H, *J*= 6.1 Hz), 7.81 (d, 2H, *J*= 6.1 Hz).

¹³C NMR (125 MHz) 7.5, 18.3, 22.7, 25.0, 42.1, 54.2, 54.4, 58.4, 58.5, 127.5, 128.2, 134.8, 138.8, 166.1, 174.6. MALDITOF (m/z): 488.3 [MNa⁺] cld for C₂₁H₃₅N₅O₅Si 465.2.

Preparation of Functionalized G Platforms

Reaction of RAGP with aminopropyltriethoxysilane (APTS)

RAGP (25 mg) in 5 mL of DMF was sonicated at room temperature for 10 min to obtain a homogeneous black suspension. **APTS** (20 μL, 0.04 mmol) was added and the reaction mixture was stirred at room temperature overnight. The reaction mixture was diluted with deionized water and centrifuged at 10000 rpm for 10 min and the supernatant was discharged. The precipitate was repeatedly washed with a solution of deionized water and methanol (1:1), centrifuged at 10000 rpm for 15 min and the supernatants were discharged. The residue was dried at 60 °C to give 20 mg of **GF-APTS**. From TGA analysis, under N₂ atmosphere, the

amount of linked **APTS** was estimated to be ~22,8 wt % corresponding to ~ 1.0 mmol /g

Reaction of RAGP with oxidized glutathione (GSSG)

GSSG (12.5 mg, 0.02 mmol) was added to a homogeneous black suspension of RAGP (25 mg) in DMF (5 mL) and the reaction was stirred at room temperature for 72 h. The reaction mixture was diluted with deionized water and centrifuged at 10000 rpm for 10 min. The precipitate was repeatedly washed with a solution of deionized water and methanol (1:1), centrifuged at 10000 rpm for 15 min and the supernatants were discharged. The residue was dried at 60 °C to give 24 mg of **GF-GSSG**. From TGA analysis, under N₂ atmosphere, the amount of linked **GSSG** was estimated to be ~ 22.7 wt corresponding to ~0.3 mmol /g.

Reaction of Sil-N₃ with G-Alk

Alkyne-terminated graphene (**G-Alk**) (140 mg corresponding to 0.112 mmol of alkyne) was sonicated at room temperature for 1h in 10 mL of THF/H₂O (1:1) to obtain a homogeneous black suspension. **Sil-N₃** (71 mg, 0.112 mmol), sodium ascorbate (40 mg, 0.2 mmol) and copper sulfate (16 mg, 0.1 mmol) were added at room temperature under argon inlet. The reaction was stirred for 48h under argon inlet; then, the reaction mixture was filtered under vacuum (Millipore 0.22 mm). The residue was repeatedly washed in sequence with water/ethanol (1:1) each time being sonicated and separated from the supernatant by centrifugation. The solid was then dried under vacuum at 50 °C to constant weight of 190 mg. The graphene functionalization degree (loading %) was estimated in terms of weight loss by TGA upon heating a solid reaction product, from 100 °C to 700 °C under N₂ atmosphere.

Biological evaluation: Graphene Silibinin Conjugated (G-Sil)

Cell cultures

Human mesenchymal stem cells (MSCs) and human osteosarcoma cell line (MG63 cell line), purchased from Lonza (Italy) were used for the biological study. In detail, MSCs were cultured in DMEM Glutamax medium (Gibco) containing 10% of FBS and 1% penicillin–streptomycin (100 U/ml–100 µg/mL). MG63 were cultured in Dulbecco Modified Eagle’s (DMEM)/F12 Medium (Gibco), containing penicillin/streptomycin (100 U/ml–100 µg/ml) supplemented with 10% fetal bovine serum (FBS). The cell cultures were kept at 37 °C in an atmosphere of 5% CO₂. For the experiments, cells were plated in 96 and 24 well plates at 5 x 10³ cells/cm². 24 h after the cell seeding the materials were added to the cells and left in culture for 48 h. Three different concentrations of **G-Alk** (10, 100 and 1000 µg/ml) and two different concentrations of free **Sil** and **G-Sil** (50 and 100 µg/ml; referred to the **Sil** content), were tested with both the cell cultures in order to evaluate the cytotoxicity and the biological effects. The cells cultured without materials were used as control group (cells alone).

Cell viability assay

MTT reagent [3-(4,5-dimethylthiazol-2-yl)-2,5-diphenyltetrazolium bromide] (Sigma) was prepared at 5 mg/mL in 1x PBS. Cells were incubated with the MTT reagent 1:10 for 2 h at 37 °C. Medium was discarded and cells incubated with 200 µl of dimethyl sulfoxide for 15 min. In this assay, the metabolically active cells react with the tetrazolium salt in the MTT reagent to produce a formazan dye that can be observed at kmax of 570 nm, (113) using a Multiskan FC Microplate Photometer (Thermo Scientific). The absorbance value is directly proportional to the number of metabolically active cells. Mean values of absorbance were determined. All experiments were carried out in triplicate.

Apoptosis evaluation

After 48 h MG63 and MSCs cells were tested with Annexin V kit (Molecular Probes) in order to discriminate non-apoptotic cells to cells in early apoptosis. (114) Briefly, the cells were washed in PBS 1x for 5 min and incubated for 15 min at room temperature with Alexa Fluor^R 488 annexin V diluted in 1X annexin-binding buffer. Then, the cells were washed, stained with 300 nM DAPI (Invitrogen) in PBS 1x for 5 min and visualized with an Inverted Ti-E fluorescence microscope (Nikon). MG63 and MSCs treated with 50 μ M of doxorubicin for 48 h were used as positive control.

Preparation of Graphene Catalase Bio conjugate (G-Cat)

Determination of catalase activity

Catalase activity was measured following the decreased in absorbance at 240 nm due to H₂O₂ decomposition rate. Fixed amount (10 μ L of 1.0 mg/mL) of either free catalase or **CG1** was mixed with 1.0 mL of H₂O₂ solution 10 mM in 50 mM phosphate saline buffer pH 7.2 (PBS) and its absorbance monitored up to 5 min.

Loading of Catalase on RAPG

RAGP at different concentration (0.5, 1.0 and 2.0 mg/mL) was dispersed by sonication for 1 minute, mixed with catalase (1.0 mg/mL) and left at 4°C for 24 hours to obtain **GG1**, **GG2**, **GG3** respectively. We have also tested the efficiency of loading after saturation of **RAPG** (1.0 mg/ml) with 1.0 mg/ml of bovine serum albumin (BSA). In order to measure the loading efficiency of catalase on **RAPG**, aliquots of the solutions were withdrawn at fixed interval of time (0, 1, 3, 6, 9 and 24 h) and the catalase activity was tested together with total protein amount according to Bradford method.

Effects of GG1 on free enzyme activity

Catalase (0.5 mg/ml final concentration) were incubated with **CG1** (0.5 mg/ml final concentration) at room temperature up to 320 h. At fixed interval of time, after

centrifugation, aliquot of the samples were withdraw and tested for enzymatic activity.

Cellular uptake of CG1

In order to analyzed the uptake of **CG1**, we labelled the enzyme with fluorescein isothiocyanate. Briefly, **Cat** (2.0 mg/mL final concentration) was dissolved in carbonate buffer (100 mM) pH 9.0 and mixed with of fluorescein isothiocyanate (1.5 mg/mL final concentration) for 2 h at room temperature. **Cat** labelled with the fluorescence dye was separated from unreacted fluorescein isothiocyanate using a PD-10 desalting column equilibrated in PBS (pH 7.2). Fluorescein isothiocyanate-catalase (1.0 mg/mL) were mixed with **RAPG** (0.5 mg/ml) and, after 1 hour of incubation, **G** materials were separated from the aqueous medium by centrifugation at 8000 rpm for 5 min. The amount of fluorescein isothiocyanate-catalase loaded on **RAPG** was checked analyzing the amount of protein in supernatant by Bradford assay, before and after incubation with the **G** material. The cellular uptake of fluorescein catalase-**G** loaded on, was analyzed utilizing lymphocyte as cell model. The isolated cells (1×10^5 /ml) were mixed for 4 hours with fluorescein **G-Cat** at a final concentration of 0.5 mg/ml. Then, the cells were separated by centrifugation (4000 rpm for 10 min) and washed three times with incubation buffer. After the final wash the cell were resuspended in PBS (pH 7.2) and lysed by sonication. The fluorescence of the solution have been recorded with a spectrophotometer. To verify the mechanism of cellular uptake the experiment has been performed in the absence or in the presence of chlorpromazine, a well known inhibitor of cellular uptake mediated by clathrin system.

Data analysis

Protein spectra were smoothed by Loess algorithm and the deconvolved spectra fitted with Gaussian band profiles. Initial values for the peak heights and widths were estimated from the deconvolved spectra. For the final fits, the positions,

heights, and widths of all bands were varied simultaneously. The curve fitting procedure was calculated on Seasolve PeakFit v4.12 software.

Lymphocyte isolation

Lymphocytes were isolated from whole blood obtained by venipuncture from healthy male volunteers and collected in heparinized tubes. All donors' volunteers provided written informed consent to participate in the study and had been informed of all risks, discomforts and benefits involved in the study, in accordance with the Declaration of Helsinki, for research protocols approved by the institutional review boards of the National Institutes of Health (NIH). All subjects provided medical histories, using a standardized questionnaire and not received anti-inflammatory medication or nutritional supplements. Blood samples were diluted with an equal volume of balanced salt solution, layered over Histopaque-1077 (Sigma-Aldrich) in centrifuge tubes, and centrifuged at 400 x g for 30-40 min at 25°C. The peripheral blood mononuclear cell (PBMC) lymphocyte layer was removed with a pipette and washed by centrifugation. The PBMCs are passed through a Percoll gradient according to Repnik et al. (2003) to enrich the fraction in lymphocytes. The former (viability > 90%) were counted on a haemocytometer and suspended in RPMI 1640 media supplemented with 10% fetal calf serum, 2 mM glutamine, 100 units/ml penicillin G e streptomycin. The cell concentration was adjusted to 1×10^5 cells/ml.^(115, 116)

Cytotoxicity assays

The isolated cells were incubated (1×10^5 /ml) in medium with or without 0.1, 0.05 and 0.025 mg/ml of **GG1** for 2 h. After the incubation, the cells were centrifuged and, after, elimination of supernatant and resuspension in incubation medium, exposed to hydrogen peroxide (100 μ M) for 2 hours. In all experiments parallel controls were performed without hydrogen peroxide.^(117, 118) The cell viability, was evaluated established trypan blue staining. Briefly, an aliquot of the cell suspension

was diluted 1:1 (v:v) with 0.4% trypan blue and the cells were counted using a haemocytometer. Results are expressed as the percentage of live or dead cells (ratio of unstained or stained cells to the total number of cells, respectively). Cytotoxicity was also measured by lactate dehydrogenase (LDH) release from damaged cells into culture medium, and expressed as a percentage of total cellular activity. The activity of LDH in the medium was determined using a commercially available kit from BioSystems S.A. Extracts don't show to interfere with the determination of LDH at the concentration utilized in the experiments. For the evaluation of caspase activity, lymphocytes were collected and washed three times (after treatments) with phosphate saline buffer (PBS) and re-suspended in Hepes-buffer (100 mM HEPES pH 7.5, 20% glycerol, 5 mM DTT and 0.5 mM EDTA). The lysates were clarified by centrifugation at 20000 x g for 10 min at 4°C and supernatants were passed through Microcon YM 30 (Nominal Molecular Weight Limit 30,000 Da) to obtain a partial purification of caspase 3. The activity of caspase 3 was monitored spectrophotometrically for 1 h at 37°C spectrophotometrically following the release of p-nitroaniline (Pna) at 405 nm from enzyme-specific colorimetric substrates (Ac-DEVD-pNA). Caspase 3 was expressed in arbitrary units as a function of untreated sample. Protein carbonylation has been analysed by UV-vis spectroscopy at 375 nm, following derivatization with 2,4-dinitrophenylhydrazine according to Levine et al. (1990).⁽¹¹⁹⁾

Characterization techniques

¹H-NMR spectra were obtained with a Varian 500 MHz spectrometer. Raman scattering measurements were carried out by means of a Horiba XploRA Micro-Raman spectrometer using the 638 nm laser line, focused on the sample's surface through the 50x objective of a microscope. The backscattered radiation was collected by the same microscope optics and dispersed by a monochromator

equipped with a 1800 line/mm holographic grating. The dispersed radiation was detected by means of a Peltier-cooled charged-coupled device (CCD) sensor. In order to avoid drug damaging, the laser power on the sample surface was kept as low as possible (≈ 1 mW), while the integration and the accumulation times were fixed at 80 s. Infrared transmission measurements were carried out in the 400–4000 cm^{-1} range using a FT-IR Spectrum 100 Perkin-Elmer spectrophotometer with a resolution of 2 cm^{-1} . Shape and size distribution were evaluated by scanning transmission electron microscopy (STEM). Analyses were carried out with the Zeiss-Gemini 2 scanning electron microscope operating at 30 kV and at a working distance of 4 mm. Samples were dispersed in isopropanol (0.5 mg/mL) and sonicated using the Sonics VCX 130 ultrasonic sonicator. Then, a drop of each suspension was dried, at room temperature for 3 h, on a 400 mesh holey-carbon coated copper grid. TGA was performed by means of Perkin-Elmer Pyris TGA7, in the temperature range 50–800 °C. About 5 mg of each sample was, firstly, placed in an platinum pan and kept at 30 °C under a 60 mL/min N_2 flow until balance stabilization and subsequently heated with a scan rate of 10 °C/min under the same N_2 flux. Balance sensitivity was 0.1 μg . A baseline recorded in the same measurement conditions with empty platinum pan was subtracted from each thermogram before data analysis. MALDI-TOF mass spectra were collected by a Voyager DE (PerSeptive Biosystem) using a delay extraction procedure (25 kV applied after 2600 ns with a potential gradient of 454 V mm^{-1} and a wire voltage of 25 V) and detecting the ions in linear mode.^(120, 121)

In order to avoid fragmentation of the sample, the excitation laser irradiance was maintained slightly above the threshold. Each spectrum was an average of 32 laser shots. The MALDI-TOF investigations were performed by loading on the plate 0.4 mmol matrix trans-2-[3-(4-tert-butylphenyl)-2-methyl-2-propenylidene]-malonitrile (DCTB) and 0.005 mmol of sample, using DMF as solvent.

Both 5,10-di(p-dodecanoxyphenyl)-15,20-di(p-hydroxyphenyl)porphyrin ($C_{68}H_{78}N_4O_4$, 1014 Da), tetrakis(p-dodecanoxyphenyl)porphyrin ($C_{92}H_{126}N_4O_4$, 1350 Da) and a PEG sample of known structure were used as external standards for m/z calibration.⁽¹²²⁻¹²⁴⁾ The MALDI-TOF mass spectra were elaborated with Grams software (ver. 3.04), from Perseptive Biosystems.

UV-vis have been carried out in quartz cuvettes (Hellma) with optical path of 1 cm at 298 K, using a Hewlett-Packard mod. 8453 diode array spectrophotometer. **G-Sil** was analysed in superpure water (Galenica Senese) at 0.5 mg/mL after sonication (1 h) and settling (15 min). For this amount, [**Sil**] onto **G-Sil** was 400 μ M (as obtained from TGA). UV-vis spectra of **G-Sil** were registered in the same condition after longer settling time (1 and 4 h, respectively). Scattering function was subtracted (OriginPro 8.5). For comparison UV-vis spectra of **Sil** and **G-Alk**, dissolved in 7% v/v DMF/H₂O, were acquired. UV-vis of **Sil** was normalized for [**Sil**] amount onto **G-Sil**.

Statistical analysis

Data are presented as means \pm standard deviation (S.D.). Data were analysed by one-way analysis of variance (ANOVA). The significance of the difference from the respective controls for each experimental test condition was assayed by using Tukey's for each paired experiment. A $p < 0.05$ was regarded as indicating a significant difference.

Chapter 3:

*From graphite to functionalized graphene by
oxazolone chemistry*

In this chapter, an innovative method for a direct exfoliation and functionalization of graphite to **G** is described. The procedure has been tested by employing two differently substituted oxazolones. A high degree of functionalization (2.1–4.6% @700 °C) was obtained for both substrates under mild conditions (70–120 °C). Successively, the resulting graphene materials were employed for the preparation of **G**/gold nanocomposites (**G/Au**). The properties of **G/Au** nanocomposites as SERS materials have been investigated by using Rhodamine 6G (R6G) as a test probe.

3.1 Functionalized G nanosheets by a top-down approach from graphite using oxazolone chemistry

As reported in chapter 1, various different types of graphene can be identified depending on the number of layers, layer dimension and amount of oxygen present in the carbon structure. Although its excellent properties endow **G** great potential, in many practical applications ⁽¹²⁵⁻¹²⁹⁾, its inertness nature, zero band gap and non-dispersibility in solvents weaken its competitive strength in the synthesis of composites, semiconductors, sensors, etc.⁽¹³⁰⁻¹³²⁾ Moreover, the difficulty to produce high-quality **G** on a large scale limited its practical use. Chemical functionalization of **G** on substrates is a topic of paramount importance, because it allows for the fine-tuning of the material's chemical and physical properties.

More strategy has been focused about the functionalization of **GO** especially *via* esterification/amidation reactions at the carboxylic groups and the coupling of diazonium salts to the sp² network. Respect to graphite or **G**, **GO** shows more imperfections on the carbon basal plane, which cause a reduction of its electrical and thermal conductivity capacities. For these reasons its employments in electronics field is limited.

Other important approaches to fabricate functionalized **G** materials are 1,3-dipolar cycloaddition (1,3-DC) ⁽¹⁹⁾, the Bingel reaction ⁽¹³³⁾, the Diels–Alder reaction (DA) ^(21, 134) and others ^(22, 135), which directly take place on the **G** surface. These synthetic strategies are not devoid of drawbacks due to the low intrinsic reactivity of **G**, which is lower than that of other carbon nanoforms, such as fullerene and carbon nanotubes, principally because of the absence of tension in the **G** basal planes.

DA is the most investigated cycloaddition process, since Haddon and co-workers have suggested that **G** can be used as either a diene or a dienophile for DA reversible reactions.⁽²⁴⁾

In 2013, for the first time, Seo et al. proposed the DA protocol to access functionalized **G** nanosheets, in a top-down approach, starting directly from graphite.⁽¹³⁶⁾ This approach allowed to obtain **G** suitably functionalized, without destroying its conjugated basal planes, without affecting the relevant chemical-physical properties.

Recently, modifications of graphite/graphene by DA reactions have been carried out using solvent-free processes. Exfoliated and functionalized **G** sheets have been obtained by Jeong-Min Seo et al. *via* DA reaction, using the graphite as diene and *maleic anhydride* (MA) or *maleimide* (MI) as dienophile. The reaction is performed at high temperature (160–220 °C), in solvent free conditions.⁽¹³⁷⁾

Highly conductive **G** was produced by Zhen Ji et al. by retro-DA reaction.⁽¹³⁸⁾ *Tetracyanoethylene* (TCNE) moieties were covalently bonded onto the **G** sheets surface *via* DA. The insertion of TCNE moieties among **G** layers induce the mechanical exfoliation of graphite in dispersible **G** adducts (GA). By retro-DA the π -system of graphene has been restored and the resultant **G** adducts exhibits a conductivity as high as 1035 S m⁻¹, comparable to that of pristine **G**.

To date, only the 1,3-DC reactions of azomethine ylides have been thoroughly investigated for the chemical manipulation of **G**.^(19, 139) No examples of

graphite/graphene functionalization by mesoionic compounds, such as 1,3-dipoles, have been reported in literature.

Oxazolones (azalactones) are versatile precursors in organic synthesis for the preparation of structurally complex amino acids and highly substituted heterocycles.^(140,141) They serve as mesoionic azomethine ylides in 1,3-dipolar cycloadditions for the construction of pyrroles, pyrrolynes, imidazoles and imidazolines. The tautomerization of the *oxazol-5-(4H)-one* into its reactive mesoionic form (münchnone, Mu) can be promoted by heating, Lewis acid (LA) conditions and basic catalyst.^(94, 142) Their reactivity as dipoles was exploited to functionalize carbon nanomaterials such as fullerene and multiwalled carbon nanotubes (MWCNT) (Fig. 3.1).

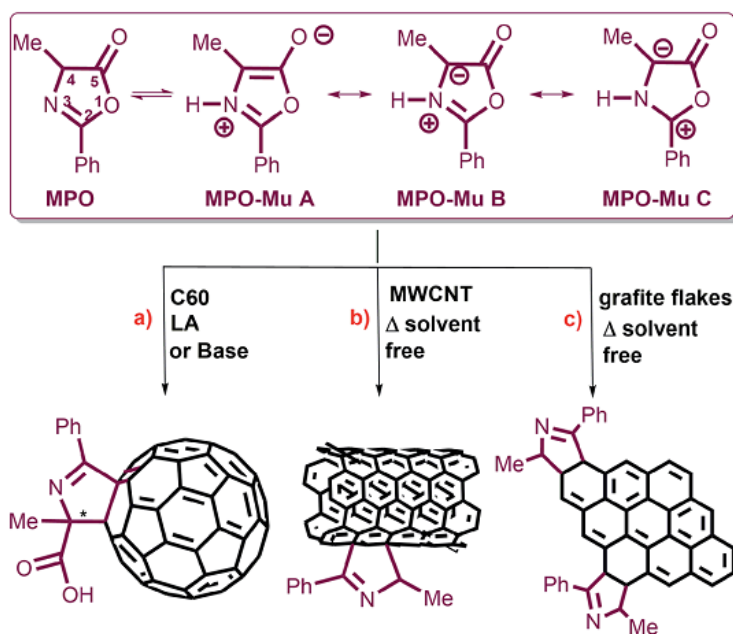


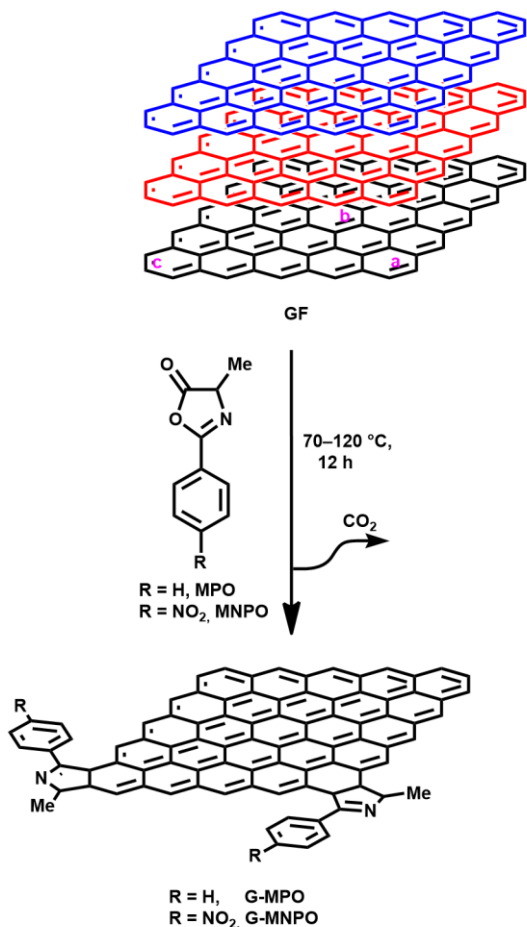
Figure 3.1 Models of the molecular structures of 4-methyl-2-phenyl oxazol-5-(4H)-one (**MPO**) and its Mu tautomers, and their 1,3-DC reactions. (a) Schematic representation of the enantioselective cycloaddition of **MPO-Mu** onto C60 under organocatalysis or LA metal catalysis. (b) 1,3-DC reaction between **MPO-Mu** and **MWCNTs**. (c) 1,3-DC of **MPO-Mu** with graphite flakes (**GFs**) reported herein.

In the course of my PhD research activity the interest was focused on the direct delamination and functionalization of graphite into **G** by exploiting the reactivity of oxazolones in solvent free conditions. *4-methyl-2-phenyl oxazolone* (**MPO**) and *4-methyl-2-p-nitrophenyl oxazolone* (**MNPO**) were selected as oxazolone substrates for their capability to react in solid/solid conditions.⁽¹³⁹⁾ Under heating, the isomerisation of oxazolones to münchnones triggers the cycloaddition process with the successive domino reactions of decarboxylation and final dehydration of 1:1 adduct. All 1,3-DC reactions were performed in a closed system using a glass ampoule at mild temperature between 70°-120° C. To improve the efficiency of the process, the graphite flakes (**GF**), **MPO** or **MNPO** were previously triturated in a mortar to obtain a fine powder. Moreover, the reactions were carried out under different experimental conditions by varying graphite/dipole weight ratio (w/w), reaction temperature and sonication time (Table 3.1, Scheme 3.2). In the first experiment the reaction was performed at 80 °C with a 1:10 **GF/MPO** weight ratio for 12 h (Table 3.1, entry 1). In order to completely remove the unreacted dipole, the reaction mixture was washed in sequence with different solvents, each time being sonicated and separated from the supernatant by centrifugation. The solid was then dried to constant weight under vacuum at 50 °C and appropriately characterized.

The **G** functionalization degree (loading %) was estimated in terms of weight loss by TGA upon heating a solid reaction product, from 100 °C to 700 °C under N₂ atmosphere (Fig. 3.3).

The TGA curve of **G-MPO1**, compared to graphite one, showed a substantial thermal stability at low temperatures, while it exhibited a relevant weight loss between 300–700 °C. It was estimated a loadings of 2.3% and 3.5% at 500 °C and 700 °C, respectively (Fig. 3.3). This is an unambiguous evidence of covalent grafting of organic groups on **G** sheets, ruling out the presence of adsorbed organic

compounds (the TGA thermogram of a physical mixture GF/MPO showed a large weight loss in the range 200–300 °C, data not shown).



Scheme 3.2 Schematic representation of the solvent-free 1,3-DC reaction of **MPO** and **MNPO** on graphite.

Entry	Experimental conditions	Sample	C 1s	N 1s	O 1s
1	GF/MPO = 1/10, 80 °C, 12 h	G-MPO1	95.01	0.55	4.44
2	GF/MPO = 1/10, 6 h))) ^a 70 °C; 120 °C, 12 h	G-MPO2	95.08	0.26	4.66
3	GF/MNPO = 1/2, 6 h))) 70 °C; 120 °C, 12 h	G-MNPO1	82.92	1.61	15.47
4	GF/MNPO = 1/10, 6 h))) 70 °C; 120 °C, 12 h	G-MNPO2	85.11	1.75	13.15
5		GF	88.38	0.00	11.62

^a))) = sonication.

Table 3.1 Experimental conditions used in the synthesis of **G-MPO** and **G-MNPO**, with C, N, and O contents (%) obtained from XPS analysis.

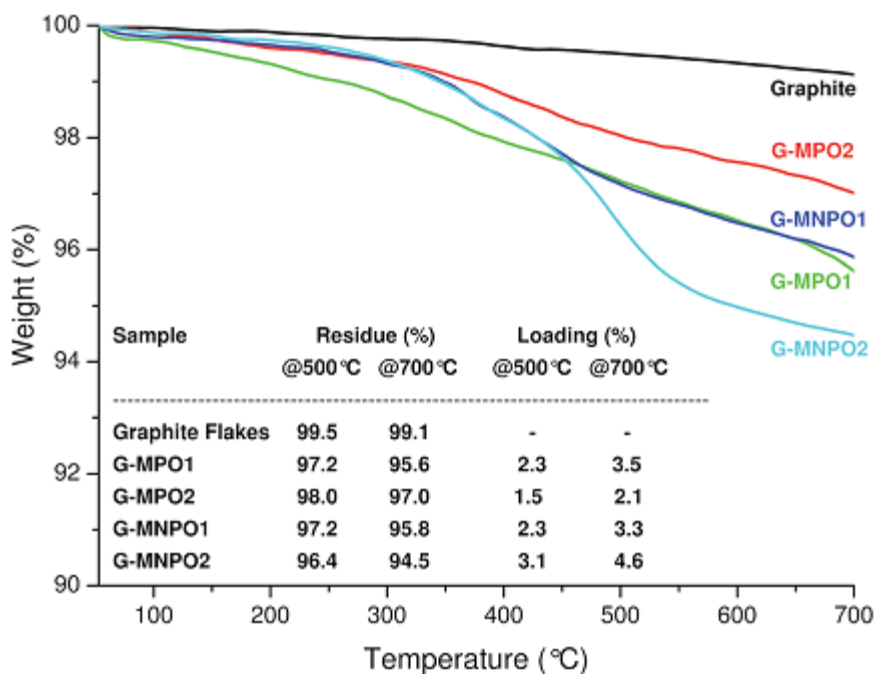


Figure 3.3 TGA profiles of *GFs*, *G-MPO1*, *G-MPO2*, *G-MNPO1*, and *G-MNPO2*, under a N_2 atmosphere. The inserted table reports the values, at 500 °C and 700 °C, of weight residue (%) and loading (%).

Moreover, the absence of adsorbed organic material was confirmed by the disappearance of characteristic azlactone absorption at 1818 cm^{-1} in the FT-IR spectrum (Fig. 3.4).

It can be supposed that the combination of increasing temperature and sonication treatment could promote the intercalation of oxazolones into graphite, expanding the graphite basal spacing and opening avenues for the penetration of dipoles into the graphite crystals and consequently improvement the exfoliation degree of graphite. Therefore, in order to improve the efficiency of the 1,3-DC process the reaction mixture was subjected to sonication at 70 °C for 6 hours and then heated at 120 °C for 12 hours (Table 3.1, entries 2–4).

Unfortunately the TGA profiles of *G-MPO2*, *G-MNPO1*, and *G-MNPO2* revealed no significant improvement in the efficiency of 1,3-DC respect to *G-MPO1*,

nevertheless the loading values were good for all experiments (Fig. 3.3). The efficiency of the 1,3-DC reaction was maintained in the case of oxazolone **MNPO**, despite its higher melting point with respect to **MPO**. The 1,3-DC reaction of **MNPO** with graphite (Table 3.1, entry 4) showed a good efficiency (4.5% @ 700 °C, see table 3.1). The loading was well preserved when lowering the graphite/dipole weight ratio from 1:10 to 1:2 (3.3% @ 700 C, see table 3.1).

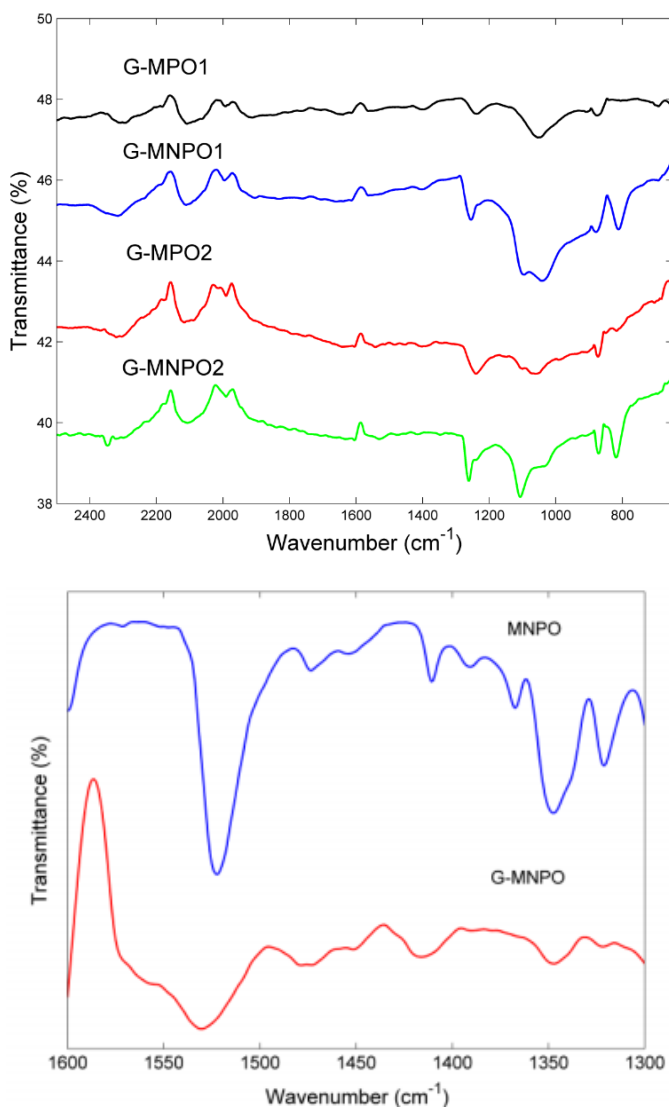


Figure 3.4 FT-IR spectra of functionalized graphene materials (up), and the comparison between the FT-IR spectra of **MNPO** and **G-MNPO** from 1300 cm⁻¹ to 1600 cm⁻¹ (down).

Information about the types of functional groups grafted on the **G** surfaces was obtained by XPS analysis.

As expected the XPS results (Fig. 3.5, Table 3.2) showed that the **G** nanomaterials have different C, O and N contents on the basis of the amount of oxazolone used (**G-MPO** series vs. **G-MNPO** series, Table 3.1). In particular, **G-MNPO2** exhibits relatively high amounts of N (1.75%) and O (13.15%) as well as a lower C content (85.11%) with respect to graphite (0.00% N, 11.62% O, and 88.38% C) and the **G-MPO2** sample (0.26% N, 4.66% O, and 95.08% C). Moreover in sample **G-MNPO2** a change in the N 1s high resolution profiles due to the additional presence of the nitro group is observed (Fig. 3.5 a). In particular the N 1s profile is dominated by two peaks at about 400 and 407 eV, representative of the formation of the C=N functionality and of aromatic nitro groups, respectively. At variance, the **G-MPO2** sample is characterized by only the contribution at 400 eV. Thus, going from the sample **G-MPO2** to **G-MNPO2**, the expected increase in the contribution centered at about 407 eV is observed (from 0% up to 28%). This behavior is accompanied by the decrease of the C=N percentage (from 100% down to 72%).

The C1s bands were deconvoluted using six contributions: a main contribution at 284.5 eV attributed to C=C/C-C in the aromatic ring and four other contributions at higher binding energies corresponding to carbon atoms bonded to nitrogen (C-N) and oxygen in different surface functionalities (C-OH, C-O, C=O) centred at 285.2, 286.3, 288.7, and 288.9 eV, respectively (Fig. 5.4, Table 2.4). The contribution at about 291.0 eV refers to $\pi-\pi^*$ bonds. The **G-MPO2** and **G-MNPO2** samples showed no significant differences in terms of carbon-oxidized phases while, as expected, the C-N bonds content increases in the **G-MNPO2** sample (see Table 3.2).

The structures of **G-MPO** and **G-MNPO** were further investigated by micro-Raman spectroscopy. In Fig. 3.6 and 3.7 are reported the Raman spectra, acquired

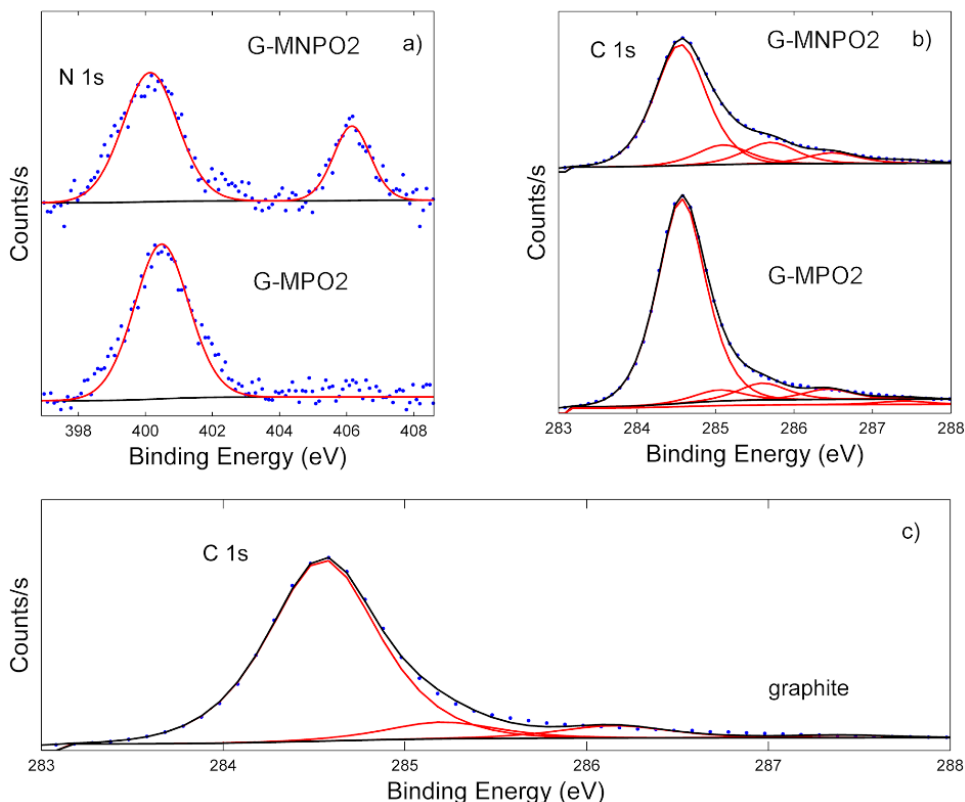


Figure 3.5 N 1s and C 1s photoelectron deconvoluted lineshapes of graphite *G-MPO2* and *G-MNPO2*.

C 1s	C=C	C-H	C-N	C-O	C=O	$\pi-\pi$
Graphite	85.0	7.7	0.0	5.9	1.3	0.1
<i>G-MPO2</i>	83.4	4.6	6.8	4.3	0.8	0.1
<i>G-MNPO2</i>	68.5	11.0	12.2	6.0	2.0	0.3

Table 3.2 C 1s XPS deconvolution fitting results for graphite, *G-MPO2* and *G-MNPO2*. All values are in percent.

on several different locations, of the micrometric-sized granular powders to take into account of the possible lack of spatial homogeneity.

The **G**-based materials showed, in the 1100–3000 cm^{-1} spectral region, four main peaks: structural imperfections due to the nanographene platform functionalization, D band (1350 cm^{-1}); the primary in plane vibrational G mode (at about 1580 cm^{-1}); the D+D' band, which appears in the 2400–2450 cm^{-1} region of the spectra; and the

second-order overtone 2D mode (at about 2690 cm^{-1}). The I_D/I_G peak intensities ratio is used to estimate the level of disorder in the **G** derivatives. In all samples, these values are below 0.5, with no appreciable variation between them, indicating that the functionalization has a limited effect on the pristine graphite structure. The same behavior occurs for the G mode peak position, which is located at about 1580 cm^{-1} for all the samples, with no shift. Nevertheless, it is evident that the D and G band intensity ratio changes moving from one sample point to another. Moreover, the D' contribution, centred at around 1620 cm^{-1} , is evident in some portion of the sample.

Finally, information about the number of **G** layers can be derived from the I_G/I_{2D} peak intensities ratio, as well as their positions and shapes. In fact, because of added forces from the interactions between the **G** layers, the Raman spectrum will change from that of single-layer **G**, namely a splitting of the 2D peak, into an increasing number of modes that can combine to give a wider, downshifted, peak. Thus, the 2D band splitting of the **G-MPO2** sample indicates the presence of several (at least four) **G** layers. At variance, the **G-MNPO2** sample shows a single, almost symmetric 2D peak located at 2710 cm^{-1} , with a full width half maximum of about 65 cm^{-1} , i.e., in an intermediate position with respect to the $2D_1$ (2683 cm^{-1}) and $2D_2$ (2718 cm^{-1}) peak positions of the bulk graphite. Interestingly, the **G-MNPO2** sample presents an I_G/I_{2D} ratio value of 0.2, significantly lower than 1.4 and 1.3, values found for the graphite and **G-MPO2** respectively. The I_G/I_{2D} ratio value, the barely visible occurrence of the D band and the almost symmetric 2D band lineshape point out that the **G-MNPO2** sample exfoliation process is rather effective for obtaining single-layer-like functionalized **G**. In the other sample, Raman data suggested a simple delamination into multiple (albeit few) layers of functionalized **G** nanosheets. All these pieces of evidence are in good agreement with literature data.⁽¹⁴³⁻¹⁴⁵⁾

The spectrum reported in Fig 3.7a is characterized by G and 2D bands with comparable intensity and by the presence of the D' band (around 1615 cm⁻¹).

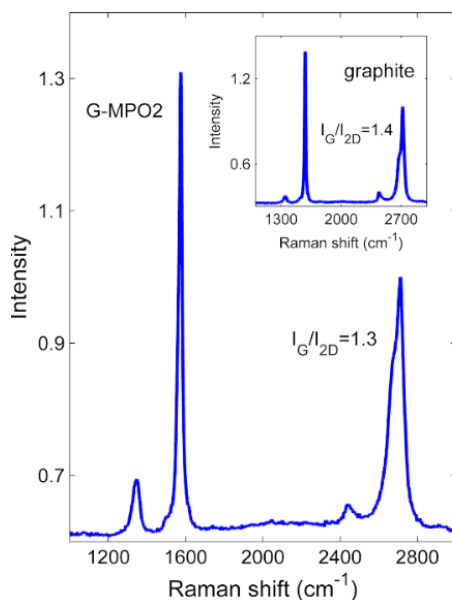


Figure 3.6 Raman spectra of **G-MPO2** and graphite (inset).

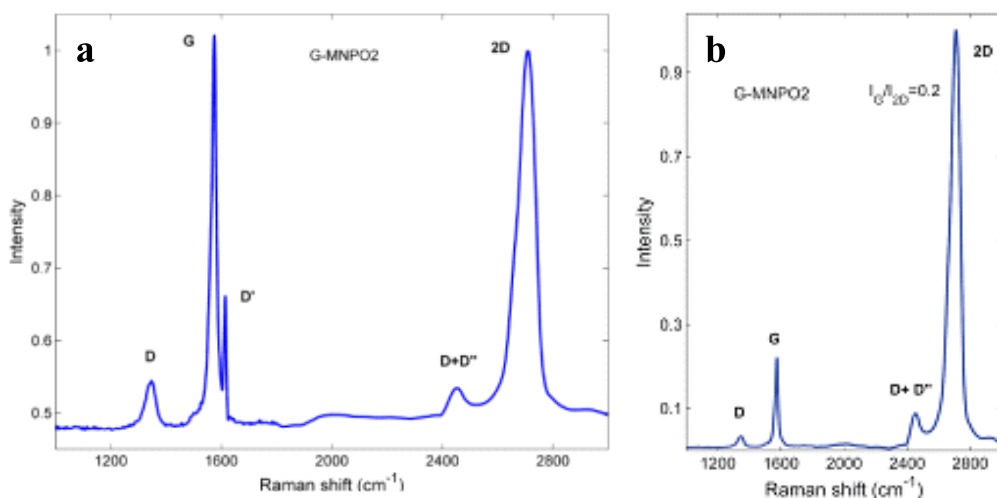


Figure 3.7 Raman characteristic spectra of **G-MNPO2**. The D/G intensity ratio is very different and the D' contribution is not evident in some portion of the sample.

Direct evidence of the effective occurrence of the exfoliation process was also given by STEM analysis. All the samples showed homogeneously distributed exfoliated **G** layers. All samples showed variable-dimension transparent sheets stacked onto each other, pointing out the efficient functionalization and exfoliation of pristine graphite (whose morphology is shown in Fig. 3.8 a) into a few layers of **G** nanosheets (Fig. 3.8 b). Moreover, folded sheets were also observed (Fig. 3.8 c). A thicknesses of about 2–3 nm was estimated in the **G-MNPO** samples.

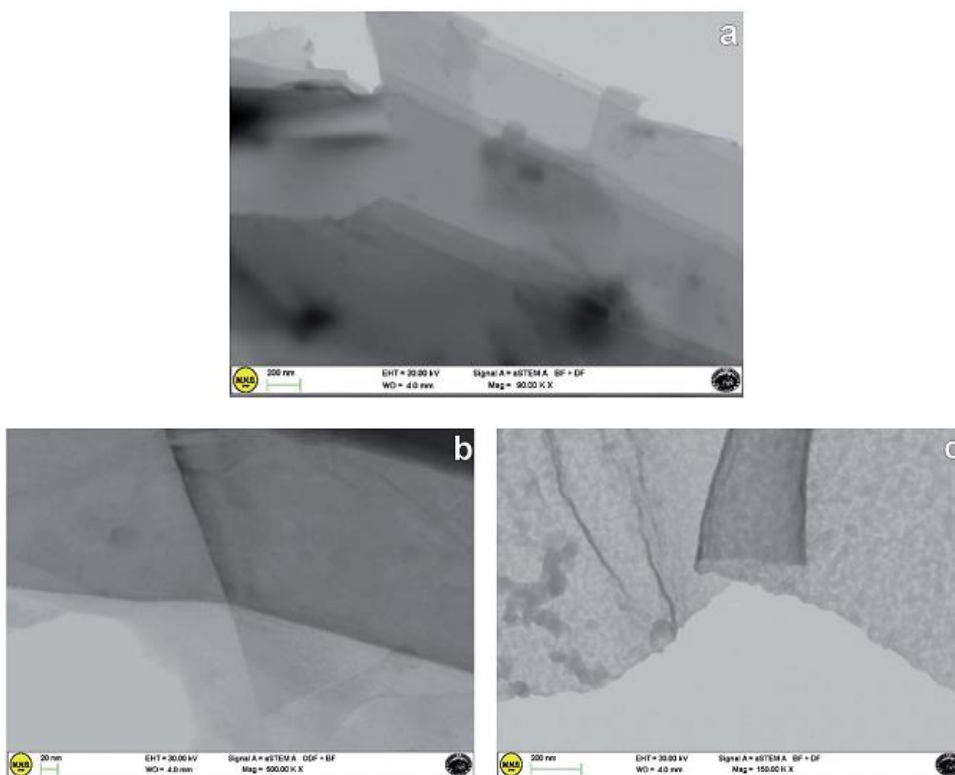


Figure 3.8 STEM images of (a) **graphite**, (b) few layers of **graphene nanosheets** in the **G-MPO2** sample and (c) **folded graphene sheet** in the **G-MNPO**.

3.2 Computational studies

To further investigate the 1,3-DC reaction of **Mu** to **GFs**, and to rationalize and shed light on the obtained results, the reactivity of MPO-Mu, chosen as a model, by first-principles calculations within the DFT framework. **G** sheets were simulated by C₇₀H₂₂ polybenzenoid hydrocarbons consisting of 25 fused benzene rings (five in a row and five in a line), terminated by hydrogen atoms, presenting zigzag shape edges (Fig. 3.2).

The computational studies were performed in collaboration with Prof. Antonino Rescifina, from the Catania University.

In this section a brief summary of results is reported.

All transition state (TS-a-c), intermediate (I-a-c), and product structures (**G-MPO-a,c**) have been reported in Fig. 3.9 and 3.10, whereas their energetic and charge parameters have been summarized in Table 3.3, Fig. 3.11.

From a mechanistic standpoint, the formation of I-a1, b, c2 may be rationalised by two possible approaches, a stepwise mechanism and a concerted one. In our case, for pathways *a* and *b* we were able to localize only the concerted process, whereas for pathway *c* only the stepwise one was successful. In principle, alternative mechanisms might also be envisaged for both cases, however all attempts to locate stationary points for reaction channels other than those reported herein were unsuccessful.

From Table 3.3 it is clear that pathway *b* is highly endergonic and the formation of I-b can be ruled out; this behaviour was expected because the reaction on the interior double bond disrupts the aromaticity of four benzene rings. Pathway *a* is the only one that furnishes a 1,3-DC product energetically more stable than the reagents and has an activation energy (TS-a1) of 2.87 kcal mol⁻¹ higher than that of TS-c1 for pathway *c* (Fig. 3.11). On the contrary pathway *c* is slightly endergonic, with an activation energy for the second step (TS-c2) of 3.41 kcal mol⁻¹ higher than that of

TS-a1. So, pathways *a* and *c* turn out to be competitive, with the second one highly reversible (DG inverse barriers of 7.41 and 15.15 kcal mol⁻¹ for TSc1 and TS-c2, respectively, compared to 27.89 kcal mol⁻¹ for TS-a1). The natural population analysis ^(146, 147) allows us to evaluate the charge transferred between the two reactants at the TSs geometry. The charge transfer in terms of the residual charge on the **MPO-Mu**, for all the optimized TSs involved in the 1,3-DC process, is shown in Table 3.4. In all cases positive values are indicative of an electron flow from the HOMO of MPO-Mu to the LUMO of the **GFs**, in close agreement with Sustmann's type I dipolar cycloaddition rule (i.e. HOMO(dipole)–LUMO(dipolarophile) controlled reactions).⁽¹⁴⁸⁾ Moreover this charge is more pronounced for the stepwise TS-c1 and reaches its maximum for the zwitterionic intermediate I-c1, according to a nucleophilic addition of the negatively charged C4 carbon atom of MPO-Mu to one of the carbon atoms belonging to the *c* double bond. In the I-c1 structure the positive charge is almost all concentrated on the C93 atom (+0.72 e), whereas the negative one is principally spread over the C83 and C89 atoms.

The zwitterionic intermediate I-c1 is stabilized by secondary orbital interactions. In fact, from the results of the second order perturbation theory (SOPT) analysis of the Fock matrix in NBO basis, according to the definition of delocalization energy given by Weinhold ^(149, 150) and reported in Table 3.4. It emerges that I-c1 is stabilized by a series of delocalizations, of which the main are the π/π^* (0.47 kcal mol⁻¹) of the C45–C85 bonding orbital with the antibonding orbital of the C104–C107 double bond and the two π/π^* (0.52 and 0.53 kcal mol⁻¹), due to the C83–C89 double bond with the antibonding orbitals of the C93–C100 and C97–O99 (Fig. 3.4).

Considering that the nitrogen inversion is a fast event, at these operating temperatures, we have taken it in account and reported here only the most stable

conformer. Finally, we considered the decarboxylative process that generates the products **GMPO-a** and **c**. The activation free energies, corresponding to the concerted loss of carbon dioxide from cycloadducts I-a1 and I-c2, of 20.74 and 22.76 kcal mol⁻¹, respectively, suggest that this is the slow step of the reaction. The irreversible character of decarboxylation and the stability of the obtained products agree with the high grade of functionalization found experimentally.

The tautomerization of **MPO** to **MPO-Mu** is not yet fully clarified. An attempt to determine the free energy of activation for this process, based on a 1,2-hydrogen shift mechanism, gave a result of 57.93 kcal mol⁻¹. Thus, the formation of the mesoionic compound must proceed through a more complex process.

Experimental evidence indicates that several 1,3-DC reactions of **MPO** with activated alkenes proceed at RT. Our results showed that 1,3-DC of **MPO** performed in solid–solid conditions was more effective than classical reactions in molecular solvents. The functionalization degrees detected in the reaction performed in toluene at reflux for 12 h using a 1:10 **GF/MPO** weight ratio were 0.40% @500 °C and 0.93% @700 °C.

Considering that no literature data are available, we have undertaken a comprehensive study to fully explain our results.

Considering that the mesoionic **MPO-Mu** differs in energy by +19.35 kcal mol⁻¹ from the starting **MPO** tautomer, the outcome of the whole reaction is that in the case of pathway *c* the process is endergonic by 1.66 kcal mol⁻¹, whereas for pathway *a* it is exergonic by 13.68 kcal mol⁻¹. So it is probable that the most expensive step could consist of the tautomerization reaction ($DG\# > 25$ kcal mol⁻¹), justifying the temperature of almost 70 °C that it takes for the reaction to occur.

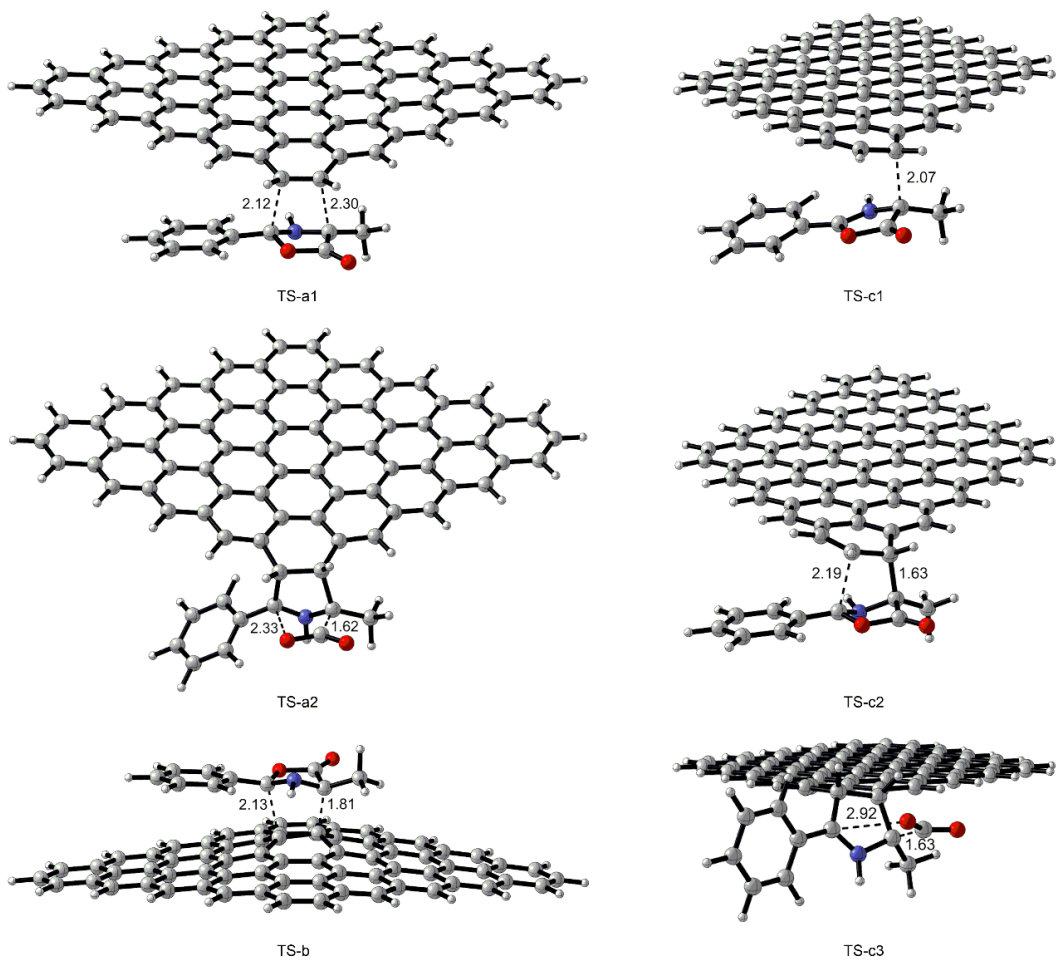


Figure 3.9 Transition state optimized structures for the 1,3-DC reaction of **MPO-Mu** with **GFs**. Distances are in Å. Carried out with CYLview.⁽¹⁵¹⁾

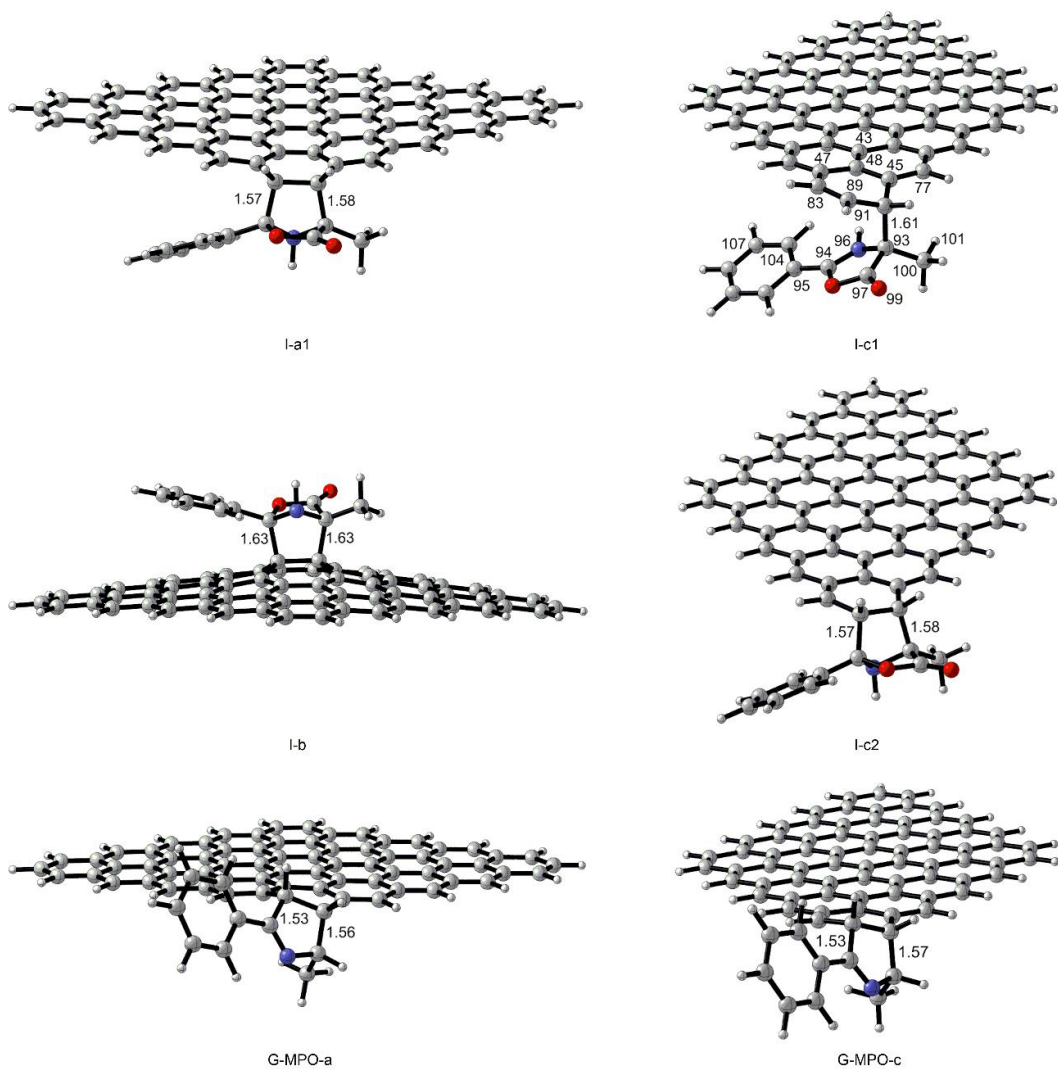


Figure 3.10 Intermediate and product optimized structures for the 1,3-DC reaction of **MPO-Mu** with **GFs**. Distances are in Å. Carried out with CYLview.^[151]

Structure	Direct ΔH^a	Inverse ΔH^b	Direct ΔG^a	Inverse ΔG^b	NPA qCT (e)
TS-a1	-0.03	29.38	15.71	27.89	+0.18
TS-a2	21.74	29.78	20.74	41.60	-
TS-b	18.75	4.71	37.63	4.60	+0.32
TS-c1	-2.71	7.45	12.84	7.41	+0.47
TS-c2	12.51	15.00	19.12	15.15	+0.31
TS-c3	23.67	32.34	26.73	44.42	-
I-a1	-29.41	-	-12.18	-	-
I-b	14.04	-	33.04	-	-
I-c1	-10.16	-	5.43	-	+0.75
I-c2	-12.65	-	3.97	-	-
G-MPO-a	-37.45	-	-33.03	-	-
G-MPO-c	-21.32	-	-17.69	-	-

Table 3.3 I (U)M06-2X direct and inverse relative enthalpies (ΔH) (kcal mol⁻¹) and relative free energies (ΔG) (kcal mol⁻¹), and charge transfer (au) in terms of the residual charge of the **MPO-Mu** fragment in the transition state.

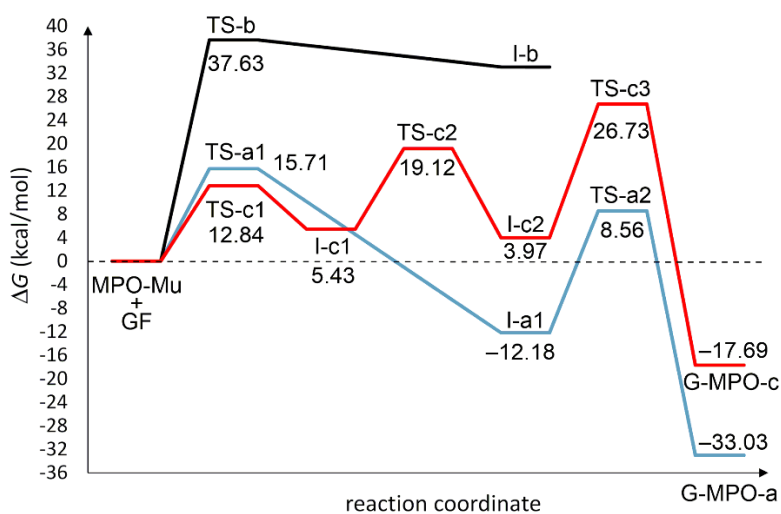


Figure 3.11 Free energy profiles for the a–c pathways involved in the 1,3-DC reaction of **MPO-Mu** with the 5 x 5 GF model. All values are relative to **MPO-Mu + GF**.

Bonds	Transition	Energy (kcal mol ⁻¹)
C45-C47/C100-H101	$\pi \rightarrow \sigma^*$	0.18
C45-C85/C104-C107	$\pi \rightarrow \pi^*$	0.47
C83-C89/C93-C100	$\pi \rightarrow \sigma^*$	0.34
C83-C89/C94-C95	$\pi \rightarrow \pi^*$	0.52
C83-C89/C97-O99	$\pi \rightarrow \pi^*$	0.53
C89-H91/C97-O99	$\sigma \rightarrow \pi^*$	0.25
C97-O99/C83-C89	$\pi \rightarrow \pi^*$	0.16
C100-C101/C45-C77	$\sigma \rightarrow \pi^*$	0.14
C104-C107/C47-C85	$\pi \rightarrow \pi^*$	0.12
N96/C43-C48	$n \rightarrow \pi^*$	0.32
N96/C47-C85	$n \rightarrow \pi^*$	0.14
N96/C45-C77	$n \rightarrow \pi^*$	0.13
N96/C47-C85	$n \rightarrow \pi^*$	0.07

Table 3.4 Secondary orbital interactions and delocalization energies for I-c1, as derived by the SOPT analysis.

3.3 Graphene/Gold Nanocomposites for SERS applications

In recent years the **G** has been proposed as new material for surface-enhanced Raman scattering (SERS) applications. In particular, it has been able to overcome the problems about the separation distance between the localized surface plasmons (LSPs). A drawback, exhibited by other materials, which commonly causes a decrease of sensitivity of hybrid-system.⁽¹⁵²⁾ **G** layers have a large surface area, reduced thickness and high flexibility, allowing an important interaction between the surface plasmons. In addition π electrons, of which **G** surface is rich, showed a high affinity with probe molecules. The combination of these two surface effects determines an excellent optical transmission of graphene in SERS applications. Therefore, **G** was proposed to prepare nanocomposites, characterized by a selective

and specific action, to be employed in labeled tumor cell detection ⁽⁷²⁾, biosensing applications ⁽⁶⁷⁾, molecular selectivity ⁽¹⁵³⁾ etc. The combination of Au NPs with **G** sheets resulted in a positive synergistic effects, mainly due to the Au/**G** chemical interaction and to the Au surface plasmonic effects, which gives to **G** unique electronic, optical, and chemical properties.⁽¹⁵⁴⁾

As a part of an ongoing program aimed at the functionalization of carbon nanomaterials for biomedical applications we investigated the ability of **G-MNPO** to act as SERS substrate.

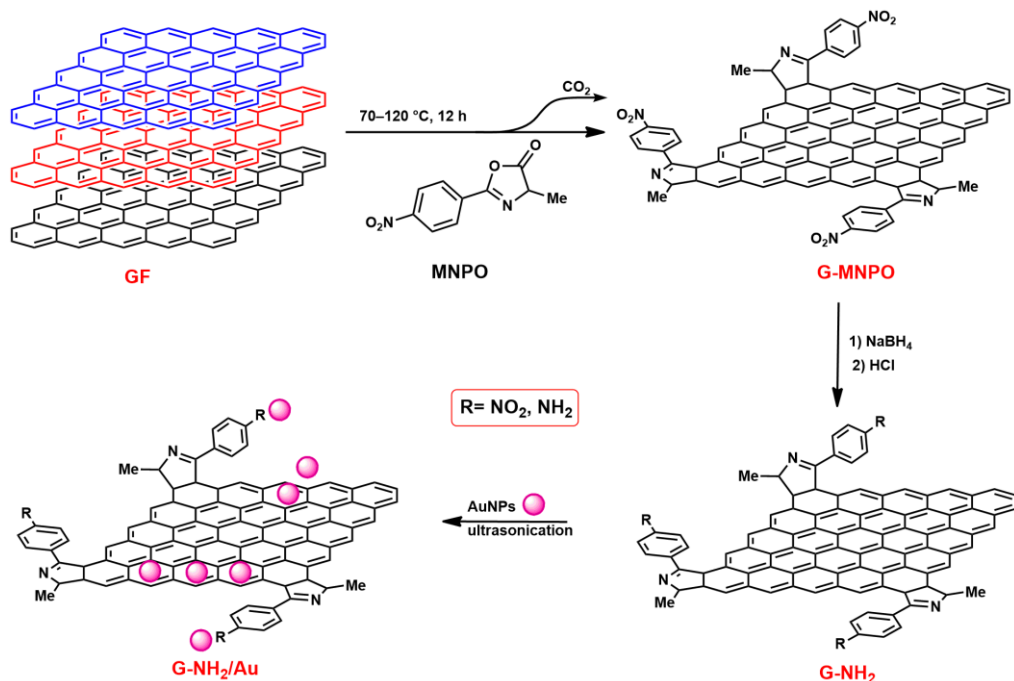
In our experiments **G-MNPO** was prepared according to the synthetic method previously reported and using in the cycloaddition reaction a molar ratio of 1:7 (**GF/MNPO**). The selected **G** substrate have a large surface area in a multilayer arrangement, an high degree of functionalization and the NO₂ groups that can be useful to bind the Au NPs. Moreover, to improve the insertion of Au NPs on **G** surface, some amine functionalities were introduced by reduction of **G-MNPO** with NaBH₄. The reduction of nitro-groups of **G-MNPO**, to amine groups gave the **G-NH₂** platform (Scheme 3.12).

Au NPs were prepared by pulsed laser ablation in liquids (PLAL) technique.

The opportunities offered by this approach are noteworthy: the production of NPs may occur in a variety of solvents, no surfactant is needed to stabilize the colloid, the NPs can be extremely pure and, finally, fine-tuning of the process allows the production of NPs which can differ in size and properties.⁽¹⁵⁵⁾ The 532 nm second harmonic emission wavelength of a Nd:YAG laser, operating at a repetition rate of 10 Hz (pulse length:5ns), was used to prepare the Au water colloids.. The ablation process was carried out using a laser fluence of 1.5Jcm², 20 mm of water above the target and an ablation time of 20 min.

Finally **G-NH₂/Au** sample was prepared by ultrasonication, mixing dispersion of **G-NH₂** with Au nano-colloids, for 1h (Scheme 3.12). In order to, completely

remove the unreacted Au NPs, **G-NH₂/Au** was filtered and repeatedly washed with water. Then the solid was dried to constant weight under vacuum at 60°C.



Scheme 3.12 Schematic representation of **G-NH₂** and **G-NH₂/Au** preparation.

Thermogravimetry analysis (TGA) of both **G-NH₂** and **G-NH₂/Au** shows a high thermal stability and no significant weight loss under 600°C, indicating the complete absence of labile oxygen-containing functional groups (Fig. 3.13). The profile of **G-NH₂** shows the decomposition between 750 °C and 900 °C, with a complete decomposition of carbon at temperatures higher than 900°C. In contrast, the **G-NH₂/Au** nanohybrid shows a lower decomposition temperature between 600 °C and 800 °C. A fully carbon decomposition of **G-NH₂/Au** can be marked at 800 °C. The residual mass of about 8.5% indicates loading of Au NPs in the **G-NH₂/Au** nanohybrid. A lower thermal decomposition of **G-NH₂/Au** compared to **G-NH₂** is due to presence of Au NPs that increase the interlayer spacing and porosity of the hybrid **G-NH₂/Au**.

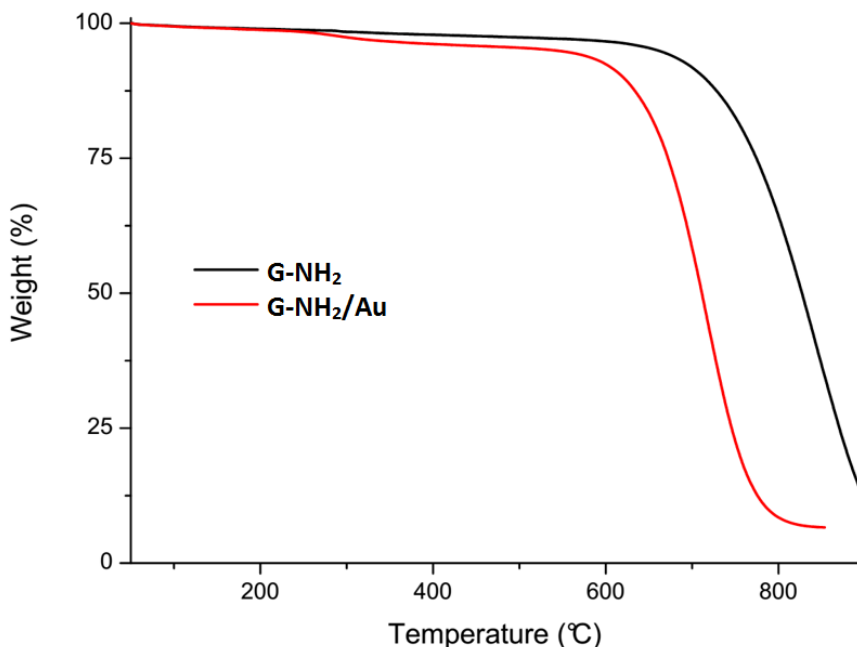


Figure 3.13 TGA profiles of **G-NH₂** (black line) and **G-NH₂/Au** (red line) under air atmosphere.

Some detailed information about the investigated systems (mainly about the chemical interaction between the graphene and Au NPs) were obtained by XPS analysis. In Fig 3.14 are shown the wide scan spectra of **G-NH₂** and **G-NH₂/Au** samples while, in the inset the Au 4f profile is shown. This profile is characterized by a well separated spin-orbit components ($\Delta=3.7\text{eV}$) where the Au 4f peak is centred at the binding energy of 84.0 eV), characteristic of the metal Au species. The chemical composition of the surface layer (5–10 nm) of all the samples was determined by XPS wide scan and high resolution line shapes. The C, O and Au species were observed in the surface layer and their percentage (calculated using the XPS area and atomic sensitivity factors), were given as relative atomic percentages (see Table 3.5).

The N 1s high resolution profile of **G-NH₂** (Fig. 3.15) showed the presence of two peaks at 400 eV attributed to N=C and NH₃⁺-C and 407 eV due to NO₂. The lower

contribute of the peak at 407 eV in **G-NH₂** sample, compared with the **G-MNPO** one (20.05 % vs 41.18%, see Fig. 3.15 and Table 3.6), indicates a good reduction of aromatic nitro groups into corresponding amino groups.

The decrease of the oxygen content after reduction reaction (19% vs 7.4%, see Fig. 3.14 and Table 3.5) further confirms the changes observed by N1s profile.

The C1s profiles of **G-MNPO**, **G-NH₂** and **G-NH₂/Au** have been deconvoluted considering six spectral components: a main contribution at 284.5 eV attributed to C=C/C-C in the aromatic ring, and four other contributions, at higher binding energies, corresponding to carbon atoms bonded to nitrogen (C-N) and oxygen (C-OH, C-O, C=O) centred at 285.2, 286.3, 288.7 and 288.9 eV, respectively. The contribution at a about 291.0 eV refers to π - π^* bonds (Fig. 3.16).

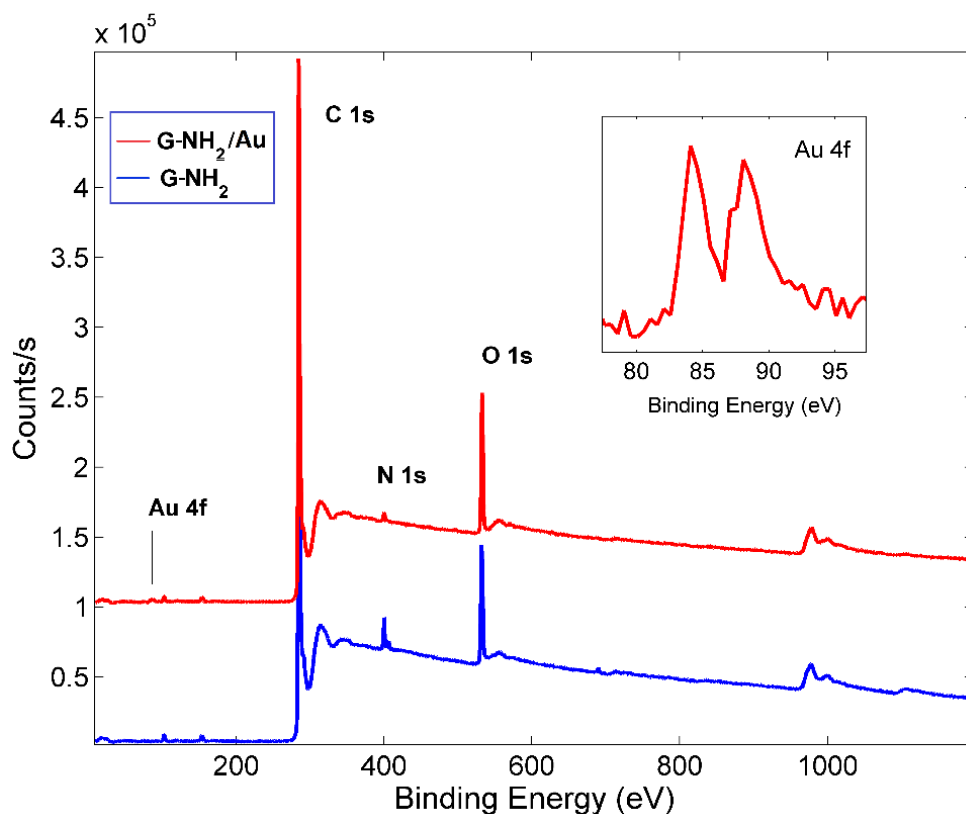


Figure 3.14 XPS wide scan of **G-NH₂** and **G-NH₂/Au** and lineshapes of Au 4f inset.

Sample	C (%)	O (%)	N (%)	Au (%)
G-MNPO	74.8	19.0	6.2	0
G-NH₂	89.3	7.4	3.3	0
G-NH₂/Au	89.0	9.4	1.1	0.5

Table 3.5 Atomic content percentage for *G-MNPO*, *G-NH₂*, *G-NH₂/Au* samples, as determined by XPS analysis.

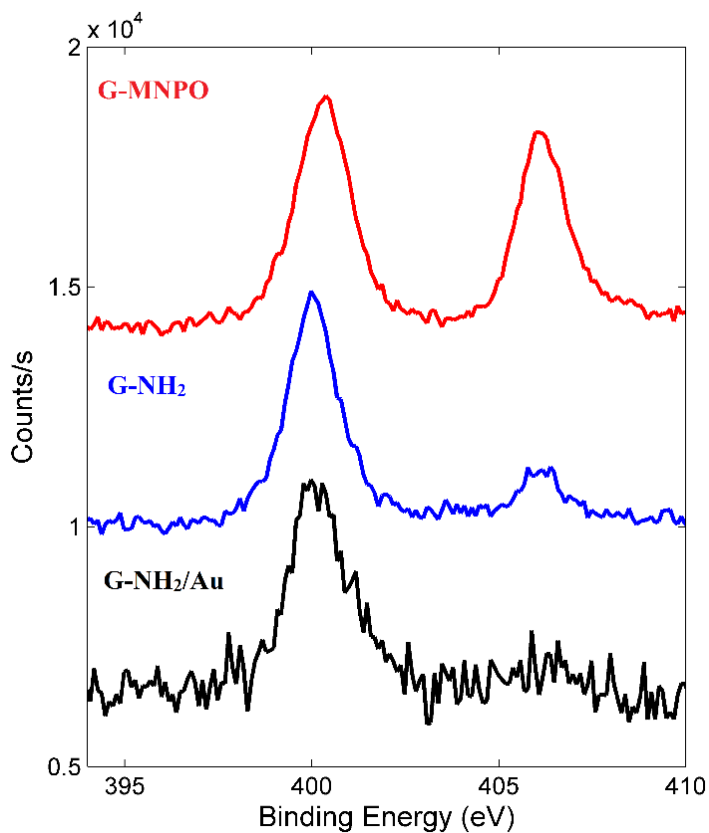


Figure 3.15 *N 1s* photoelectron deconvoluted lineshapes of *G-MNPO*, *G-NH₂*, *G-NH₂/Au*.

Sample	G-MNPO	G-NH₂	G-NH₂/Au
N 1s (N=C, NH ₃ ⁺) %	58.82	79.95	83.66
N 1s (NO ₂) %	41.18	20.05	16.34

Table 3.6 Nitrogen bonding relative atomic content for *G-MNPO*, *G-NH₂*, *G-NH₂/Au* samples, as determined by *N1s* XPS band deconvolution analysis.

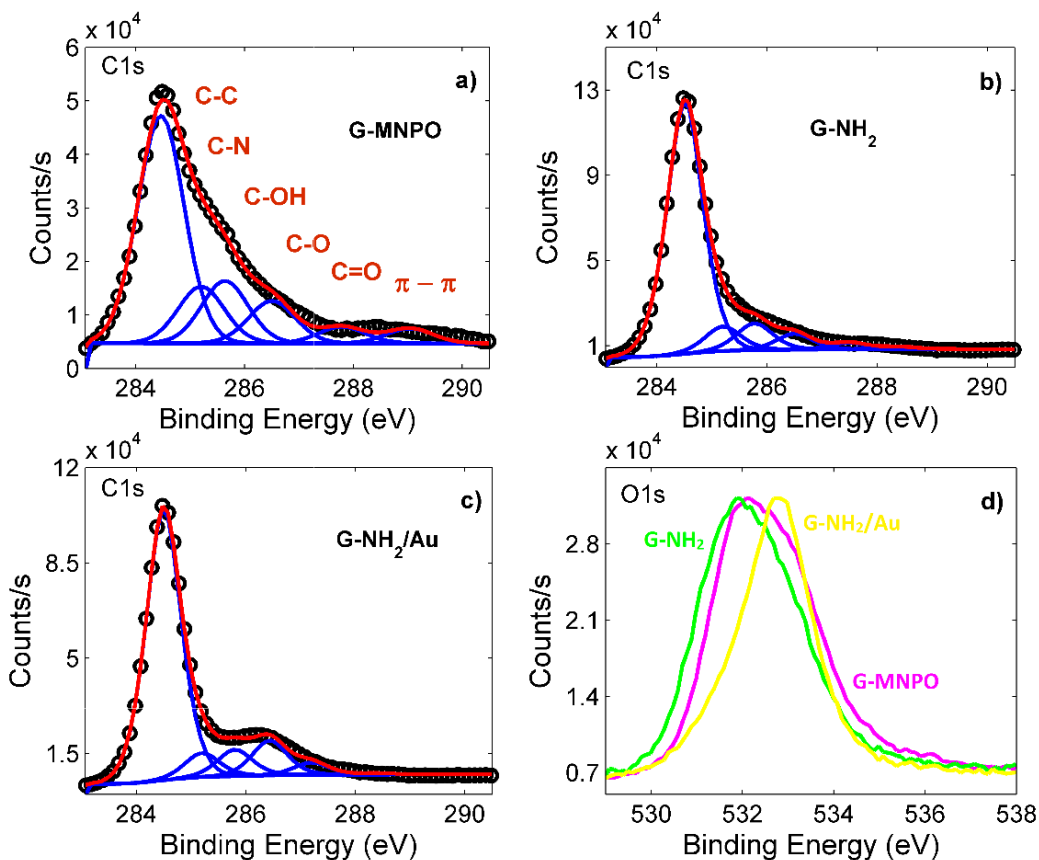


Figure 3.16 C1s photoelectron deconvoluted lineshapes of **G-MNPO** (a), **G-NH₂**, **G-NH₂/Au** (c) sample. O 1s photoelectron deconvoluted lineshapes of **G-MNPO** (violet), **G-NH₂** (green), **G-NH₂/Au** (yellow).

In order to further investigate the structural properties of **G-NH₂/Au** nanohybrids, Raman spectroscopy has been used as a tool. Raman spectra of **G-NH₂** and **G-NH₂/Au** are shown in Fig. 3.17.

In Raman spectrum of **G-NH₂**, the G and 2D features are clearly visible at 1580 and 2720 cm^{-1} , respectively. These peaks can be regarded as the **G** fingerprint. The defected related D-peak is very weak, indicative of the high quality of graphene. The 2D band splitting indicates the presence of a multilayers **G** system. All these Raman contributions are again evident in the **G-NH₂/Au** nanocomposites.

However, some relevant differences can be envisaged. Firstly, the increase of the intensity of all the peaks, due to the presence of Au NPs. The strong electric field gradient induced by the metallic nanoparticles determines an overall change of the dipole moment during the vibration, even in the absence of a polarizability change. On the other hand, when **G** and Au NPs are in close proximity, some Raman forbidden peak appear: the D' at 1616 cm^{-1} and the D+G at about 2925 cm^{-1} contributions.

These evidences can be determined by: *i*) the insertion of Au NPs on **G-NH₂** platform, mainly at the edges of **G** layers (functionalized area of **G** layers) as suggested by computational studies; *ii*) reduced size of layers due to the mechanical effect during the ultrasonication treatment adopted for the preparation of the nanocomposite.

Moreover, the decrease of I_G/I_{2D} ratio, from 1.58 to 0.98, points out a better exfoliation of **G-NH₂/Au** respect to **G-NH₂**; probably the insertion of Au NPs between **G-NH₂** layers promotes their separation.

Finally, the shifting of G and 2D bands suggests the anchorage of Au NPs on **G** surface (Fig. 3.17). Raman signal was collected at several different samples locations to take into account of the Au spatial homogeneity distribution within graphene nanoplatform. The more prevalent types of observed Raman spectra are those reported in the Fig. 3.17.

Morphological information about the Au NPs size and distribution within the **G** layers has been attained by electron microscopy analyses. In particular, STEM images reported in Fig 3.18 show homogeneously distributed exfoliated **G** layers. In several portion of the sample various-dimensional transparent sheets, stacked onto each other, with a thickness of about 2-3 nm, were observed. Particularly, STEM images of **G-NH₂/Au** (Fig. 3.18) show folded sheets with a reduced size

with respect to one (data not show). Moreover, Au NPs characterized by an average size of 15 nm are mainly distributed at the edges of the **G** layers.

All these evidences are an indirect proof that the 1,3-dipolar cycloaddition occurred predominantly at graphene edges, according to the theoretical calculation.

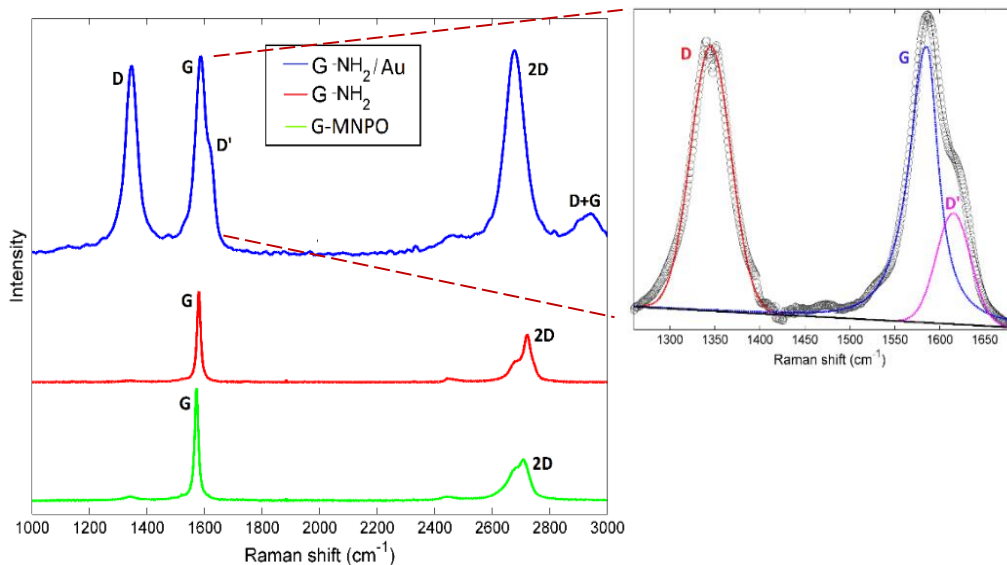


Figure 3.17 Raman spectra of **G-MNPO**, **G-NH₂**, **G-NH₂/Au**. Insert of deconvolution of the D and G bands related to the **G-NH₂/Au** sample.

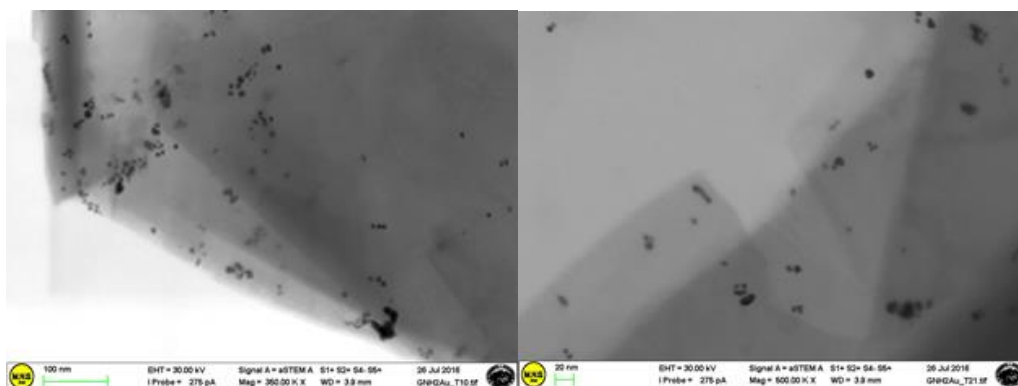


Figure 3.18 STEM images of **G-NH₂/Au**

G-NH₂/Au nanoplatform was tested as surface-enhanced Raman scattering (SERS) substrate; thus the SERS activity of the **G-NH₂/Au** sample was investigated. In order to carry out the SERS measurements Au NPs, **G-NH₂** and **G-NH₂/Au** nanocolloids were deposited onto glass substrates by means of an aerograph supported spraying technique. To test the SERS activity, the samples were immersed for 30 min in rhodamine (R6G dye) aqueous solutions at different concentrations (1×10^{-3} , 2×10^{-4} , 5×10^{-5} M) and then, air dried. Raman spectra were acquired using two different excitation diode laser line (532 nm and 638 nm) and an integration time of 120 s. UV-Visible Spectroscopy helped in determination of appropriate laser wavelength for resonant excitation of the localized surface plasmon (Fig. 3.19). In fact, SERS is more effective when incident radiation falling on the nanostructured substrate is completely absorbed by metal nanoparticles (in our case the Au NPs), so that excitation of the localized surface plasmon can take place. The field enhancement is greatest when the plasmon frequency is in resonance with the incident radiation.

In Fig. 3.19 are shown the optical absorption spectra of the as prepared Au NPs and that of **G-NH₂/Au**. Au NPs in water shows the characteristic Au Surface Plasmon Resonance (SPR) band at 522 nm, due to the coherent oscillations of surface electrons interacting with an external electromagnetic field. When the Au NPs are loaded on **G** surfaces (**G-NH₂/Au**) the Au band shows a red shift from 522 nm to 548 nm (Fig. 3.19). A quenching in the peak intensity was also observed. The slightly red-shift and the decrease of the SPR intensity suggest an increase of the spatial distance between each Au NPs and the others, due to their dispersion into each **G** foil and/or within the graphene layers. Moreover, a charge transfer from Au NPs to **G**, resulting in a decrease in electron density, could occur which, in turn, contributes to the red shift of the surface plasmon absorption.⁽¹⁵⁶⁾

SERS spectra, acquired using the 638 nm laser excitation, are shown in Fig. 3.20. All the spectra show well-defined Raman peaks at about 615, 777, 1189, 1314, 1366, 1513 and 1651 cm^{-1} , characteristic of the R6G dye. The feature at 615 cm^{-1} is assigned to the C–C–C in-plane bending mode, the peak at 777 cm^{-1} to the C–H out-of-plane bending mode and the remaining peaks to the aromatic stretching vibrations of C atoms.⁽¹⁵⁷⁾ These Raman features are clearly observable at 10^{-3} M concentration and less evident, but still visible, for lower R6G concentration values (down to 1×10^{-5} M). On the other hand, if the R6G aqueous solution is deposited onto a **G-NH₂** bare platform (i.e. without Au NPs), even at a 10^{-3} M concentration, no Raman activity is detected. The Raman spectrum of **G-NH₂** is characterized only by broad asymmetric and low intensity bands, positioned near 1580 cm^{-1} (referred as G band) and near 1330 cm^{-1} (referred as D band), typical of carbon-based materials (data not shown). The R6G SERS spectra, obtained on **G-NH₂/Au** platform are very similar to that obtained by using a substrate made from Au nanostructured film (reported in the inset, Fig. 3.20). As a final remark, we observed that, by using a 532 nm laser excitation, no Raman signals could be collected in all the tested conditions. This unusual behavior can be explained taking into account the observed SPR optical absorption red-shift, which certainly lowers the SERS effect.

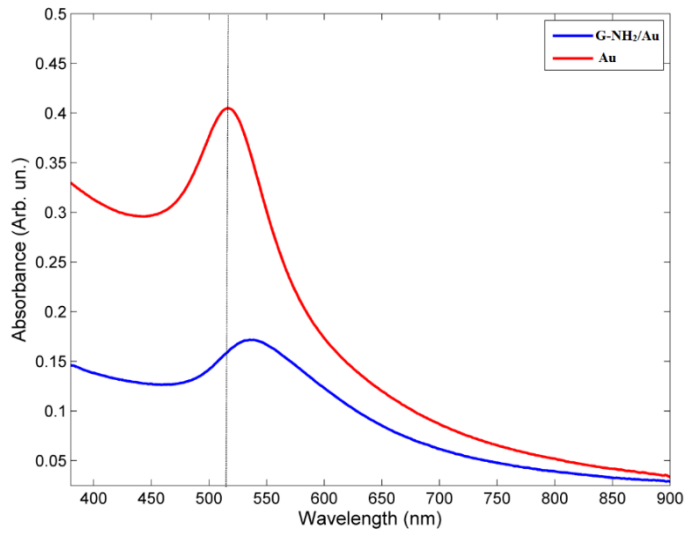


Figure 3.19 Optical absorption spectra of the as prepared PLAL Au nanoparticles and that of the **G-NH₂/Au** sample

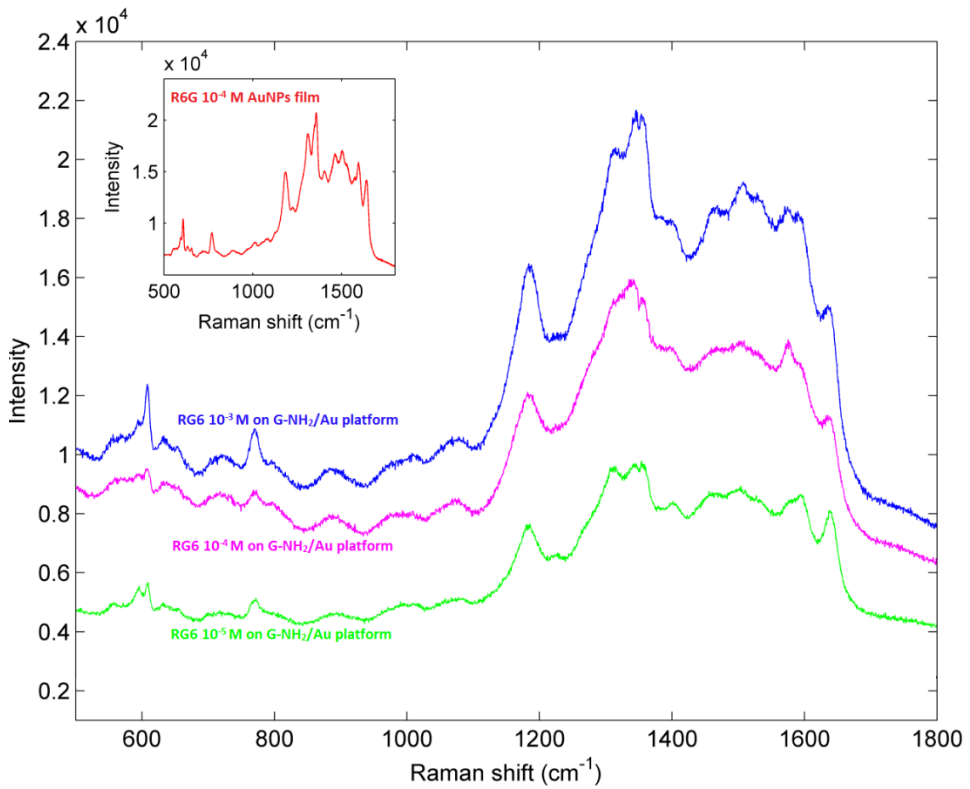


Figure 3.20 SERS spectra of the investigated samples: **G-NH₂/Au platform** tested at three concentration 10⁻⁵, 10⁻⁴ and 10⁻³ M (green, violet and blue respectively).

3.4 Experimental section

Materials

Graphite flakes (GFs), solvents and other reagents were purchased from Sigma Aldrich. **MPO** and **MNPO** were synthesized according to literature procedures.⁽¹⁹⁹⁾ Melting points were determined on a Kofler melting apparatus and are uncorrected. Merck Kieselgel 60F₂₅₄ plates were used for TLC and Merck silica gel 60 (0.063–0.100 mm) for column flash chromatography.

Synthesis of G-MPO, G-MNPO, G-NH₂ and GNH₂/Au

Entry 1, Table 1 (*Synthesis of G-MPO*)

MPO (500 mg) and graphite flake (50 mg) were combined using a mortar and a pestle and the resulting powder was transferred into a glass ampoule. The reaction mixture was heated at 80 °C for 12 h. The mixture was cooled and the solid residue was washed three times with methanol and dimethylformamide (1:1, 3 x 50 mL) and each time sonicated for 10 min and separated from the supernatant by centrifugation at 3500 rpm for 20 min. The effective elimination of unreacted dipole was monitored by NMR analysis of washing solvents. The residue was dried at 60 °C to give 50 mg of **G-MPO1**. From TGA analysis under a N₂ atmosphere, the amount of cycloadduct grafted to graphene was estimated to be ~3.5% wt.

Entry 2-4, Table 1 *Synthesis of G-MPO and G-MNPO*

MPO (Mp: 38–39 °C) or **MNPO** (Mp: 139–142 °C) and graphite flake, in the correct w/w ratio (entries 2–4), were combined using a mortar and a pestle, and the resulting powder was transferred into a glass ampoule. The reaction mixture was sonicated for 6 h at 70 °C, and then heated at 120 °C for 12 h. The mixture was cooled and subjected to a workup procedure. From TGA analysis, the amounts of cycloadduct grafted to graphene were estimated to be ~2.1% wt,

~3.3% wt, and ~4.6% wt for **G-MPO2**, **G-MNPO1**, and **G-MNPO2**, respectively.

Synthesis of G-NH₂

G-MNPO was prepared according to the above reported synthetic method. The cycloaddition reaction was performed using a molar ratio of 1:7 (GF/MNPO).

G-MNPO (240 mg, 1 eq of NO₂) in 30 mL H₂O, has been sonicate for 30 min to obtain a homogenous dispersion. NaBH₄ (100 mg, 10 eq) were added to dispersion. The reaction was stirred at 80°C overnight.

The reaction mixture has been acidified to pH 3, by using a solution of HCl 1M and stirred for 1h at r.t. The reaction mixture was filtered under vacuum (Millipore 0.1 mm). The residue was repeatedly washed in sequence with water/ethanol (1:1) each time being sonicated and separated from the supernatant by centrifugation. The residue was dried, at ~ 60 °C to obtain 185 mg of **G-NH₂**.

Au NP synthesis

The 532 nm second harmonic emission wavelength of a Nd:YAG laser, operating at a repetition rate of 10 Hz (pulse length: 5 ns), was used to prepare the Au water colloids. The beam was focused on the surface of the gold target (3 mm thickness, 99.99% purity) through a mirror tilted at 45° and a lens with a focal length of 20 cm. The laser spot size was about 2 mm in diameter. The ablation process was carried out using a laser fluence of 1.5 J cm⁻², 20 mm of water above the target and an ablation time of 20 min.

Synthesis of G-NH₂/Au

G-NH₂ (52 mg) in 2 mL H₂O was sonicated for 10 min to obtain a homogenous dispersion. Therefore 20 mL of AuNPs was added to graphene dispersion and the mixture has been ultra-sonicated (65% W, 30 min). The reaction mixture was filtered under vacuum (Millipore 0.1 mm). The residue was repeatedly washed with water. The residue was dried, at ~ 60 °C to obtain 44 mg of **G-NH₂**.

Preparation of SERS Platform

In order to carrying out the SERS measurements Au NPs, **G-NH₂** and **G-NH₂/Au** nanocolloids were deposited onto glass substrates by means of an aerography spraying technique. as performed using DFT calculations.

Characterization techniques

¹H-NMR spectra were obtained with a Varian 500 MHz spectrometer. The Fourier Transform Infrared (FTIR, Perkin Elmer Spectrum 100) spectra were collected, in Attenuated Total Reflectance (ATR) configuration, from 4000 to 450 cm⁻¹. The chemical composition and the bonding configurations of the samples were also investigated by means of XPS. The spectra were acquired at room temperature using a Thermo Scientific K-Alpha system, equipped with a monochromatic Al Ka source (1486.6 eV) and an hemispherical analyser operating in constant-pass energy (CAE) mode. The pass energy was set at 200 eV for survey scans and at 50 eV for the XPS core level spectra. A spot size diameter of about 400 μm was adopted while surface charging effects were avoided using an electron flood gun. Raman spectra were carried out, in air at room temperature, using a Horiba XploRA spectrometer equipped with a confocal microscope and a Peltier-cooled charge-coupled detector (CCD). The samples were excited using the 638 nm line from a solid state laser and integrated for 50 s, using a 50s microscope objective. In order to prevent laser-induced damage or heating, measurements were carried out using a low laser power (2.5 mW on the illuminated area of 2.0 μm²). Spectra from several random positions on each specimen were collected on account of the possible spatial non-homogeneity of the samples. To ensure reproducibility, experiments were performed in triplicate. The morphology of graphene samples was analyzed using the Zeiss-Gemini 2 scanning electron microscope, operating, in transmission mode, at 30 kV and at a working distance

of 4 mm. Some drops of the sample, dispersed in isopropanol ($\approx 0.5 \text{ mg mL}^{-1}$) using the Sonics VCX 130 ultrasonic sonicator, were deposited on a 400 mesh holey carbon coated copper grid and left to dry at room temperature for 3 h. TGA experiments were performed by means of Perkin-Elmer Pyris TGA7, in the temperature range 50–800 °C. About 5 mg of each sample was firstly placed in a platinum pan and kept at 25 °C under a 60 mL min^{-1} N_2 flow until balance stabilization, and subsequently heated with a scan rate of 10 °C min^{-1} under the same N_2 flux. The balance sensitivity was 0.1 mg. A baseline recorded in the same measurement conditions with an empty platinum pan was subtracted from each thermogram before data analysis. UV-vis absorption spectra were recorded by means of a PerkinElmer Lambda 750 UV-vis spectrometer in the range 190–1100 nm using quartz cells.

Computational studies

Geometry optimizations of the critical points (reactants, transition structures and products) were studied at the (U)M06-2X level of theory.^(158, 159) For each geometry studied, calculation of harmonic vibrational frequencies was carried out at the same level of theory, with the aim to characterize all structures as minima or transition states. For the minima all the wavenumbers obtained are positive, whereas transition state structures were found to have only one negative eigenvalue with the corresponding eigenvector involving the formation of the newly created bonds. Vibrational frequencies were calculated (1 atm, 298.15 K) for all optimized structures, at the (U)M06-2X/6-31G(d) level of theory, and used, unscaled, to compute both. ZPVE and thermal corrections at 298 K. The enthalpy and entropy changes were calculated from standard statistical thermodynamic formulas.⁽¹⁶⁰⁾ The intrinsic reaction coordinates^(161, 162) (IRC analysis) were also calculated to analyse the mechanism in detail for all the transition structures

obtained at the same level of theory. All the optimizations were carried out by Berny's analytic gradient method ⁽¹⁶³⁾ included in the Gaussian 09 software package.⁽¹⁶⁴⁾ In all cases, full geometry optimization was carried out without any symmetry constraints. The electronic structures of critical points were studied by the natural bond orbital³⁸ (NBO) method as implemented in the Gaussian 09 suite.

Chapter 4

*Peptide self-assembly:
Novel materials with great potential for
biomedical applications*

In this chapter it is described the development of new coiled-coil peptide to be employed in gene-delivery strategy. This research project has been carried out under the supervision of Dr Max Ryadnov and Dr Emiliana De Santis, from the Biotechnology group at the National Physical Laboratory (London, UK).

4.1 Basic concepts about peptide self-assembly

In nature, many cellular components, which are essential for the lifecycle, are rooted by self-assembly processes that involve both inorganic and organic compounds. For example, cell membranes formation is based on phospholipids self-assembly. Also the double helix of DNA is generated by a self-assembly process due to hydrogen bond interactions between nucleotide bases. Even the formation of proteins tertiary and quaternary structures involves self-assembly processes based on folding of polypeptide chains.⁽¹⁶⁵⁾

The self-assembly processes allow to obtain well-ordered nanostructures and it justifies the increasing interest to develop many nanosystems based on these self assembly processes for biomedical applications.⁽¹⁶⁶⁾

Currently, the mechanism of self-assembly is not yet understood in details. Probably, external stimuli induce a transition of the biomaterial to a self-assembled system by means of noncovalent interactions including hydrogen bonding, stacking phenomena, electrostatic interactions and Van der Waals forces.⁽¹⁶⁶⁾

Among organic compounds involved in self-assembly processes, major attention has been focused on peptides, due to their unique properties such as biocompatibility, biodegradability, versatility and chemical diversity.⁽¹⁶⁵⁾ The peptides are able to form several types of nanostructures like tubules, fibers, vesicles, spheres, etc. The kind of nanostructures obtained depend on the peptide sequence as well as on the spatial arrangement of the peptidic chains within one construct (i.e. topology).⁽¹⁶⁶⁾

Concerning the biomedical field, self-assembled peptides exhibited several attractive features for applications in tissue regeneration, preparation of surfactants, drug delivery, biological surface engineering and antibiotics (Fig. 4.1).^(167, 168)

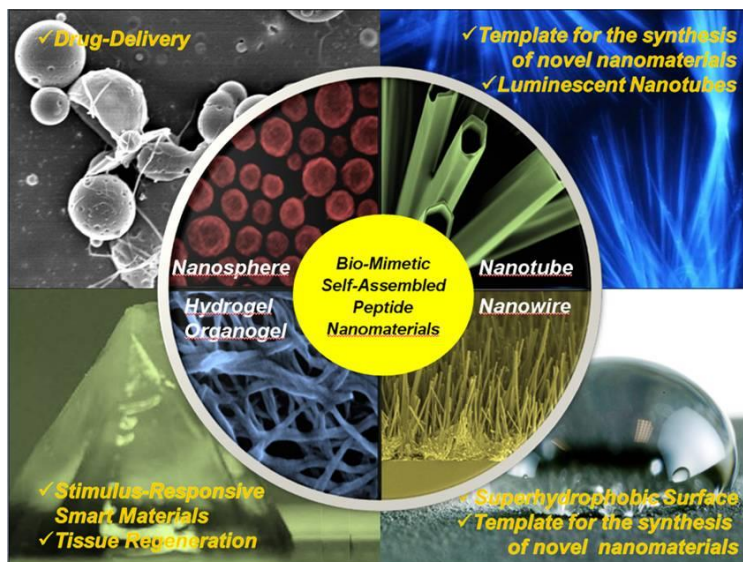


Figure 4.1 Representative illustration of potential applications of self-assembled peptide nanomaterials

Natural occurring proteins can adopt two different types of secondary structures, α -helix and β -strand. These secondary structures are induced by hydrogen bond interactions between the amino acids present in the linear peptide chain (Fig. 4.2). The protein's behavior to assume α -helix and β -strand conformation depends only on the nature of the amino acids, the basic building blocks of the peptide framework. The α -helix arrangement is due to interactions intra-peptide along the peptide backbone. This particular structure allows to obtain α -helices with a wrapped form and an unlimited length. In β -strands instead, hydrogen bond interactions occur inter-peptide, therefore the conformation of the resulting peptide is more extended respect to the α -helix. In contrast to the unlimited length of the α -helices, the amino acid sequences of β -strand are commonly less than 10 units.⁽¹⁶⁹⁾

The β -strands undergo a lateral assembly process to form β -sheets, which can subsequently self-assemble to nanofiber structures, by electrostatic and hydrophobic interactions.⁽¹⁶⁸⁾ In particular, nanofibers are used to build hydrogel scaffolds for tissue engineering, having properties similar to those of natural extracellular membrane.⁽¹⁷⁰⁾ These scaffolds are employed for cellular cultures in several cases like: human carcinoma, embryonic kidney, hepatocytes neuroblastoma, fibroblasts, neural stem cells, embryonic stem cells. In these contexts, many authors reported a good cellular growth.⁽¹⁷¹⁻¹⁷³⁾

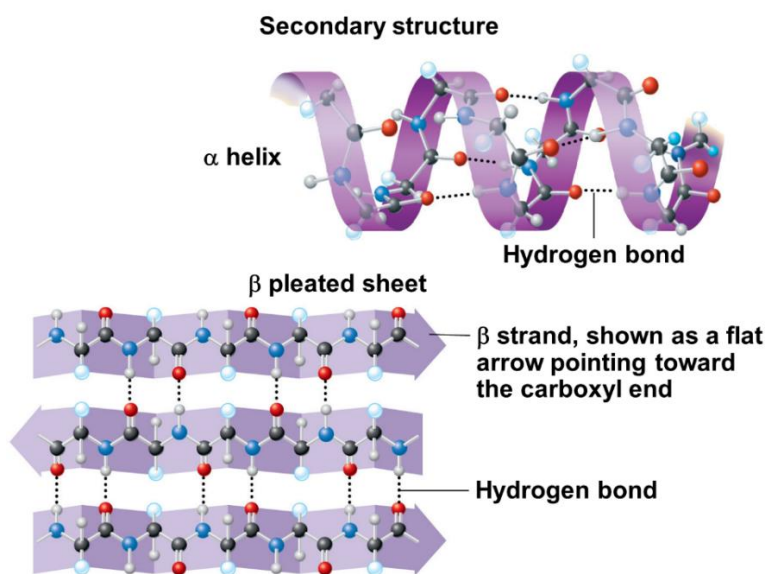


Figure 4.2 Secondary structures of proteins

Moreover, these scaffolds seem to be able to control the cell differentiation, therefore they could be used in regenerative medicine applications.^(172, 173)

β -sheets were also used to prepare self-assembled bi-layer structures, nanotubes and nanovesicles.⁽¹⁷⁴⁾ Several kind of drugs, whose limited activity is due to their poor solubility in aqueous media, can be encapsulated inside these structures. This

strategy of circumventing solubility issues might increase the stability of the drugs as well as their bioavailability and their half-life time. ^(175, 176)

Other reports showed the preparation of β -sheet nanosystems embedding DNA fragments, assembled by ionic interactions and employed as vectors in gene delivery. ⁽¹⁷⁷⁾

Pairwise, peptides characterized by an α -helix conformation have been investigated as models to prepare several systems for biomedical applications. The α -helices, through a self-assembly process, can wrap each other forming a supercoil, either right- or left-handed. ⁽¹⁶⁹⁾

Unlike β -sheets, the resulting coiled-coil systems showed more stability and action specificity. In nature about 200 types of coiled-coil systems have been identified; they are involved in a wide variety of important biological processes like: metabolism, transcription, muscle contraction etc. ⁽¹⁷⁸⁻¹⁸⁰⁾

4.2 Coiled-coils

The common coiled-coil structure proposed by Crick is composed of two or three α -helices wrapping around each other in a parallel fashion, left-handed, with a pitch of 18.6 nm and a pitch angle of about 20° . ⁽¹⁸¹⁾ The interaction between more helices reduces the typical α -helical pitch from 3.6 to 3.5 residues per turn, creating an interfacial stripe between associating helices. ⁽¹⁸²⁾ The coiled-coils can be formed by same (homotypic) or different (heterotypic) helices. ⁽¹⁸³⁾ The helices can have two different orientation, *i.e.* parallel or anti-parallel, and the number of strands can change from two to five. ⁽¹⁸⁴⁾

The heptad is the basic unit of a typical coiled-coil system and it is a sequence of seven amino acids. The number of heptads that forms a coiled-coil is considerably variable, ranging from over 200 heptads, in fibrous proteins, down to only two heptads in *de novo* designed synthetic coiled-coil. ⁽¹⁸⁴⁾

The heptads are composed by a regular alternation of hydrophobic and hydrophilic amino acid residues, HPPHPPP, also referred to as *abcdefg* (Fig. 4.3). The positions occupied by amino acid residues in the sequence shape the coiled-coil supramolecular structure.⁽¹⁸⁴⁾

Charged residues, the most common being Lysine and Glutamic Acid, Glutamine and Alanine, occupy the positions *e* and *g*. Instead, hydrophobic residues such as Leucine and Isoleucine, are present in positions *a* and *d*. During the self-assembly process, *a* and *d* residues build the inter-helical hydrophobic core, stabilized by both hydrophobic and Van der Waals interactions (Fig. 4.3). At the same time, *e* and *g* residues form inter-helical electrostatic interactions, which help to stabilize the coiled-coil structure (Fig. 4.3).⁽¹⁸⁵⁾

Regarding *b*, *c* and *f* positions, they offer greater flexibility. Commonly, in coiled-coils *de novo* design strategy, these positions are occupied by amino acids able to confer solubility properties to the peptide or to control the degree of aggregation of the polypeptide by interactions on the external surface of the coiled-coil.

This specific arrangement permits the formation of only one type of secondary structure, the α -helix. This phenomenon is presumably due to the repetitiveness of the amino acid sequences.⁽¹⁸²⁾

Recently, *de novo* design proteins showed basic units formed by eleven residues, rather than the canonical seven residues; this induces a change from left-handed to right-handed, due to a change of the hydrophobic pattern.⁽¹⁸⁶⁾

By contrast with the high specificity of the secondary structure, the tertiary and the quaternary structures of the proteins are subjected to many variations, influencing the peptide's behavior in biological environment. For example, Glycine and Proline are usually present in α -helical breakers and rarely are chosen to design the central region of *de novo* coiled-coils. Cysteine is usually discarded in the design of new coiled-coils because it can form disulphide bridges by spontaneous oxidation. This

process determines the formation of cross-linking networks along the peptide chains, decreasing the flexibility of the protein structures.⁽¹⁸³⁾ However, in recent works, Cysteine has been used to prepare complex multi-hub systems interconnected by cross-linking bonds. For example, Woolfon and co-workers prepared a system based on the self-assembly process between two complementary hubs. These hubs were prepared by disulfide bonds between a heterodimeric α -helix chain and a homo-trimeric coiled-coil system.⁽¹⁸⁷⁾

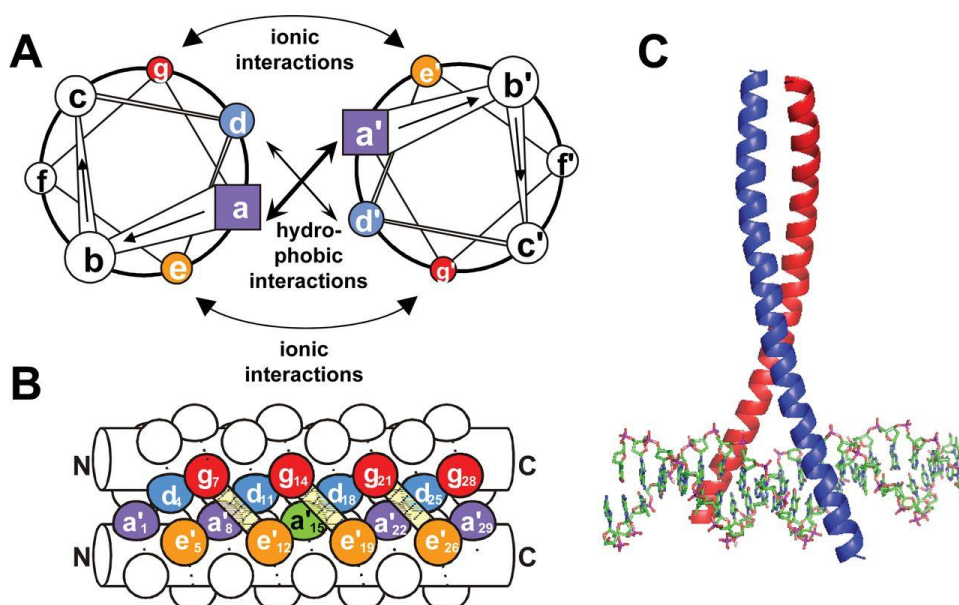


Figure 4.3 Coiled-coil peptide structure: A) Helical wheel representation (top view), B) intermolecular interactions between two α -helices represented as cylinders, C) Coiled-coil dimers

The coiled-coils can self-assemble into a variety of different morphologies (e.g. nanofibers), which has inspired scientists to prepare *de novo* coiled-coils. It has been demonstrated that by changing the amino acids at *c*, *b* and *f* positions is possible to control the length and the thickness of the resulting fiber. In particular, a Tyrosine residue in *f* position is able to reduce the length of the fiber and this decreases the integrity of the fiber itself, destabilizing the helix.⁽¹⁸⁸⁾ Moreover, it

has been demonstrated that an Arginine residue at the *d* position causes the block of the hydrophobic periodicity of the heptad-repeating unit, therefore the resulting oligomers are not able to self-assemble.⁽¹⁸⁹⁾

Coiled-coils can also form nanotubular structures. Recently, a series of *de novo* coiled-coil peptides characterized by two hydrophobic faces, self-assembling into nanotubes, were developed. These structures are similar to TolC, an outer-membrane protein of *Escherichia coli*, composed of 12-stranded antiparallel β -barrel and 12-stranded anti-parallel α -helical cylindrical tubes. The strategy consists of substituting the bulky residues at *a* and *f* positions with Alanine. This induces a decrease of the curvature degree between adjacent helices. Moreover, the formation of cylindrical structures is favored by introducing charged residues at *b* and *e* positions. In this kind of structures the helices ran perpendicular to the axis of the overall fiber.⁽¹⁹⁰⁾

Beyond fibers and nanotubes, the coiled-coils can also be used to prepare more complex three-dimensional structures. In particular new strategies are focused on creating new systems through the association of ionic hubs by electrostatic interactions.⁽¹⁸⁴⁾ Several kinds of drug delivery systems are based on coiled-coils. The coiled-coils have a hydrophobic core wherein is possible to introduce drugs characterized by a limited solubility. Several studies have demonstrated an improvement of pharmacokinetic profile of this kind of drugs. For example it was prepared a complex formed by Pt (IV) incorporated in RHCC (right-handed coiled-coil) domain, from *Staphylothermus marinus* (20 kDa), for glioblastoma treatment. Pt(IV) kinetically inert, can be activated to Pt(II) in a hypoxic extracellular tumour environment. This complex showed an improvement of chemotherapeutic efficacy and selectivity toward human glioblastoma cells and tolerability.⁽¹⁹¹⁾

The coiled-coils are employed also to prepare polymer-drug conjugated systems. Recent works described the internalized process of these systems through an easily

endocytosis mechanism.⁽¹⁹²⁾

Moreover, coiled-coils are used to build liposome anticancer systems for drug release. In particular, their sensibility to temperature changes was exploited to prepare a system for DOX delivery. It has been demonstrated that the DOX is released at the melting point of coiled-coils at about 42 °C.⁽¹⁹³⁾

Currently, the coiled-coils are investigated as multivalent platforms for immunological applications. It was understood that the key to prepare an efficient vaccines is to create multivalent platforms of antigens, these are characterized by an increasing immunogenicity respect to classic vaccines. To care various diseases, several vaccines are developed with this strategy including HIV⁽¹⁹⁴⁾, influenza⁽¹⁹⁵⁾ and recent remarkable issues such as Zika and Ebola.⁽¹⁸⁶⁾

Regard to the opportunity to prepare new complex systems characterized by antiviral activity, based on coiled-coils, in a recent work the preparation of an antiviral building block system constituted by a pentameric coiled-coil sequence linked to a trimeric coiled-coil peptide was described. The studies established that this building block system is able to become a nanoparticle-shaped protein by self-assembly process. On the surface of this building block it was inserted a trimeric coiled-coils B cell epitope (HRC1), which is involved in severe acute respiratory syndrome. The biological studies have demonstrated an antibodical activity of this system and the ability to neutralize the virus.⁽¹⁹⁶⁾ Recently, this system is also employed to prepare vaccines for HIV and Malaria.⁽¹⁸⁶⁾

In conclusion, the coiled-coils offer the possibility to prepare new biocompatible nanomaterials characterized by unique properties and selective action, for several biomedical applications. Their integration onto a **G** platform could be of potential interest to prepare multi-functional drug/gene delivery system.

4.3 SD1: a peptide for gene-delivery

During the time spent at NPL the work project has been focused on development, synthesis and characterization of a coiled-coil peptide for gene-delivery.

The primary sequence of the peptide (**SD1**) was engineered using the typical design of coiled-coils previously described. It is composed by 39 amino acids with hydrophobic residues at the positions *a* and *d* and charged residues at the position *e* and *g* respectively, which are essential to form the inter-helical hydrophobic core, stabilized by inter-helical ionic interactions.

SD1 was obtained by solid phase synthesis using Fmoc (N-(9-fluorenyl)methoxycarbonyl) chemistry on a peptide synthesizer. The synthetic procedure is based on: *i*) attachment of the first N^α protected amino acid; *ii*) deprotection of N^α; *iii*) activation and coupling of N-protected amino acids; *iv*) cleavage of the peptide chain prepared from the resin. HCTU/DIPEA are used as coupling agents and piperidine solution (DMF) as deprotector agent.

SD1 has been purified by reverse-phase semipreparative gradient HPLC and its identity and purity were confirmed both by MALDI-TOF mass spectrometry by using *α*-cyano-4-hydroxycinnamic acid as the matrix (Fig. 4.4) and by reverse-phase analytical HPLC.

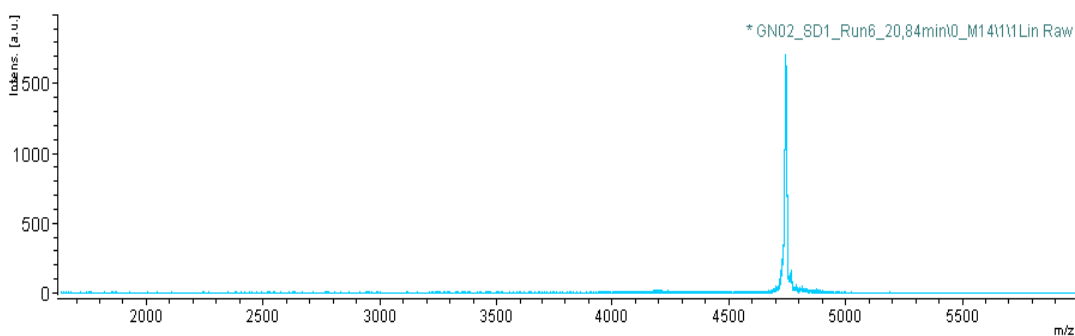


Figure 4.4 **SD1** MalDI-TOF mass spectrometry

In order to prepare a peptide coiled-coil system to be employed in biomedicine field **SD1** must show an α -helix conformation. This is a necessary requirement to prepare a coiled-coil *via* peptide self-assembly process.

Therefore the peptide folding was investigated by Circular Dichroism (CD) and Fourier Transform Infrared (FT-IR) spectroscopies.

The CD spectra showed a positive band at 190nm, together with negative bands at 207nm and at 224nm, which correspond to π - π^* and n - π^* electronic transitions of the amide chromophore typical of an α -helix folding (Fig. 4.5).

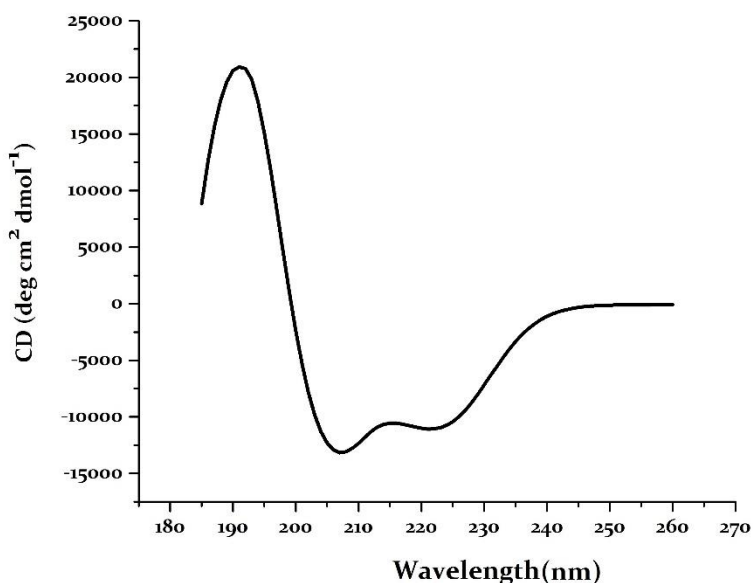


Figure 4.5 SD1 CD

The α -helix folding was also confirmed by FT-IR (Fig. 4.6). The FT-IR spectra showed an amide I band at 1644 cm^{-1} due to C=O stretch vibrational modes and an amide II band at 1552 cm^{-1} due to in-plane NH bending modes and CN stretching vibrational modes.⁽¹⁹⁷⁾ The amide I band is found at a lower wavelength than that typically observed for an isolated α -helix (1654 cm^{-1})⁽¹⁹⁸⁾. This may be attributed

to a distortion of the helix resulting from the self-assembly of the helices into coiled-coil superhelices.

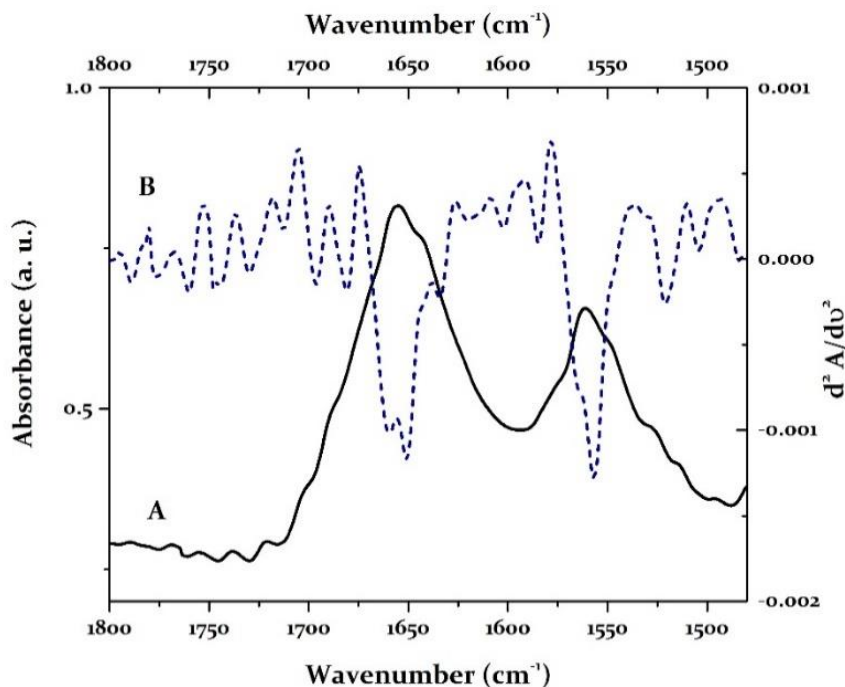


Figure 4.6 SD1 FT-IR: A) Original Spectrum, B) Second derivate spectrum

The CD analysis was also used to follow the stability of the peptide folding with increasing temperature from 20 °C to 90 °C and back to 20 °C to check for reversibility. The CD spectra decreased in intensity upon heating as result of an increased conformational flexibility. The presence of an isodichroic point at 203 nm is indicative of an interconversion between two species, from α -helical to unfolded structure. CD spectra at 20 °C before and after thermal unfolding revealed an almost complete reversibility of folding (Fig. 4.7). The thermal denaturation gave a sigmoidal unfolding curve, indicative of a folded structure. The first derivative curve shows the melting temperature at 45 °C and 64 °C (Fig. 4.8).

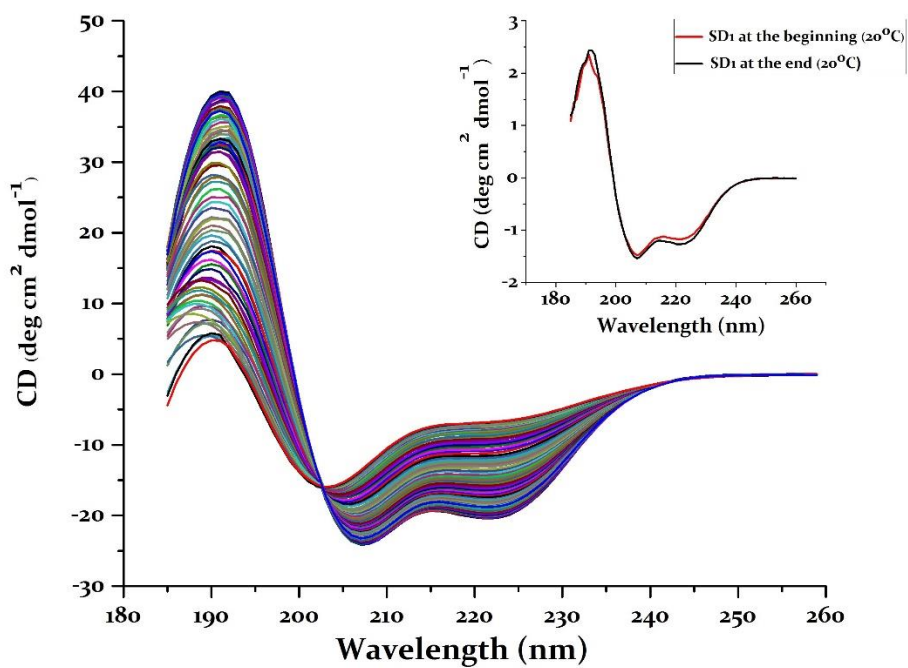


Figure 4.7 SD1 CD.

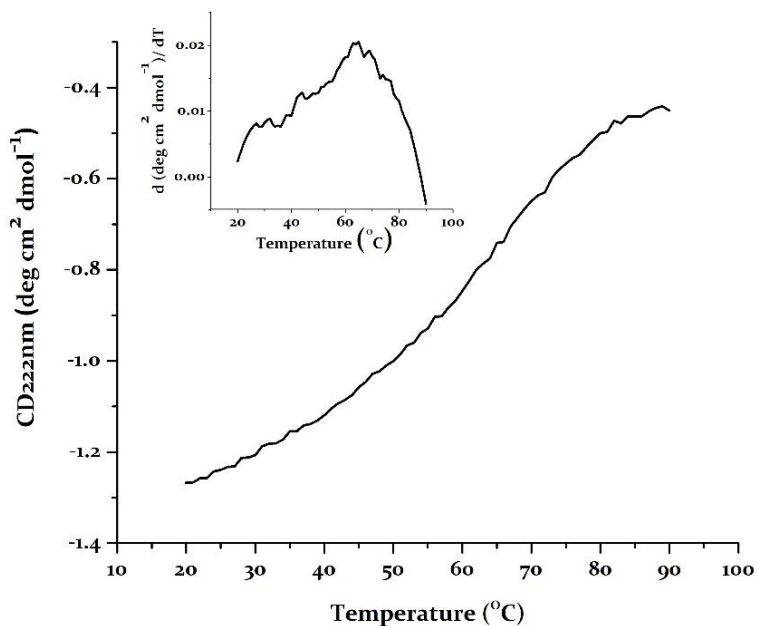


Figure 4.8 SD1 CD

The next step was the investigation the ability of **SD1** to undergo a self-assembly process.

TEM analysis (Fig. 4.9) confirmed the peptide self-assembling. **SD1** formed spherical structures of estimated dimensions between 200 and 50 nm. The spherical morphology of this system makes it a useful candidate as gene delivery vehicle.

First of all **SD1** must fulfill some essential conditions to be used as gene delivery vehicle: *i)* have a great affinity to genetic material and therefore the capacity to protect it; *ii)* bind the genetic material without destroying or altering it; *iii)* be able to enter in the endosomal membrane and delivery it to the nucleus.

The affinity between our peptide **SD1** and small interfering RNA (siRNA) was tested at Diamond Light Source (Didcot, UK). The binding interaction between these two species was qualitatively established by synchrotron radiation CD (SRCD), at different charge ratio siRNA/SD1. The subtraction of the CD signal of the peptide and the siRNA from that of the complex showed a residual CD signal (Δ CD), clearly evidencing the formation of a new complex (Fig. 4.10).

The work is still in progress. A full titration by CD will be performed to quantify the binding alongside biological studies, such as gene transfection and knock-down, to quantify the binding between the peptide and siRNA and to assess the ability of the peptide to transport functional siRNA inside the cells.

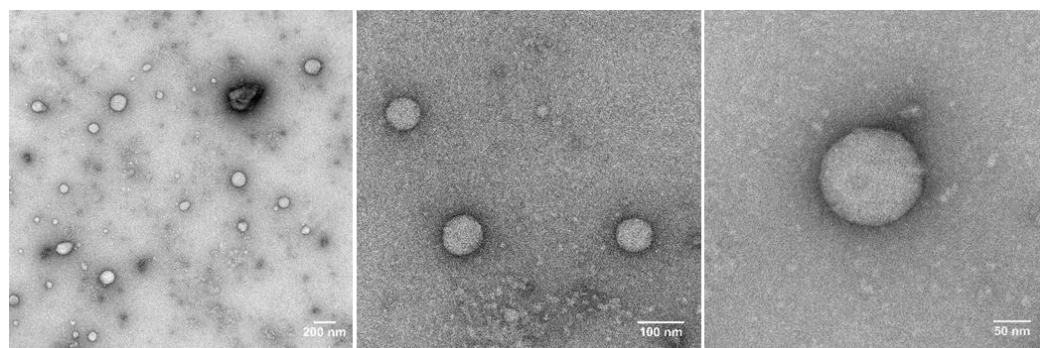


Figure 4.9 **SD1** TEM

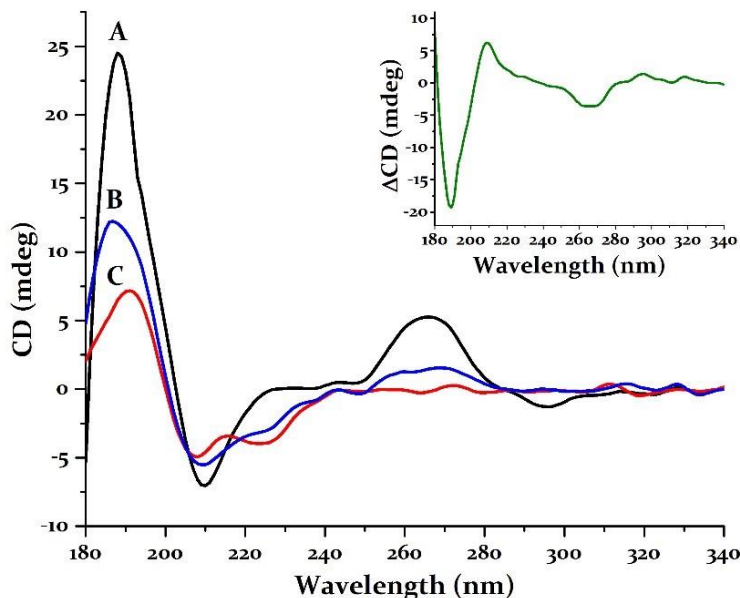


Figure 4.10 CD Binding *SD1*: A (*siRNA*), B (*SD1*), C (Complex at Charge Ratio 1.575)

4.4 Experimental section

SD1 synthesis

SD1 was prepared by on a Liberty microwave peptide synthesizer (CEM Corporation), using standard solid phase Fmoc (N-(9-fluorenyl(methoxycarbonyl) protocols on Rink amide-4-methylbenzhydrylamine resins (0.236 gr) with HBTU (50 mL) and DPEA (50mL) as activator agents and a solution 20% Piperidine in DMF (308 mL) as deprotecting agent, DMF (6339 mL) is the reagent solvent.

Each amino acid was solubilized in DMF; the amino acid amount is reported in Table 4.1.

The reaction time was set at about 26 hours and the peptide was cleaved from the resin afterwards. The crude of reaction was washed in sequence with DMF and DCM. The residue was treated with 5 mL of cleavage solution [TFA:TIS:H₂O

(9.5:0.25:0.25)]. After 3 hours the residue was filtered off and washed with 3 mL of cleavage solution.

The product was diluted with diethyl ether and ultracentrifugated at 3500 rpm for 45 min at 4 °C; the supernatant was taken off and the residue underwent sonication for 15 min. in water. **SD1** was then lyophilized affording 173 mg of product.

SD1 (173 mg) was solubilized in 22 ml buffer A (95% H₂O, 5% MeCN) and purified by High Performance Liquid Chromatography using Vydac C18 analytical (5 μm) column. The analytical run used a 10-90% buffer B (MeCN 95%, H₂O 5%) gradient over 50 min. **SD1** was identified by MALDI-ToF. MS [M + H]⁺: m/z 4732.02

Amino acid	gr	mL of DMF
F-MOC-Ala-OH	0.74	12
FMOC-Arg(Pbf)-OH	4.27	25
FMOC-Asp(OtBu)-OH	0.49	6
FMOC-Gln(Trt)-OH	1.10	9
FMOC-Glu-OtBu-OH	1.70	20
FMOC-Gly-OH	0.36	6
FMOC-Ile-OH	0.85	12
FMOC-Leu-OH	1.06	15
FMOC-Lys(BOC)-OH	1.40	15
FMOC-Tyr(tBu)-OH	0.49	16
βAla-FMOC	0.43	7

Table 4.1 Amino acids used to synthesis **SD1** peptide

Characterization techniques

Fourier transform infrared spectroscopy FT-IR spectra were registered using a Tensor-27 series FT-IR spectrometer equipped with a BioATR II unit (Bruker

Optics), as the sampling platform, and a photovoltaic mercury cadmium telluride (MCT) detector and a Bruker Optics workstation equipped with OPUS software.) The peptide samples (100 μ M, 50 μ L) were prepared by using a MOPS solution (10 mM, pH 7.4). They were located in a circular sampling area of radius 2 mm with a path length of 6 μ m. FT-IR spectra were registered with resolution 4 cm^{-1} , scanner velocity 20 kHz, 256 scans, phase resolution 32 and zero filling factor 4. Gaussian peak fitting (proprietary software) has been used for the spectra deconvolutions.

High Resolution Transmission Electron Microscopy (HR-TEM)

The morphology of SD1 sample was investigated by using FEI Tecnai 20 twin lens scanning transmission electron microscope, operated at 200 kV. The grids has been prepared by placing few drops of buffer solution on glow discharge treated Cu grids, coated with pioloform and carbon film, stained with uranyl acetate (1%, wt) for a few seconds. Afterword, the buffer excess was removed. Few drops of sample water solution were placed on grids, the excess is removed and after uranyl acetate staining is applied. High resolution images were obtained by using FEI Eagle 4kx4k CCD. Circular Dichroism (CD) Spectroscopy. CD spectra were registered on nitrogen-flushed J-810 circular dichroism spectropolarimeter (JASCO) fitted with Peltier temperature controller. Sample solutions (100 μ M, 200 μ L), were prepared by using a filtered MOPS solution (10 mM, pH=7.4). They were loaded on a circular Quartz cell ($l = 0.05$ cm) and the data collected with a 1 nm step and 1 second collection time per step is presented as the average of 2 scans. Same experimental conditions are applied in thermal stability analysis.

Titration curves were obtained on nitrogen-flushed Module B end-station spectrophotometer at B23 beamline (Diamond Light Source, UK). Samples were loaded on a circular Quartz cell ($l = 0.01$ cm, $V = 20\mu$ L), and the data collected with a 1 nm step and 1 second collection time per step is presented as the average of 4 scans. Peptide working solution (100 μ M), buffer solution (filtered MOPS solution,

10mM pH=7.4) and siRNA tritated (100-400 μ M) has been prepared. Applied Photosystem Chirascan spectropolarimeter was used to obtain tritration curve. All measurements were taken in ellipticities in mdeg and after baseline correction were converted to mean residue ellipticity by normalising for the concentration of peptide bonds and cuvette path length ($MRE = \theta/110xc$, where l: path length; c: molar concentration; x: number of peptide bonds).

Acknowledgements

It would have been impossible to carry out the research project, described in this thesis, without the passionate support and input of many people. Therefore, I wish to thank all of them.

The first person that I want to thank is my PhD supervisor Prof. Anna Piperno. She has been my guide; our discussions have been a fundamental incentive to grow and improve myself. She taught me to never give-up, to study and to investigate all aspects to reach the goal.

A sincere and deeply thankfulness goes to Dr Enza Fazio. She has been a second scientific guide, a source of inspiration and an honest friend of mine.

I would like to thank:

Dr Angela Scala and Dr Nicola Micale, for their scientific suggestions and their important and continuous support during these years.

Dr Massimiliano Cordaro for his friendship and for the help he gave me to face and solve laboratory issues.

Prof. Giovanni Grassi and Prof. Francesco Risitano for helpful discussion and comments.

I wish to express my sincere gratitude to all people which gave a precious support to the development of the topic discussed herein: Prof Placido G. Mineo, Prof Antonio Rescifina, Dr Francesco Barreca, Dr Antonino Mazzaglia, Dr Davide Barreca, Dr Anna Tampieri and Dr Silvia Panseri.

I am also very grateful to Dr Max Ryadnov for the opportunity he gave me to work in his Biotechnology laboratory at National Physical Laboratory (NPL). A special thank goes to Dr Emilina De Santis, my scientific guide during the time spent in NPL and an honest friend. Her teaching style and enthusiasm for this job have been

an inspiration source for me. I would like also to thank Dr Angelo Bella and Dr James Noble for the enjoyable time spent together.

A sincere thankfulness goes to Simona Grimato: her continuous support has been very important for me during these years.

I would like to thank Prof Fausto Puntoriero, Dr Francesco Nastasi, Emanuele La Mazza, Tania Salerno and Dr Maria Chiara Trapani, for their friendship.

I wish to thank my family for the everyday unconditional love and encouragement. Last, but not the least, a special thank goes to my boyfriend Antonio, for his continuous support in my life. He has selflessly given more to me than I ever could have asked for.

References

1. A.L. Geim, A.H. MacDonald, *Physics Today*, 2007, Vol. **60**, p. 35.
2. J.H. Chen, C. Jang, S. Xiao, M. Ishigami, M. S. Fuhrer, *Nature Nanotechnology*, 2008, Vol. **3**, p. 206.
3. A.A. Balandin, S. Ghosh, W. Bao, I. Calizo, D. Teweldebrhan, F. Miao, C. Ning Lau, *Nano Lett.*, 2008, Vol. **8**, p. 902.
4. R.R. Nair et. al., *Science*, 2008, Vol. **320**, p. 1308.
5. Scientific Background on the Nobel Prize in Physics 2010: **GRAPHENE. Sciences, Class for Physics of theRoyal Swedish Academy of. 2010**, *Royal Swedish Academy of Sciences, Stockholm*.
6. J. Kim, Y. Piao, T. Hyeon., *Chem. Soc. Rev.*, 2009, Vol. **38**, p. 372.
7. X. Huang, X. Qi, F. Boey, H. Zhang., *Chem. Soc. Rev.*, 2012, Vol. **41**, p. 666.
8. A. Bianco, H.M. Cheng, T. Enoki, Y. Gogotsi, R.H. Hurt, N. Koratkar, T. Kyotani, M. Monthieux, C. R.Park, J.M.D. Tascon, J. Zhang, *Carbon*, 2016, Vol. **61**, p. 1.
9. A. Criado, M. Prato et al., *Angew.Chem. Int.Ed.*, 2015, Vol. **54**, p. 10734.
10. K. S. Novoselov, A. K. Geim, S. V. Morozov, D. Jiang, Y. Zhang, S. V. Dubonos, I. V. Grigorieva, A. A. Firsov., *Science*, 2004, Vol. **306**, p. 666.
11. K. R. Paton, E. Varrla, C. Backes, R. J. Smith, U. Khan, A. O'Neill, C. Boland, M. Lotya, O. M. Istrate, P. King, T. Higgins, S. Barwich, M. Peter, P. Pucz, V. Nico, J. N. Coleman., *Nat. Mater.*, 2014, Vol. **13**, p. 624.
12. W. Norimatsu, M. Kusunoki, *Phys. Chem. Chem. Phys.*, 2014, Vol. **16**, p. 3501.
13. X. Li, W. Cai, J. An, S. Kim, J. Nah, D. Yang, R. Piner, A. Velamakanni, I. Jung, E. Tutuc, S. K. Banerjee, L. Colombo, R. S. Ruoff., *Science*, 2014, Vol. **324**, p. 1312.
14. M. Cai, D. Thorpe, D. H. Adamson, H. C. Schniepp, *J. Mater.Chem.*, 2012, Vol. **22**, p. 24992.

15. V. Georgakilas, M. Otyepka, A.B. Bourlinos, V. Chandra, N. Kim, K.C. Kemp, P. Hobza, R. Zboril, K.S. Kim, *Chem. Rev.*, 2012, Vol. **112**, p. 6156.
16. R. Gažák, K. Purchartová, P. Marhol, L. Živná, P. Sedmera, K. Valentová, N. Kato, H. Matsumura, K. Kaihatsu, V. Křen, *Eur. J. Med. Chem.*, 2010, Vol. **45**, p. 1059.
17. T. Skaltsas, N. Tagmatarchis, S. Pispas, *Curr. Org. Chem.*, 2015, Vol. **19**, p. 1800.
18. D. Jiang, B. G. Sumpter, S. Dai, *J. Phys. Chem. B*, 2006, Vol. **110**, p. 23628.
19. Y. Cao, K. N. Houk, *J. Mater. Chem.*, 2011, Vol. **21**, p. 1503.
20. M. Quintana, A. Montellano, A. E. D. Castillo, G. Van Tendeloo, C. Bittencourt, M. Prato, *Chem. Commun.*, 2011, Vol. **47**, p. 9330.
21. B. Jin, J. Shen, R. F. Peng, C. D. Chen, Q. C. Zhang, X. Y. Wang, S. J. Chu, *Ind. Eng. Chem. Res.*, 2015, Vol. **54**, p. 2879.
22. P. A. Denis, *Chem.–Eur. J.*, 2013, Vol. **19**, p. 15719.
23. W. Y. Zan, *Appl. Surf. Sci.*, 2014, Vol. **311**, p. 377.
24. S. Sarkar, E. Bekyarova, S. Niyogi, R. C. Haddon, *J. Am. Chem. Soc.*, 2011, Vol. **133**, p. 3324.
25. B. Wang, J. Wang, J. Zhu, W. et al., *ACS Macro Let.*, 2014, Vol. **8**, p. 1862.
26. B. Li, L. Zhou, D. Wu, H. Peng, K. Yan, Y. Zhou, Z. Liu, *ACS*, 2011, Vol. **5**, p. 5957.
27. L. Shahriaiy, A. Athawale, *International Journal Renewable Energy and Environmental Engineering*, 2014, Vol. **2**, p. 58.
28. I. Childres, L. A. Jauregui, W. Park, et al.: **Raman Spectroscopy of Graphene and Related Materials**, Chap. **19**.
29. J. Zhao, L. Liu, F. Li: **Structural Characterization. Graphene Oxide: Physics and Applications**, *Springer Briefs in Physics*, 2015, Chap. **2**.
30. S. Mallakpour, A. Abdolmaleki, S. Borandeh, *Applied Surface Science*, 2014, Vol. **307**, p. 533.

31. P. Russo, A. Hu, G. Compagnini, W.W. Duleyd., *Nanoscale*, 2014, Vol. **6**, p. 2381.
32. L. Z. Feng, Z. A. Liu, *Nanomedicine*, 2011, Vol. **6**, p. 317.
33. H. Shen, L. Zhang, M. Liu, Z. Zhang, *Theranostics*, 2012, Vol. **2**, p. 283.
34. J. A. Barreto, W. O'Malley, M. Kubeil, B. Graham, H. Stephan, L. Spiccia, *Adv. Mater.*, 2011, Vol. **23**, p. H18.
35. Y. Li, Y. Liu, Y. Fu, T. Wei, L. Le Guyader, G. Gao, R.-S. Liu, *Biomaterials*, 2012, Vol. **33**, p. 402.
36. A. Sasidharan, L.S. Panchakarla, P. Chandran, D. Menon, S. Nair, C.N.R. Rao, M. Koyakutty., *Nanoscale*, 2011, Vol. **3**, p. 2461.
37. S. A. Zhang, K. Yang, L. Z. Feng, Z. Liu, *Carbon*, 2011, Vol. **49**, p. 4040.
38. K. Yang, L. Feng, X. Shi, Zhuang Liu, *Chem. Soc. Rev*, 2013, Vol. **42**, p. 530.
39. Ruoff, S. Park, R. S. Ruoff, *Nat. Nanotechnol.*, 2009, Vol. **4**, p. 217.
40. D. Depan, J. Shah, R. D. K. Misra, *Mater. Sci. Eng.:C*, 2011, Vol. **31**, p. 1305.
41. N. G. Sahoo, H. Bao, Y. Pan, M. Pal, M. Kakran, H. K. F. Cheng, L. Li, L. P. Tan, *Chem. Commun.*, 2011, Vol. **47**, p. 5235.
42. Z. Liu, J. T. Robinson, X. M. Sun, H. J. Dai, *J. Am. Chem.*, 2008, Vol. **130**, p. 10876.
43. L. Zhang, J. Xia, Q. Zhao, L. Liu, Z. Zhang, *Small*, 2010, Vol. **6**, p. 537.
44. J. Liu, Y. Li, Y. Li, J. Li, Z. Deng, *J. Mater. Chem.*, 2010, Vol. **20**, p. 10944.
45. D. Bitounis, H. Ali-Boucetta, B. H. Hong, D.H. Min, K. Kostarelos, *Adv. Mater.*, 2013, Vol. **25**(16), p. 2258.
46. V. K. Rana, M. C. Choi , J. Y. Kong , G. Y. Kim , M. J. Kim , S. H. Kim, S. Mishra, R.P. Singh, C.S. Ha, *Macromol. Mater. Eng.*, 2011, Vol. **296**, p. 131.
47. P. Huang, C. Xu , J. Lin , C. Wang , X. Wang , C. Zhang , X. Zhou , S. Guo, D. Cui, *Theranostics*, 2011, Vol. **1**, p. 240.
48. K. Yang, S. Zhang, G. Zhang, X. Sun, S.-T. Lee, Z. Liu, *Nano Lett.*, 2010, Vol. **10**, p. 3318.

49. J. T. Robinson, S. M. Tabakman, Y. Liang, H. Wang, H.S. Casaloungue, D. Vinh, H. Dai, *J. Am. Chem. Soc.*, 2011, Vol. **133**, p. 6825.
50. K. Yang, J. Wan, S. Zhang, B. Tian, Y. Zhang, Z. Liu, *Biomaterials*, 2012, Vol. **33**, p. 2206.
51. M. Zhang, R.R. Naik, L. Dai: **GO for Photodynamic Therapy. Carbon Nanomaterials for Biomedical Applications**, *Springer Series in Biomaterials Science and Engineering*, 2016, Chap. **8**, p. 248.
52. D. E. J. G. J. Dolmans, D. Fukumura, R. K. Jain, *Nat. Rev. Cancer*, 2003, Vol. **3**, p. 380.
53. H. Dong, Z. Zhao, H. Wen, Y. Li, F. Guo, A. Shen, P. Frank, C. Lin, D. Shi, *Sci. China: Chem.*, 2010, Vol. **53**, p. 2265.
54. Z. Hu, Y. Huang, S. Sun, W. Guan, Y. Yao, P. Tang, C. Li, *Carbon*, 2012, Vol. **50**, p. 994.
55. S. Liu, T. H. Zeng, M. Hofmann, E. Burcombe, J. Wei, R. Jiang, J. Kong, Y. Chen, *ACS Nano*, 2011, Vol. **5**, p. 6971.
56. O. Akhavan, E. Ghaderi, *ACS Nano.*, 2010, Vol. **4**, p. 5731.
57. Q. Bao, D. Zhang, P. Qi, *Colloid Interface Sci.*, 2011, Vol. **360**, p. 463.
58. O. N. Ruiz, K. A. S. Fernando, B. J. Wang, N. A. Brown, P. G. Luo, N. D. McNamara, M. Vangsness, Y. P. Sun, C. E. Bunker, *ACS Nano.*, 2011, Vol. **5**, p. 8100.
59. M.D. Hughes, Y.J. Xu, P. Jenkins, P. McMorn, P. Landon, D.I. Enache, A.F. Carley, G.A. Attard, G.J. Hutchings, F. King, E.H. Stitt, P. Johnston, K. Griffin, C.J. Kiely, *Nature*, 2005, Vol. **437**, p. 1132.
60. J. Huang, T. Akita, J. Faye, T. Fujitani, T. Takei, M. Haruta, *Angew. Chem. Int. Ed.*, 2009, Vol. **48**, p. 7862.
61. M. Turner, V.B. Golovko, O.P.H. Vaughan, P. Abdulkin, A. Berenguer-Murcia, M.S. Tikhov, B.F.G. Johnson, R. M. Lambert, *Nature*, 2008, Vol. **454**, p. 981.
62. X. Yang, Y. Wang, X. Huang, Y. Ma, Y. Huang, R. Yang, H. Duan, Y. Chen, *J. Mater. Chem.*, 2011, Vol. **21**, p. 3448.

63. W. Chen, P. Yi, Y. Zhang, L. Zhang, Z. Deng, Z. Zhang, *ACS Appl. Mater. Interfaces*, 2011, Vol. **3**, p. 4085.
64. C. Wang, J. Li, C. Amatore, Y. Chen, H. Jiang, X.-M. Wang, *Angew. Chem., Int. Ed.*, 2011, Vol. **50**, p. 11644.
65. D. Depan, B. Girase, J. S. Shah, R. D. K. Misra, *Acta Biomater.*, 2011, Vol. **7**, p. 3432.
66. A. Bush, A. V. Thomas, Z.-Z. Yu, N. A. Koratkar, *Adv. Sci. Eng. Med.*, 2012, Vol. **4**, p. 15.
67. C.H. Lu, H.H. Yang, C.L. Zhu, X. Chen, G.N. Chen, *Angew. Chem.*, 2009, Vol. **121**, p. 4879.
68. D. Li et al., *Small*, 2015, Vol. **11**, p. 2200.
69. I.A. Larmour, K. Faulds, D. Graham, *Chem. Sci.*, 2010, Vol. **1**, p. 151.
70. S. Harmsen et al., *Sci. Transl. Med.*, 2015, Vol. **7**, p. 271.
71. L. Marrucci, C. Manzo, D. Paparo, *Phys. Rev. Lett.*, 2006, Vol. **96**, p. 163905.
72. N. Yi, Ch. Zhang, Q. Song, Sh. Xiao, *Scientific Reports*, 2016, Vol. **6**, p. 25134.
73. J. Liu et. al., *Acta Biomateriala*, 2013, Vol. **9**, p. 9243.
74. A. Sasidharan, L. S. Panchakarla, P. Chandran, D. Menon, S. Nair, C. N. R. Rao, M. Koyakutty, *Nanoscale*, 2011, Vol. **3**, p. 2461.
75. K. Yang, Y. Li, X. Tan, R. Peng, Z. Liu, *Small*, 2013, Vol. **9**, p. 1492.
76. S. Shi, F. Chen, E. B. Ehlerting, W. Ca, *Bioconjugate Chem.*, 2014, Vol. **25**, p. 1609.
77. M. Quintana. *Acc. Chem. Res.*, 2013, Vol. **46**, p. 138.
78. G. Neri, A. Scala, F. Barreca, E. Fazio, P.G. Mineo, A. Mazzaglia, G. Grassi, A. Piperno, *Chem. Commun.*, 2015, Vol. **51**, p. 4846.
79. H. T. Hu, X. B. Wang, J. C. Wang, L. Wan, F. M. Liu, H. Zheng et al., *Chem. Phys. Lett.*, 2010, Vol. **484**, p. 247.
80. S. Park, J. An, J.R. Potts, A. Velamakanni, S. Murali, R. S. Ruoff, *Carbon*, 2011, Vol. **49**, p. 3019.

81. J. Wang, L. Zhang, Q. Wang, D. Zhang, *J. Biomed. Nanotechnol.*, 2014, Vol. **10**, p. 543.
82. C.V. Kavitha, G. Deep, S.C. Gangar, A.K. Jain, C. Agarwal, R. Agarwal, *Mol. Carcinog.*, 2014, Vol. **51**, p. 69.
83. E. Fazio, A. Scala, S. Grimato, A. Ridolfo, G. Grassi, F. Neri, *J Mater. Chem. B*, 2015, Vol. **3**, p. 9023.
84. J.A. Kemp, M.S. Shimb, C.Y. Heo, Y.J. Kwon, *Adv. Drug Deliv. Rev.*, 2016, Vol. **98**, p. 3.
85. A. Piperno, A. Marrazzo, A. Scala, A. Rescifina, *Società Chimica Italiana, Roma*, 2015, Vol. **19**.
86. R. Elhag, E.A. Mazziro, K.F.A. Soliman, *Anticancer Res.*, 2015, Vol. **35**, p. 1263.
87. W. Feng, D. Cai, B. Zhang, G. Lou, X. Zou, *Biomed. Pharmacother.*, 2015, Vol. **74**, p. 257.
88. Y. Yao, W. Chen, Y. Du, Z. Tao, Y. Zhu, Y.X. Chen, *Phys. Chem. C*, 2015, Vol. **119**, p. 22452.
89. K. Tushar, K. Maiti, G. Sundar, S. Anirban, D. Swagata, *J. Photochem. Photobiol. A*, 2008, Vol. **194**, p. 297.
90. G. Deep, R. Agarwal, *Cancer Metastasis Rev.*, 2010, Vol. **29**, p. 447.
91. Y.S. Hsieh, S.C. Chu, S.F. Yang, P.N. Chen, Y.C. Liu, K.H. Lu, *Carcinogenesis*, 2007, Vol. **28**, p. 977.
92. P. Xu, Q. Yin, J. Shen, L. Chen, H. Yu, Z. Zhang, Y. Li, *Int. J. Pharm.*, 2013, Vol. **454**, p. 21.
93. J. Marco-Marti ´nez, S. Reboredo, M. Izquierdo, V. Marcos, J. L. Lo ´pez, *J. Am. Chem. Soc.*, 2014, Vol. **136**, p. 2897.
94. G. Grassi, A. Scala, A. Piperno, D. Iannazzo, M. Lanza, C. Milone, *Chem. Commun.*, 2012, Vol. **48**, p. 6836.
95. S. M. Heilmann, J. K. Rasmussen and L. R. Krepski, *J. Polym. Sci., Part A: Polym. Chem.*, 2001, Vol. **39**, p. 3655.

96. M. W. Jones, S. J. Richards, D. M. Haddleton, M. I. Gibson, *Polym. Chem.*, 2013, Vol. **4**, p. 717.
97. M. E. Lynn, D. M. Buck, *Polym. Chem.*, 2012, Vol. **3**, p. 66.
98. M. E. Buck, D. M. Lynn, *Polym. Chem.*, 2012, Vol. **3**, p. 66.
99. D. Iannazzo, A. Mazzaglia, A. Scala, A. Pistone, S. Galvagno, M. Lanza, C. Riccucci, G. M. Ingo, I. Colao, M. T. Sciortino, A. Piperno, G. Grassi, *Colloids Surf. B*, 2014, Vol. **123**, p. 264.
100. P. A. Russo, M. M. Antunes, P. Neves, P. V. Wiper, E. Fazio, F. Neri, F. Barreca, L. Mafra, M. Pillinger, N. Pinna, A. A. Valente, *J. Mater. Chem. A*, 2014, Vol. **2**, p. 11813.
101. S. Santangelo, E. Piperopoulos, E. Fazio, G. Faggio, S. Ansari, M. Lanza, F. Neri, G. Messina, C. Milone, *Appl. Surf. Sci.*, 2014, Vol. **303**, p. 446.
102. P. A. Russo, M. M. Antunes, P. Neves, P. V. Wiper, E. Fazio, F. Neri, F. Barreca, L. Mafra, M. Pillinger, N. Pinna, A. A. Valente, *Green Chem.*, 2014, Vol. **16**, p. 4292.
103. A. U. Alam, M. M. R. Howlader, M. J. Deen, *ECS J. Solid State Sci. Technol.*, 2013, Vol. **2**, p. 515.
104. M. Z. Igbal, M. S. Katsiotis, S. M. Alhassan, M. W. Liberatore, A. A. Abdala, *RSC Adv.*, 2014, Vol. **4**, p. 6830.
105. M. Z. Igbal, M. S. Katsiotis, S. M. Alhassan, M. W. Liberatore and A. A. Abdala, 2014, *RSC Adv.*, Vol. **4**.
106. D. Yang, X. Wang, J. Shi, X. Wang, S. Zhang, P. Han, Z. Jiang, *Biochemical Engineering Journal*, 2016, Vol. **105**, p. 273.
107. X.L. Wei, Z.Q. Ge, *Carbon*, 2013, Vol. **60**, p. 401.
108. I.V. Pavlidis, M. Patila, U. T. Bornscheuer, D. Gournis, H. Stamatis, *Trends in Biotechnology*, 2014, Vol. **32**, p. 312.
109. C. Zhang, S. Chen, P.J.J. Alvarez, W. Chen, *Carbon*, 2015, Vol. **94**, p. 531.
110. H. N. Kirkman, G. F. Gaetani, *Proc. Natl. Acad. Sci. U. S. A.*, 1984, Vol. **81**, p. 4343.
111. X.-L. Wei, Z.-Q. Ge, *Carbon*, 2013, Vol. **60**, p. 401.

112. C. Zhang, S. Chen , P.J.J. Alvarez , W. Chen, *Carbon*, 2015, Vol. **94**, p. 531.
113. Y. Liu, D.A. Peterson, H. Kimura, D. Schubert, *J.Neurochem.*, 1997, Vol. **69**, p. 581.
114. G. Koopman, C.P. Reutelingsperger, Kuijten, G.A. Keehnen, R.M. Pals, S.T.M.H. van Oers, *Blood*, 1994, Vol. **84**, p. 1415.
115. E. Bellocco, D. Barreca, G. Laganà, U. Leuzzi, E. Tellone, S. Ficarra, A. Kotyky, A. Galtieri, *Mol. Cell. Biochem*, 2009, Vol. **321** (1-2), p. 165.
116. D. Barreca, G. Laganà, S. Ficarra, E. Tellone, U. Leuzzi, A. Galtieri, E. Bellocco, *Food Res. Int.*, 2011, Vol. **44**, p. 2302.
117. D. Barreca, G. Laganà, U. Leuzzi, A. Smeriglio, D. Trombetta, E. Bellocco, *Food Chemistry*, 2016, Vol. **196**, p. 493.
118. A. Smeriglio, G. Mandalari, C. Bisignano, A. Filocamo, D. Barreca, E. Bellocco, D. Trombetta, *Industrial Crops and Products*, 2016, Vol. **83**, p. 283.
119. R.L. Levine, D. Garland, C.N. Oliver, A. Amici, I. Climent, A.G. Lenz, B.W. Ahn, S. Shaltiel, E.R. Stadtman, *Methods Enzymol*, 1990, Vol. **186**, p. 464.
120. P. Mineo, D. Vitalini, E. Scamporrino, *Rapid Commun. Mass Spectrom.*, 1999, Vol. **13**, p. 2511.
121. P. Mineo, E. Scamporrino, D. Vitalini, R. Alicata, S. Bazzano, *Rapid Commun. Mass Spectrom.*, 2005, Vol. **19**, p. 2773.
122. G. Montaudo, E. Scamporrino, D. Vitalini, P. Mineo, *Rapid Commun. Mass Spectrom.*, 1996, Vol. **10**, p. 1551.
123. D. Vitalini, P. Mineo, E. Scamporrino, *Macromolecules*, 1997, Vol. **30**, p. 5285.
124. E. Scamporrino, P. Maravigna, D. Vitalini, P. Mineo, *Rapid Commun. Mass Spectrom.*, 1998, Vol. **12**, p. 646.
125. F. Bonaccorso, L. Colombo, G. Yu, M. Stoller, V. Tozzini, A. C. Ferrari, R. S. Ruoff, V. Pellegrini, *Science*, 2015, Vol. **347**, p. 1246501.
126. H. P. Cong, J. F. Chen, S. H. Yu, *Chem. Soc. Rev.*, 2014, Vol. **43**, p. 7295.
127. T. Mahmoudi, W. Y. Rho, H. Y. Yang, S. R. P. Silva, Y. B. Hahn, *Chem. Commun.*, 2014, Vol. **50**, p. 8705.

128. J. M. Tour, *Chem. Mater.*, 2014, Vol. **26**, p. 163.
129. G. X. Liu, *J. Nanoelectron. Optoelectron.*, 2012, Vol. **7**, p. 329.
130. S. Goenka, V. Sant, S. Sant, *J. Controlled Release*, 2014, Vol. **173**, p. 75.
131. K. Kostarelos, K. S. Novoselov, *Nat. Nanotechnol.*, 2014, Vol. **9**, p. 744.
132. S. X. Shi, F. Chen, E. B. Ehlerding, W. B. Cai, *Bioconjugate Chem.*, 2014, Vol. **25**, p. 1609.
133. M. Quintana, K. Spyrou, M. Grzelczak, W. R. Browne, P. Rudolf, M. Prato, *ACS Nano*, 2010, Vol. **4**, p. 3527.
134. Y. Cao, S. Osuna, Y. Liang, R. C. Haddon, K. N. Houk, *J. Am. Chem. Soc.*, 2013, Vol. **135**, p. 17643.
135. X. J. Xu, W. Lv, J. Huang, J. J. Li, R. L. Tang, J. W. Yan, Q. H. Yang, J. G. Qin, Z. Li, *RSC Adv.*, 2012, Vol. **2**, p. 7042.
136. J. M. Seo, I. Y. Jeon, J. B. Baek, *Chem. Sci.*, 2013, Vol. **4**, p. 4273.
137. J. Baek, J. B. Seo, *Chem. Commun.*, 2014, Vol. **50**, p. 14651.
138. Z. Ji, J. Chen, L. Huang, G. Shi, *Chem. Comm.*, 2015, Vol. **51**, p. 2806.
139. G. Grassi, A. Scala, A. Piperno, D. Iannazzo, M. Lanza, C. Milone, A. Pistone, S. Galvagno, *Chem. Commun.*, 2012, Vol. **48**, p. 6836.
140. A. Piperno, A. Scala, F. Risitano, G. Grassi, *Curr. Org. Chem.*, 2014, Vol. **18**, p. 2691.
141. J. S. Fisk, R. A. Mosey, J. J. Tepe, *Chem. Soc. Rev.*, 2007, Vol. **36**, p. 1432.
142. J. Marco-Martinez, S. Reboredo, M. Izquierdo, V. Marcos, J. L. Lopez, S. Filippone, N. Martin, *J. Am. Chem. Soc.*, 2014, Vol. **136**, p. 2897.
143. A. Das, B. Chakraborty, A. K. Sood, *Bull. Mater. Sci.*, 2008, Vol. **31**, p. 579.
144. R. Saito, M. Hofmann, G. Dresselhaus, A. Jorio, M. S. Dresselhaus, *Adv. Phys.*, 2011, Vol. **60**, p. 413.
145. R. Saito, A. Jorio, A. G. Souza, G. Dresselhaus, M. S. Dresselhaus, M. A. Pimenta, *Phys. Rev. Lett.*, 2002, Vol. **88**, p. 027401.
146. R. B. Weinstock, F. Weinhold, *J. Chem. Phys.*, 1985, Vol. **83**, p. 735.

147. J. E. Carpenter, F. Weinhold, *J. Mol. Struct.: THEOCHEM*, 1988, Vol. **169**, p. 41.
148. *Pure Appl. Chem. R. Sustmann.*, 1974, Vol. **40**, p. 569.
149. F. Weinhold, *Encyclopedia of computational chemistry*, 1998.
150. F. Weinhold, C. R. Landis: **Valency and bonding: a natural bond orbital donor–acceptor perspective**, *Cambridge University Press, Cambridge, UK*, 2005.
151. C. Y. Lview, C. Y. Legault, Universit´ e de Sherbrooke
<http://www.cylview.org>, **2009**.
152. C. Ciraci, R. T. Hill, J. J. Mock, Y. Urzhumov, A. I. Fernández-Domínguez, S. A. Maier, J. B. Pendry, A. Chilkoti, D. R. Smith, *Science*, 2012, Vol. **337**, p. 1072.
153. S. Huang, X. Ling, L. Liang, Y. Song, W. Fang, J. Zhang, J. Kong, V. Meunier, M.S. Dresselhaus, *Nano Lett.*, 2015, Vol. **15**, p. 2892.
154. H. Zheng, Xi-When Du, S.C. Singh, S.A. Kulinich, S. Yang, J. He, W. Cai, *Adv. Funct. Mater.*, 2012, Vol. **22**, p. 1333.
155. L. Lascialfari P. Marsili, S. Caporali, M. Muniz-Miranda, G. Margheri, A. Serafini, A. Brandi, E. Giorgetti, S. Cicchi, *Thin Solid Films*, 2014, Vol. **93**, p. 596.
156. J. Li, C.Y.Liu, *Eur. J. Inorg. Chem.*, 2010, Vol. **8**, p. 1244.
157. P.Hildebrandt, M.Stockenburger, *J.Phys.Chem.*, 1984, Vol. **88**, p. 5935.
158. R. Valero, R. Costa, I. D. P. R. Moreira, D. G. Truhlar, F. Illas, *J. Chem. Phys.*, 2008, Vol. **128**, p. 114103.
159. Y. Zhao, D. G. Truhlar, *Theor. Chem. Acc.*, 2008, Vol. **120**, p. 215.
160. W. J. Hehre: **Ab initio molecular orbital theory**, *Wiley, New York*, 1986.
161. *Acc. Chem. Res. K. Fukui*, 1981, Vol. **14**, p. 363.
162. M. Headgordon, J. A. Pople, *J. Chem. Phys.*, 1988, Vol. **89**, p. 5777.
163. H. B. Schlegel, *J. Comput. Chem.*, 1982, Vol. **3**, p. 214.
164. M. J. Frisch et al., *Gaussian 09 Revision D.01*.
165. D. Mandal, A.N. Shirazi, K. Parang, *Organic & Biomolecular*, 2014, p. 1.

166. X. Zhao, F. Pan, J. R. Lu, *Progress in Nature Science*, 2008, Vol. **18**, p. 653.
167. Y. B. Lim, K. S. Moon, M. Lee, *Chem. Soc. Rev.*, 2009, Vol. **38**, p. 925.
168. R. V. Ulijn, A. M Smith, *Chem. Soc. Rev.*, 2008, Vol. **37**, p. 664.
169. E. De Santis, M.G. Ryadnov, *Chem. Soc. Rev.*, 2015, Vol. **44**, p. 8288.
170. X. Zhao, S. Zhang, *Macromol. Biosci.*, 2007, Vol. **7**, p. 13.
171. H. Yokoi, T. Kinoshita, S. Zhang, *Proc. Natl. Acad. Sci. USA*, 2005, Vol. **102**, p. 8414.
172. F. Gelain, D. Bottai, A. Vescovi et al., *PLoS ONE*, 2006, Vol. **1**, p. 1.
173. J. Kisiday, M. Jin, B. Kurz et al, *Proc. Natl. Acad. Sci. USA*, 2002, Vol. **99**, p. 9996.
174. S. Zhang S, X. Zhao, *J Mater Chem*, 2004, Vol. **14**, p. 2082.
175. X. Zhao, Y. Nagai, P.J.Reeves et al., *Proc. Natl. Acad. Sci. USA*, 2006, Vol. **47**, p. 17707.
176. P. Kiley, X, Zhao, M. Vaughn et al., *PLoS Biol*, 2005, Vol. **3**, p. 1180.
177. J.J Schwartz, S. Zhang, *Curr Opin*, 2000, Vol. **2**, p. 1464.
178. C.Cohen, D.A.D. Parry, *Science*, 1994, Vol. **263**, p. 488.
179. A. Lupas, *Trends Biochem. Sci.*, 1996, Vol. **21**, p. 375.
180. R. Siegert, M.R. Leroux, C. Scheufler, F.U. Hartl, I. Moarefi, *Cell*, 2001, Vol. **103**, p. 621.
181. F.H.C. Crick, *Acta Crystallogr.*, 1953, Vol. **6**, p. 689.
182. Y. Wu, J. H. Collier, *WIREs Nanomed. Nanobiotechnol.*, 2016,
183. R.S. Hodges, *Biochem. Cell. Biol.*, 1996, Vol. **74**, p. 133.

184. Y.B. Yu, *Advanced Drug Delivery Reviews*, 2002, V

ol. **54**, p. 1113.

185. D.N. Woolfson, *Advances in Protein Chemistry*, 2005, Vol. **70**, p. 79.

186. J. Stetefeld, M. Jenny, T. Schulthess, R. Landwher, J. Engel, R.A. Kammerer, *Nat. Struct. Biol.*, 2000, Vol. **7**, p. 772.
187. J.M. Fletcher, R.L. Harniman, F.R. Barnes, A.L. Boyle, A. Collins, J. Mantell, T.H. Sharp, M. Antognozzi, P.J. Booth, N. Linden et al., *Science*, 2013, Vol. **340**, p. 595.
188. H. Dong, S.E. Paramonov, J.D. Hartgerink, *J Am Chem Soc*, 2008, Vol. **130**, p. 13691.
189. C. Xu, C. R. Liu, A.K. Mehta, R.C. Guerrero-Ferreira, E.R. Wright, S. Dunin-Horkawicz, K. Morris, L.C. Serpell, X. Zuo, J.S. Wall et al., *J Am Chem Soc*, 2013, Vol. **135**, p. 15565.
190. E.H. Egelman, C. Xu, F. DiMaio, E. Magnotti, C. Modlin, X. Yu, E. Wright, D. Baker, D.V.P. Conticello, *Structure*, 2015, Vol. **23**, p. 280.
191. Y. Shi, S-A Liu, D.J. Kerwood, J. Goodisman, J.C. Dabrowiak, *J. Inorg. Biochem.*, 2012, Vol. **107**, p. 6.
192. B. Apostolovic, S. P. Deacon , R. Duncan , H-AA Klok, *Macromol. Rapid Commun.*, 2011, Vol. **32**, p. 11.
193. Z. S. Al-Ahmady, W. T. Al-Jamal, J. V. Bossche, T. T. Bui, A.F. Drake, A. J. Mason, K. Kostarelos, *ACS Nano*, 2012, Vol. **6**, p. 9335.
194. L.J. Picker, S.G. Deeks, *Nature*, 2013, Vol. **503**, p. 207.
195. F. Krammer, P. Palese, *Nat. Rev. Drug. Discov.*, 2015, Vol. **14**, p. 167.
196. T.A.P.F. Pimentel, Z. Yan, S.A. Jeffers, K.V. Holmes, R.S. Hodges, P. Burkhard, *Chem. Biol. Drug Des.*, 2009, Vol. **73**, p. 53.
197. J. Kong, S. Yu, *Acta Biochem Biophys Sin*, 2007, Vol. **39**, p. 549.
198. T. Heimburg, J. Schunemann, K. Weber, N. Geisler, *Biochemistry*, 1999, Vol. **38**, p. 12727.
199. A. D. Melhado, M. Luparia and F. D. Toste, *J. Am. Chem. Soc.*, 2007, Vol. **129**, 12638.